Nanoparticle synthesis using flame spray pyrolysis for catalysis

Høj, Martin; Grunwaldt, Jan-Dierk; Jensen, Anker Degn; Elmøe, Tobias Dokkedal

Publication date:
2012

Document Version
Publisher's PDF, also known as Version of record

Nanoparticle synthesis using flame spray pyrolysis for catalysis

One step synthesis of heterogeneous catalysts

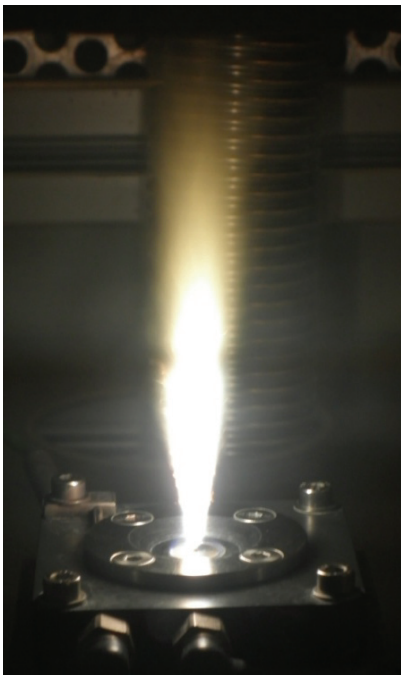

Martin Høj

Ph.D. Thesis

Technical University of Denmark

September 2012

DTU Chemical Engineering
Department of Chemical and Biochemical Engineering

Nanoparticle synthesis using flame spray pyrolysis for catalysis
One step synthesis of heterogeneous catalysts

Ph.D. Thesis

September 2012

by

Martin Høj

Cover photo: Flame spray pyrolysis nozzle during synthesis of Mo/Al_2O_3 catalyst.

Published by: Department of Chemical and Biochemical Engineering, Søltofts Plads, Building 229, DK-2800 Kgs. Lyngby, Denmark

Request report from: www.kt.dtu.dk

Reproduced figures: Permissions for reproduction of figures from the literature were obtained from the publishers.

ISBN: 978-87-92481-96-2

Preface and acknowledgements

This thesis is submitted as partial fulfillment of the Ph.D. degree at the Technical University of Denmark. It is the product of three years employment in research, teaching, supervision of project students and studies in chemical engineering. The thesis is intended as a summary of the results of my research.

The project is titled “Nanoparticle Synthesis Using Flame Spray Pyrolysis for Catalysis”. The unifying topic of my research is Flame Spray Pyrolysis (FSP), which was used for the synthesis of catalysts for oxidative dehydrogenation of propane and for hydrotreating. Structural characterization of the catalysts was performed and structure-activity-selectivity relations of these reactions were investigated.

I would like to thank several people who helped me. First of all, I thank my supervisors Jan-Dierk Grunwaldt and Anker D. Jensen for all their useful advice, our many meetings and constructive comments to my work. Tobias D. Elmøe also acted as supervisor in the beginning of my Ph.D. work and I am very grateful for all the help he provided in starting up the FSP work. Many thanks to Michael Brorson and his team at Haldor Topsøe A/S for the hydrotreating catalytic activity measurements and related discussions. Also thanks to Pablo Beato and his team at Haldor Topsøe A/S for allowing me to use their Raman and UV-vis facilities, discussing my results and directing me to literature. I also owe special thanks to Lutz Mädler and David K. Pham from University of Bremen for two-nozzle FSP synthesis of catalyst samples and related discussions.

From my own department, I would like to thank Anders Tiedje for discussions, advice, ideas and solutions to all technical problems. Thanks to the DTU-Chemical Engineering workshop team for materializing ideas and sketches. Thanks to Thomas Wolfe for his LabView program suite and for helping me programming the automated catalytic activi-

ty test setup control. Thanks to my present and former Ph.D. and post doc. colleagues in the fields of catalysis and FSP: Matthias, Jakob, Michael, Xiao, Peter, Rasmus and Kirsten for fruitful discussions and good times at conferences. Also thanks to the Ph.D. students and colleagues at the department, particularly the "Lunch Club", who contributed to a pleasant working environment and good times at the Friday Bar, department parties and Staff Club events. Thanks to the students I co-supervised: Henrike, Thomas, Kasper and Thomas, Line and Anders for their hard and dedicated work.

Also thanks to Stefan Mangold (XAS beam line, ANKA synchrotron) and the Grunwaldt group: Alexey Boubnov, Gian Luca Chiarello, Matthias Bauer, Wolfgang Kleist, Georg Hofmann, Henning Lichtenberg and Maria Casapu for designing the in-situ XAS setup and their help during beam times. Thanks to Finn Petersen from ChimneyLab Europe for a very good collaboration during the design and construction of the setup for oxidative dehydrogenation. Thanks to Jakob B. Wagner and Thomas W. Hansen from DTU-CEN for teaching me how to acquire TEM images. The Danish Council for Strategic Research (Nanoparticle design by flame spray pyrolysis and hydrothermal synthesis for catalysis. Grant no. 2106-08-0039) and DTU-Chemical Engineering are gratefully acknowledged for funding my Ph.D. project. DanScatt, the EU (Contract RII13-CT-2004-506008) and BMBF (Materials in action) are acknowledged for funding travels to and measurements at the ANKA synchrotron.

I would also like to thank my parents and grandparents for always supporting me throughout my entire education.

Finally, the most important thank goes to my two special girls Christina and Amalie ☺

Martin Høj
Copenhagen, September 4, 2012

List of publications and conference presentaions

International peer-reviewed journals

Martin Høj, Kasper Linde, Thomas K. Hansen, Michael Brorson, Anker D. Jensen and Jan-Dierk Grunwaldt: ”Flame spray synthesis of $CoMo/Al_2O_3$ hydrotreating catalysts”, *Appl. Catal. A* **397** (2011) 201–208.

Martin Høj, Anker D. Jensen and Jan-Dierk Grunwaldt: ”Structure of alumina supported vanadia catalysts for oxidative dehydrogenation of propane prepared by flame spray pyrolysis”, *Appl. Catal. A* **451** (2013) 207-215.

Martin Høj, David K. Pham, Michael Brorson, Lutz Mädler, Anker D. Jensen and Jan-Dierk Grunwaldt: ”Two-nozzle FSP synthesis of $CoMo/Al_2O_3$ hydrotreating catalysts”, *Catal. Lett.* Accepted (2013)

Martin Høj, Thomas Kessler, Anker D. Jensen and Jan-Dierk Grunwaldt: ”Structure, activity and kinetics of supported molybdenum oxide and mixed molybdenum-vanadium oxide catalysts prepared by flame spray pyrolysis”, *In preparation for Appl. Catal. A*

Other journals

Martin Høj, Jakob M. Christensen, Anker D. Jensen and Jan-Dierk Grunwaldt: ”Flamme spray pyrolyse til fremstilling af nano-materialer. Syntese af nanopartikler i gasfase åbner nye muligheder for fremstilling af funktionelle nanomaterialer med kontrolleret sammensætning, partikelstørrelse og krystallinsk struktur”, *submitted for Dansk Kemi.*

Oral conference contributions

Martin Høj, Michael Brorson, Anker D. Jensen and Jan-Dierk Grunwaldt. ”Co-Mo/Al_2O_3 hydrotreating catalysts prepared by flame synthesis”. Presented at: EuropaCat X, 2011, Glasgow, Scotland.

Martin Høj, Michael Brorson, Anker D. Jensen and Jan-Dierk Grunwaldt. ”Flame synthesized CoMo/Al_2O_3 hydrotreating catalysts”. Presented at: 8th European Congress of Chemical Engineering (ECCE8), 2011, Berlin, Germany.

Poster conference contributions

Martin Høj, Anker D. Jensen and Jan-Dierk Grunwaldt. ”Flame made V/Al_2O_3 propane oxidative dehydrogenation catalyst”. Presented at: EuropaCat X, 2011, Glasgow, Scotland.

Martin Høj, Anker D. Jensen and Jan-Dierk Grunwaldt. ”Flame synthesized vanadia catalysts for oxidative dehydrogenation of propane”. Presented at: The 15th Nordic Symposium on Catalysis, 2012, Åland, Finland.

Martin Høj, Anker D. Jensen and Jan-Dierk Grunwaldt. ”Flame synthesised vanadium and molybdenum oxide catalysts for oxidative dehydrogenation of propane”. Presented at: The 15th International Congress on Catalysis, 2012, Munich, Germany. Selected for poster symposium presentation.

Martin Høj, Michael Brorson, David K. Pham, Lutz Mädler, Anker D. Jensen and Jan-Dierk Grunwaldt. ”One- and two-flame synthesis of $CoMo/Al_2O_3$ and $CoMo/Al_2O_3$-SiO_2 hydrotreating catalysts”. Presented at: The 15th International Congress on Catalysis, 2012, Munich, Germany.

Abbreviations and nomenclature

Abbreviations

BET	Brunauer, Emmett and Teller's theory for SSA calculation
DBT	Dibenzothiophene
DFT	Density functional theory
DMDS	Dimethyl disulfide
EXAFS	Extended X-ray absorption fine structure
FCC	Fluid catalytic cracking
FID	Flame ionization detector (gas chromatography)
FSP	Flame spray pyrolysis
FTIR	Fourier transform infra red (spectroscopy)
GC (GC-FID, GC-MS)	Gas chromatography (gas chromatograph with flame ionization detector or mass spectrometer detector)
HDN	Hydrodenitrogenation
HDS	Hydrodesulfurization
HYD	Hydrogenation
LMCT	Ligand to metal charge transfer
MFC	Mass flow controller
MS	Mass spectrometry
N (Nl/Nml)	Normal (normal liter/normal milliliter)
ODP	Oxidative dehydrogenation of propane
PI	Piping and instrumentation
SAXS	Small angle X-ray scattering
SSA	Specific surface area in m^2/g
STM	Scanning tunneling microscopy
STY	Space time yield in $g_{propene}/(g_{cat} \cdot h)$
TCD	Thermal conductivity detector (gas chromatography)
TEM	Transmission electron microscopy
ToF-SIMS	Time of flight-Secondary ion mass spectrometry
TPR	Temperature programmed reduction
UV-vis	Ultra violet to visible light (spectroscopy)
wt.%	Weight percentage
XANES	X-ray absorption near edge spectroscopy
XRD	X-ray diffraction

Nomenclature

[X]	Concentration of species X in mol/l
2θ	Scattering angle in X-ray diffraction
D_{eff}	Effective diffusivity in cm^2/s
d_p	Particle diameter in nm
E_0	Absorption edge energy in X-ray absorption spectroscopy
$E_{a,x}$	Activation energy in kJ/mol of reaction *x*
F	Volumetric flow in cm^3/s
$F(R_\infty)$	Kubelka-Munk function (UV-vis)
$h\nu$	Photon energy in eV
k (In X-ray absorption spectroscopy)	Outgoing photo electron wave number in $Å^{-1}$
$k_{0,x}$	Pre-exponential factor in $cm^3/(g \cdot s)$ of reaction *x*
k_x (in kinetics)	First order reaction rate constant in $cm^3/(g \cdot s)$ of reaction *x*
m/z	Mass divided by charge (Mass spectrometry)
m_x	Mass of x in g
N	Number of particles
R (In kinetics)	Gas constant in J/(mol·K)
R (In Thiele modulus)	Radius in cm
R (In X-ray absorption spectroscopy)	Distance in Å
R_∞ (In UV-vis spectroscopy)	Percentage reflection of infinite layer
r_x	Reaction rate of reaction *x*
S	Selectivity to propene
T	Temperature in K or °C
w	Mass of catalyst in g
X	Conversion of propane
y_i	Measured mole fraction of species *i* (Gas chromatography)
y_i^{corr}	Internal standard corrected mole fraction of species *i*
Y_x	Yield of species X (X = C_3H_6 or CO_x)
η	Effectiveness factor
$\mu(E)$	Absorption coefficient in X-ray absorption spectroscopy as function of photon energy
ρ	Density in g/cm^3
φ	Thiele modulus
$\chi(k)$	EXAFS function of outgoing photo electron wave number
$\chi(R)$	Fourier transformed EXAFS function of distance in Å

Abstract

Roughly 85 to 90 % of the products from the chemical industry have been in contact with a catalyst and the production volume and financial turnover of the catalyst industry are expected to increase in the near future. This growth will be fueled by increasing demands for chemicals, new catalytic processes based on renewable feedstock, new or improved ways of preparing catalysts and a better understanding of the catalyst structure at operating conditions.

This thesis explores flame spray pyrolysis (FSP) as a novel one-step preparation method for heterogeneous catalysts and investigates structure-activity-selectivity relationships. Specific catalysts studied are cobalt-molybdenum hydrotreating catalysts and vanadium and molybdenum oxide catalysts for oxidative dehydrogenation of propane (ODP).

Hydrotreating is an established field in the petrochemical industry, driven by strict legislation on sulfur and nitrogen content in transportation fuels. Research is therefore performed to improve the commercial catalysts. In this thesis, FSP prepared catalysts are demonstrated to have an activity of up to 91 % of a commercial reference. This is promising for a new synthesis method which has not yet been optimized. The catalysts structure was investigated by spectroscopy and electron microscopy.

ODP is an exothermic, alternative process to current highly energy demanding propene production methods; however the propene selectivity is a major obstacle for commercialization. FSP prepared vanadia catalysts with low vanadium loadings gave propene yields of up to 13 % at 33 % propane conversion and space time yields of up to 0.88 $g_{propene}/(g_{cat} \cdot h)$, which competes well with vanadia catalysts prepared by other methods. Kinetics of the reaction and the catalyst structure were investigated by in-situ and ex-situ by e.g. X-ray absorption and Raman spectroscopy.

Dansk resumé

Omtrent 85 til 90 % af verdens kemikalieproduktion er fremstillet ved katalyse. Både mængden af producerede katalysatorer og katalysatorindustriens omsætning forventes at vokse i fremtiden. Denne vækst bliver båret af øget efterspørgsel på kemikalier, nye katalytiske processer baseret på bæredygtige råstoffer, nye eller forbedrede katalysatorproduktionsmetoder og øget fundamental forståelse af katalysatorer under procesbetingelser.

Emnet for denne afhandling er flamme spray pyrolyse (FSP), en ny metode til at fremstille katalysatorer i et trin, samt struktur-aktivitet-selektivitet relationer. De undersøgte katalysatorer er kobolt-molybdænkatalysatorer til hydrotreating og vanadium- og molybdænoxidkatalysatorer til oxidativ dehydrogenering af propan (ODP).

Hydrotreating er en vigtig proces i den petrokemiske industri, pga. miljøregler om begrænsning af mængden af svovl og nitrogen i diesel. Der forskes derfor for at få mere effektive kommercielle katalysatorer. I denne undersøgelse opnåede de undersøgte katalysatorer en aktivitet på 91 % i forhold til en kommerciel reference. Katalysatorer fremstillet med FSP har derfor potentiale til at konkurrere med kommercielle katalysatorer. FSP katalysatorernes struktur blev undersøgt med spektroskopi og elektronmikroskopi.

ODP er en alternativ, eksoterm propenproduktionsmetode sammenlignet med nuværende endoterme fremstillingsmetoder. Den største begrænsning for anvendelsen af ODP er selektiviteten. Vanadiumoxidkatalysatorer fremstillet med FSP med lav koncentration af vanadium gav 13 % propenudbytte ved 33 % propanomsætning og op til 0.88 $g_{propen}/(g_{kat} \cdot h)$ i vægt-tidsudbytte. Dette er på niveau med

vanadiumoxidkatalysatorer fremstillet ved konventionelle metoder. Reaktionskinetikken og katalysatorstrukturen blev undersøgt med bl.a. Røntgen absorption og Raman spektroskopi.

Contents

1. Introduction

1.1 Flame spray pyrolysis (FSP)

Liquid fed flame spray pyrolysis (FSP) is a novel one-step synthesis method for preparation of nano-sized particles [1-2]. Typically, organic metal compounds are dissolved in an organic solvent and the precursor solution is sprayed as micrometer sized droplets with high velocity oxygen and ignited with a small premixed methane-oxygen flame (see Figure 1.1) [3]. The solvent and metal compounds quickly evaporate and combust to form atomically dispersed vapors of metal oxides, which nucleate to form clusters when reaching cooler parts of the flame. The formed clusters grow by surface growth and coalescence, accompanied by sintering [4]. This results in non-porous nanoparticles, which coagulate and sinter to form agglomerates and aggregates with high inter particle porosity [1]. The flame process gives high maximum temperature and a short residence time with homogeneous nanoparticles as the product. Most of the combustion enthalpy for the spray flame comes from the solvent [5]. It is important, that the combustion enthalpy is sufficiently high and the flame is sufficiently hot for rapid vaporization of the liquid droplets of the precursor solution, so that nucleation and particle growth occur from the gas phase; otherwise, micrometer sized hollow or shell like particles are formed [1,5].

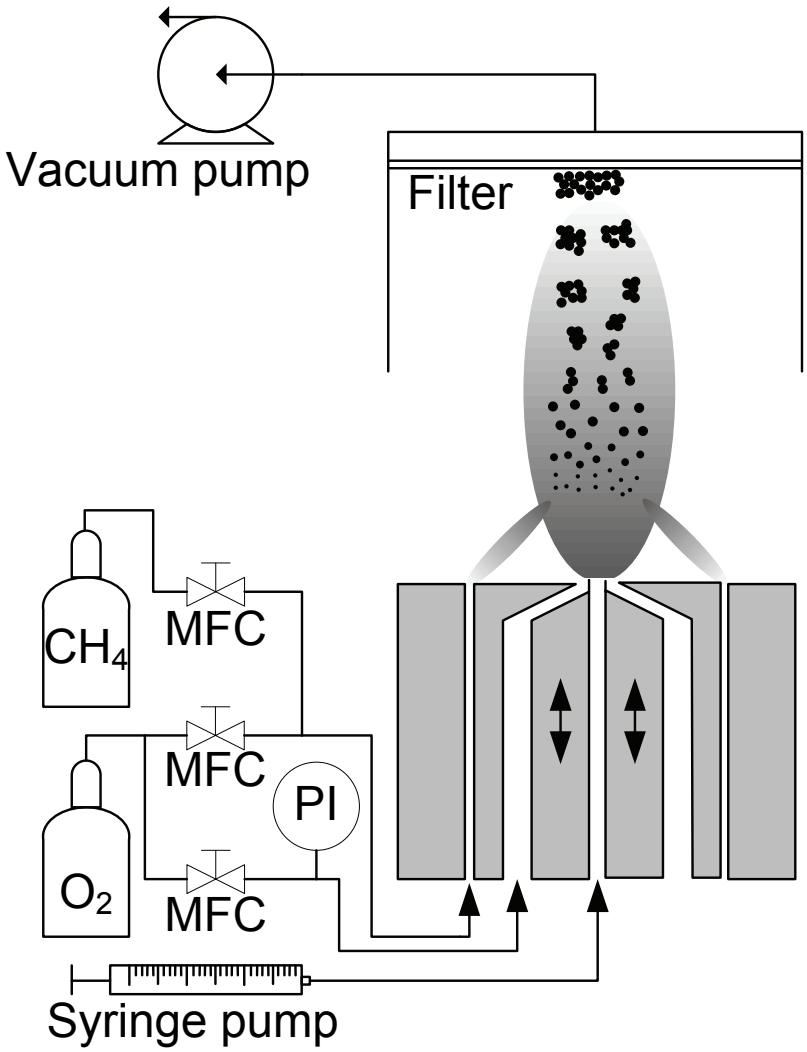

Figure 1.1: Schematic diagram of the FSP setup at DTU-Chemical Engineering. The precursor solution is injected with a syringe pump in the central capillary and is sprayed with high velocity oxygen around the capillary at a pressure drop of at least 1.5 bar. The capillary holder can be moved up and down to adjust the pressure drop (PI). The precursor droplets are ignited with a premixed methane oxygen flame and the particles collected on a filter above the flame with the aid of a vacuum pump. All gas flows are controlled by calibrated mass flow controllers (MFC). Cluster formation, particle growth and agglomeration are schematically shown.

Materials produced by FSP are very interesting candidates for heterogeneous catalysts because of their high surface area. Furthermore, the use of precursor solutions containing several metal compounds allows one-step preparation of multi-component catalyst materials. Conventional catalyst preparation would include precipitation, washing, dry-

ing and calcination of the support material followed by impregnation, drying and calcination of the active phase [6]. On lab-scale this might take two to four days depending on the number of steps, but with FSP the calcined catalyst is obtained within a few hours work.

FSP has been exploited for preparation of supported noble metal catalysts and mixed oxide catalysts [6-7]. In case of mixed oxide materials, the multi-metal compound precursor solutions can lead to mixed-metal oxides, solid solutions or segregated phases of oxides. The result depends on the solid phase miscibility of the two oxides, the volatility of the metals/oxides and the flame properties such as residence time and temperature.

One-step flame synthesis of noble metals on typical oxide supports (Al_2O_3, TiO_2, SiO_2, ZnO, ZrO_2, ect.) yields segregated phases of oxide supported noble metals, while mixing two noble metal compounds in the precursor solution can result in particles consisting of both metals, e.g. Ag-Au, Pd-Pt and Pt-Rh [7-8]. When using precursor solutions containing both vanadium and titanium compounds, the product was crystalline titania with vanadia on the surface, due to the much higher volatility of vanadia [6]. On the other hand, solutions containing both cerium and zirconium compounds resulted in either segregated CeO_2 and ZrO_2 or mixed-metal $Ce_xZr_{1-x}O_2$ depending on the solvent boiling point and combustion enthalpy [9-10]. Solutions with aluminum and cobalt compounds yielded the whole range of phases from Al_2O_3, $CoAl_2O_4$, CoO to Co_3O_4 depending on the element ratio [11]. Finally, the preparation of Ru-promoted Co/ZrO_2 Fischer-Tropsch catalysts by FSP resulted in well dispersed Co_3O_4 in a ZrO_2 matrix, whereas incipient wetness impregnation of ZrO_2 with Co gave large clusters of Co_3O_4 as observed by TEM and XRD [12].

When preparing alumina or alumina supported catalysts by FSP, there seem to be differences in opinion about which phase is formed. The group of Laine reported a mixture of mostly δ-Al_2O_3 with some θ-Al_2O_3 and minor amounts of γ-Al_2O_3 [11,13-14] and the group of Pratsinis reported only γ-Al_2O_3 [8,15-17]. The difference may be the particle size, since the specific surface areas reported by the Laine group are around 50 to70 m^2/g. The Pratsinis group reported surface areas around 110 to 130 m^2/g. When the particles are small, the line broadening of the diffraction pattern is significant, making it difficult to distinguish between the polymorphs of alumina [18]. Which phase is the thermodynamically stable one may also depend on the particle size, since the γ- to α-polymorph transformation always leads to significant sintering and much larger primary particles [14].

Besides heterogeneous catalysis, FSP has been applied in several other materials research fields, e.g. synthesis of nano-phosphors for bio-labeling [19], gas sensors [20], battery materials [21], fuel cells [22], solar cell materials [23] and bio-active nanoparticles [24]. Research and development for pilot scale FSP production with production rates around 100 to 500 g/h is performed [25-28].

A recent study of zirconia synthesis by FSP combined with computational fluid dynamics (CFD) calculations showed, that the maximum flame temperature may be 3000 K at about 20 mm above the nozzle [29]. At this height most of the liquid solvent (ethanol and 1-propanol) and precursor (Zr(*n*-propoxide)$_4$) have evaporated and are present as gasses. The formation of solid ZrO_2 is observed from about 10 mm above the nozzle (see Figure 1.2). Sampling particles at 50 mm above the burner showed individual particles and at 100 mm agglomerates were formed. Simulations showed that the primary particle size continued to grow until about 130 to 200 mm above the burner depending

on the dispersion gas flow, where the temperature has dropped below 1000 K. Similar observations have been performed by in-situ small angle X-ray scattering (SAXS) for the synthesis of silica in vapor fed flames [30].

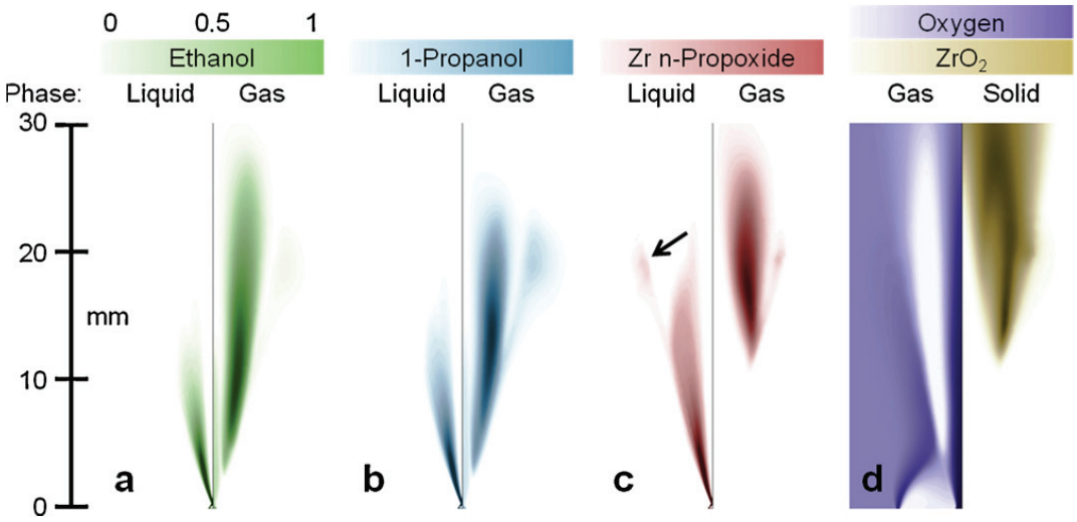

Figure 1.2: Model-predicted multi-component evaporation of ethanol (a, green), 1-propanol (b, blue) and zirconium *n*-propoxide (c, red) atomized at 4 ml/min precursor solution feed by 5 l/min O_2. Figure a–c present the normalized mass fraction of the components in the liquid (left) and gas (right) phases. Also shown are normalized gas phase mass fractions of oxygen (d, left, purple) and zirconia nanoparticles (d, right, yellow). The arrow points at droplets that have escaped the reaction zone. Figure from ref. [29] with permission.

One further development of the FSP process is two-nozzle FSP [5]. Studies on $Pt/Ba/Al_2O_3$ showed that NO_x storage-reduction catalysts could be produced with better storage capacity, as compared to traditional one-nozzle FSP, due to the synthesis of individually crystalline $BaCO_3$ and Al_2O_3 nanoparticles in separate flames, preventing the formation of $BaAl_2O_4$ [31]. In addition to maintaining many of the advantages of conventional FSP, two-nozzle FSP can also offer control over the mixing of the individual components from the different flames, which further increases the process flexibility.

FSP is one technique in a family of flame processes for synthesis of nanoparticles, which have been extensively reviewed [1-2,5-6,32-34]. Vapor fed flame aerosol synthe-

sis is a related technique, where volatile combustible precursors (e.g. acetylacetonates) are fed as vapors with a carrier gas into a methane-oxygen flame [35-38]. Like for FSP, the precursors combust to form atomically dispersed vapors of metal oxides, which nucleate to nanoparticles, which are collected on a filter. This method is limited to elements, where volatile precursors are available and the production rate is rather low. However, feeding already vaporized precursors to the flame is an advantage.

Most elements are available as organically dissolvable precursors, but commercial use of FSP would be limited to elements, where those precursors are available at a reasonable price or are relatively easy to prepare from cheap materials. Flame assisted spray pyrolysis is intended to overcome this problem by using aqueous or alcoholic solutions of e.g. metal nitrates. However, this has the problem of forming inhomogeneous micrometer sized particles, because the combustion enthalpy is not high enough for rapid evaporation of the precursor droplets, so particles form in the liquid phase. This can partly be overcome by using an acetylene assisted flame, where acetylene is added in a ring around the flame jet [39].

1.2 Hydrotreating

Hydrotreating is performed at oil refineries in order to remove sulfur (hydrodesulphurization, HDS) and nitrogen (hydrodenitrogenation, HDN) from the heterocyclic compounds in which these elements typically occur in crude oil [40-41]. Besides removal of sulfur and nitrogen, the hydrotreating process also effects (partial) hydrogenation (HYD) of some aromatic compounds in the oil.

Industrial hydrotreating catalysts contain as active phase cobalt or nickel promoted molybdenum(IV)sulfide, MoS_2, on an alumina support [40-42]. The catalysts are typically prepared by simultaneous or sequential impregnation of a pre-shaped alumina support

with aqueous solutions of molybdenum, cobalt and/or nickel compounds, followed by calcination to obtain the active metals in their oxidic form on the alumina surface. Once loaded in the reactor, the catalysts are activated by sulfidation that converts transition metal oxides into the active so-called Co-Mo-S phase. In order to obtain a highly active sulfidic catalyst, the oxidic precursor should ideally consist of well dispersed molybdenum oxide monomers and small clusters on the surface of the support, as evidenced from extended X-ray absorption fine structure (EXAFS) and Raman spectroscopy [43-47]. Cobalt oxide should also be well dispersed on the surface, in close contact to the molybdenum species. Cobalt should preferentially be in octahedral coordination, as evidenced from Mössbauer measurements [48]. Other species formed are Co_3O_4 particles and $CoAl_2O_4$ spinel, formed by migration of cobalt ions to vacancies in the γ-Al_2O_3 lattice [48]. The active catalyst is obtained by sulfiding the oxide precursor in an H_2S/H_2 atmosphere. Surface molybdenum and cobalt in octahedral coordination form the active Co-Mo-S phase, consisting of layers of MoS_2 decorated with cobalt ions on the S-edges [48-50]. Typical particle lengths are 2 to 5 nm, as observed directly with transmission electron microscopy (TEM) and indirectly by EXAFS, when incorporating distorted Mo-atom positions at the particle edges in the analysis model [51-52]. Cobalt present as Co_3O_4 particles forms inactive Co_9S_8 upon sulfidation and cobalt present in $CoAl_2O_4$ does not sulfide; neither form of Co thus contributes to the catalytic activity.

Based on observations with transmission electron microscopy (TEM) and scanning tunneling microscopy (STM) on model catalyst supported on flat substrates along with density functional theory (DFT) calculations, the structure of MoS_2 is believed to be close to triangular platelets containing a layer of molybdenum atoms sandwiched between two layers of sulfur atoms [53-58]. The platelets can stack together to form crys-

tals of MoS_2. When cobalt promotes molybdenum sulfide the triangular platelets are truncated to hexagons with cobalt atoms replacing molybdenum atoms at the three new edges (see Figure 1.3) [54,56]. The active sites are believed to be the edges and corners of the (promoted) MoS_2 platelets depending on the size [55]. Recent TEM measurements on carbon supported industrial type hydrotreating catalysts confirm the structure determined on model systems by STM (see Figure 1.4) [59-60].

Hydrotreating of thiols, thioethers and ammines proceeds readily at industrial reaction conditions. More refractory sulfur compounds are aromatic heterocycles like thiophene, dibenzothiophene (DBT) and alkyl substituted DBT. Theses can either be directly desulfurized or undergo pre-hydrogenation, breaking the aromatic structure and making HDS proceed readily. Particularly, alkyl substituted DBT needs to be pre-hydrogenated, since access to the sulfur atom is sterically hindered. After breaking the aromatic structure, the molecules are no longer planar, facilitating HDS to proceed more easily.

The purpose of this study was to prepare alumina-supported and unsupported cobalt molybdenum hydrotreating catalysts by one-step flame synthesis, with all three metal components present in the precursor solution. The combination of high surface area and close contact between cobalt and molybdenum could be advantageous for the formation of the active Co-Mo-S phase, after sulfidation of a flame-made oxide precursor.

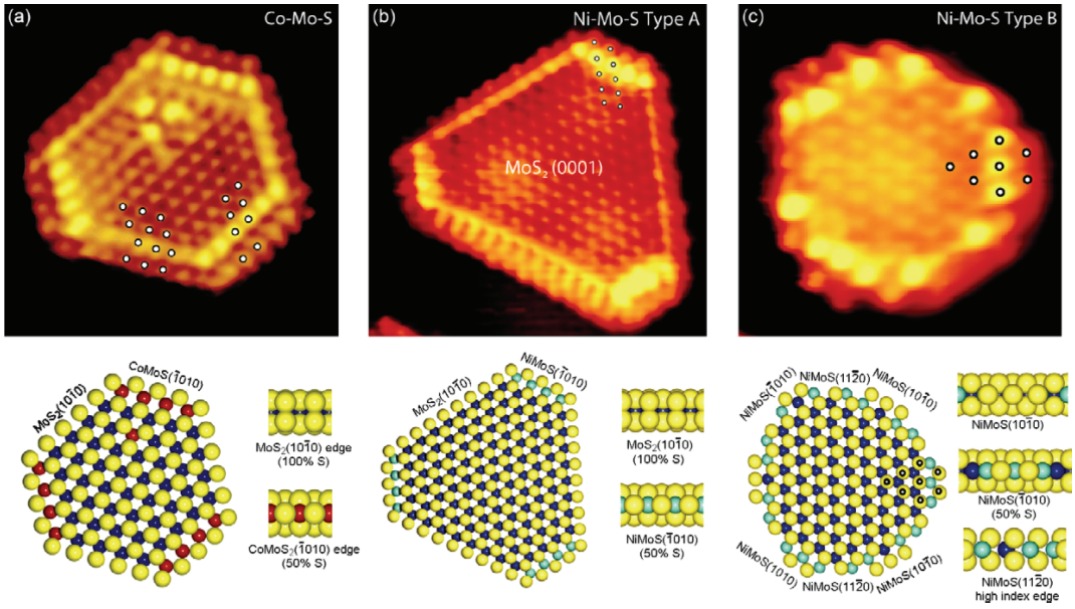

Figure 1.3: Top: Atom-resolved STM image of a hexagonally truncated Co–Mo–S and Ni–Mo–S nanoclusters supported on Au(111). The superimposed white dots illustrate the registry of protrusions on both types of edges. Bottom: A ball model (top and side views, respectively) of the nanoclusters based on DFT calculations. (Mo: blue; S: yellow; Co: red; Ni: cyan). Figure from ref. [53] with permission.

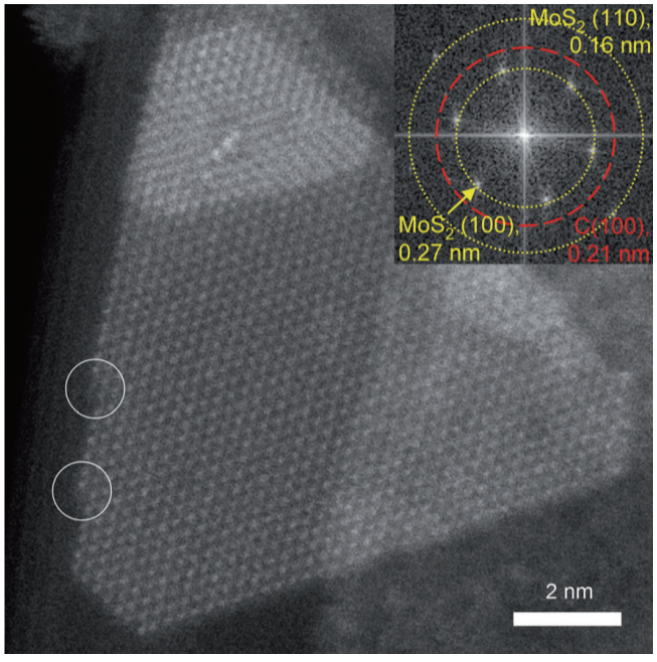

Figure 1.4: High-resolution STEM image of a MoS_2 nanocrystal supportedon a graphite support. Figure from ref. [59] with permission.

1.3 Oxidative dehydrogenation of propane

Upgrading C_2 to C_4 alkanes to the corresponding alkenes may become interesting processes to meet future demands for light alkenes [61], particularly for propene [62]. Light alkenes are mainly produced by fluid catalytic cracking (FCC), where they are byproducts in the upgrading of heavy oil fractions and by steam cracking, where the reaction conditions can be optimized to yield mainly ethene or mixtures of propene and butenes [62]. Processes for catalytic dehydrogenation of propane to propene have also been developed employing chromium or platinum based catalysts [63-64]. The major drawbacks of these three processes are the high energy consumption due to the endothermic reactions and coking of the catalysts and reactors, leading to deactivation and lower yields [62-63]. To overcome this problem some processes use multiple swing reactors where some are on-stream, while others are being regenerated [64].

Catalytic oxidative dehydrogenation of propane (ODP) is another process which could be employed for dedicated production of propene. This reaction is exothermic and the oxidizing reaction conditions eliminate the problem of coking, as long as the oxidant is not completely consumed [65]. Also, it could be operated auto-thermally [66]. The major drawback of ODP is lower selectivity, since propane, as well as the propene product, are easily combusted to CO and CO_2 [67]. So far, no catalyst with sufficient selectivity for industrial production of propene has been reported in the literature, despite high research and development activities [61].

Several types of catalysts have been reported in the literature, with strong attention to supported vanadium oxide [61]. In addition, supported molybdenum oxides have been intensively investigated [68-70], as well as different mixtures of molybdenum and vanadium oxide [71-73]. It was found that the reaction mechanism of ODP on vanadium

and molybdenum oxides is similar, although their activities are different with Mo being much less active [74-75]. It was also found that the support material greatly influences catalytic activity and selectivity of vanadia. ZrO_2 and TiO_2 resulted in high activity, Al_2O_3 in intermediate activity and SiO_2 in the lowest activity [76-78]. Generally the selectivity had the opposite trend of activity (see Figure 1.5).

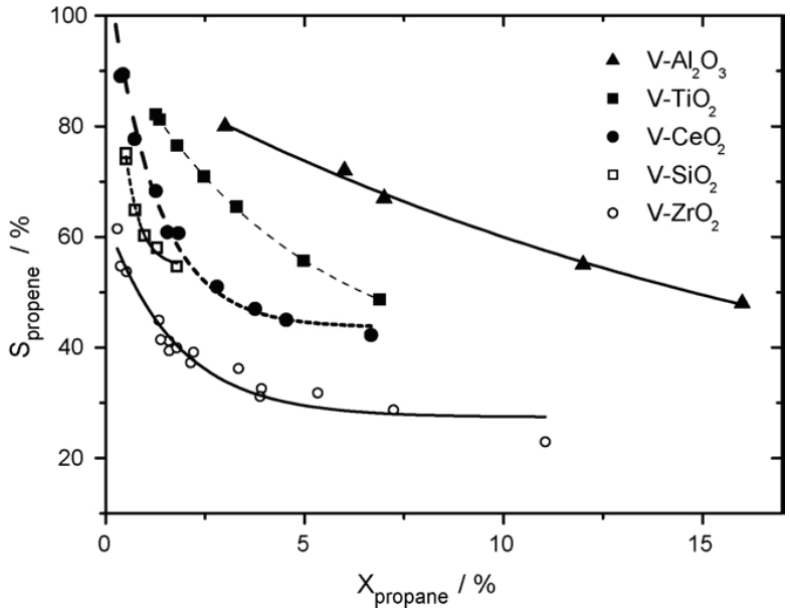

Figure 1.5: Selectivity–conversion trajectories for V-Al_2O_3, V-TiO_2, V-CeO_2, V-SiO_2 and V-ZrO_2 with low vanadium loadings at 400 ◦C. $C_3H_8/O_2/N_2$ = 29.1/14.5/56.4 at a total gas flowof 60 ml min^{-1}. Lines are to guide the eye. Figure from ref. [77] with permission.

According to recent density functional theory (DFT) calculations of silica supported vanadia, the first step in the ODP mechanism is C-H bond cleavage at the methylene group forming an adsorbed *iso*-propyl group [79-81]. The *iso*-propyl group can directly be converted to propene by a second C-H bond cleavage at one of the methyl groups or form an *iso*-propanol intermediate, which eliminates water to form propene [79,82]. If this occurs at an isolated $O=V^{5+}$ vanadyl site, a H_2O-V^{3+} site with adsorbed water is formed. Alternatively if two neighboring $O=V^{5+}$ vanadyl sites participate in the reaction

two HO-V^{4+} sites with hydroxyl groups are formed. The pathway with two HO-V^{4+} sites as the surface product is energetically favorable compared to a single H_2O-V^{3+} site. The reduced catalyst surface is re-oxidized to O=V^{5+} by oxygen from the gas phase through peroxovanadate intermediates [83]. Peroxide species have also been suggested to participate in the mechanism on the basis of an O-O stretching band around 930 cm^{-1} in Raman spectroscopy measurements and DFT calculations [84-85]. However, this interpretation has been questioned and other interpretations of the Raman band around 930 cm^{-1} have been proposed [86-87]. Peroxovanadates are thus more likely to be intermediates in the re-oxidation of the catalyst surface. Peroxovanadates and other adsorbed electrophilic oxygen species like H_2O_2, $HOO^{\bullet}$, O_2^- and O^- are active in the complete oxidation of propane and propene to CO and CO_2 [83,88]. O=V^{5+} vanadyl sites are also active in the complete oxidation of propene, but less than electrophilic oxygen species [83].

Kinetic investigations have been performed, and a reaction scheme consisting of the ODP reaction, parallel combustion of propane and sequential combustion of propene (see Scheme 1.1), all first order in hydrocarbon and zeroth order in oxygen, is generally accepted [67,75,89-97]. From these studies it was concluded, that the best propene yields is obtained at high temperature, where the ratio of the propene combustion rate constant to the ODP rate constant is minimized. However, this also maximizes the ratio of the propane combustion rate constant to the ODP rate constant. Hence, the interplay between all three reactions must be considered to determine the optimal reaction conditions.

$$C_3H_8 + \frac{1}{2}O_2 \longrightarrow C_3H_6 + H_2O$$

$$C_3H_8 + \left(2 + \frac{3}{2}x\right)O_2 \longrightarrow 3CO_x + 4H_2O$$

$$C_3H_6 + \left(\frac{3}{2} + \frac{3}{2}x\right)O_2 \longrightarrow 3CO_x + 3H_2O$$

Scheme 1.1: Reaction network of oxidative dehydrogenation of propane.

Alumina supported vanadia catalysts have been prepared by FSP by Rossetti and co-workers [98]. The specific surface areas obtained in their study ranged from 18 to 27 m^2/g, approximately a factor 5 to 10 lower than typical alumina supported catalysts prepared by FSP [15]. SEM images reported by Rossetti et al. [98] also showed a very broad particle size distribution. This may be due to the use of aluminum nitrate as precursor, which contains large amounts of water, so that the combustion enthalpy of the precursor solution may have been too low for fast evaporation of the precursor droplets. Another reason could be the low dispersion gas pressure drop across the nozzle leading to larger precursor droplets [99], which evaporate slowly. Consequently crystalline V_2O_5 and $AlVO_4$ were produced rather than supported vanadia species.

The aim of this study was to prepare high surface area vanadia, molybdenum oxide and mixed molybdenum-vanadium oxide on alumina catalysts by FSP and investigate the structure-activity-selectivity relationship of oxidative dehydrogenation of propane as function of transition metal loading. For this purpose vanadium and aluminum acetylacetonates and molybdenum 2-ethylhexaoate, dissolved in the high combustion enthalpy solvent toluene, were used as precursors during flame synthesis.

1.4 Outline of this thesis

Further exploring FSP as a method for synthesis of thermally stable and high surface area catalysts is interesting. This thesis explores the use of FSP for the synthesis of cobalt-molybdenum hydrotreating catalysts and vanadium and molybdenum oxide catalysts for oxidative dehydrogenation of propane (ODP). The experimental of FSP and a newly constructed catalytic activity test setup are described in Section 2. The hydrotreating experiments started with FSP synthesis of $CoMo/Al_2O_3$ catalysts (Section 3). This resulted in undesired formation of $CoAl_2O_4$. To minimize the formation of $CoAl_2O_4$, the hydrotreating catalyst preparations continued with two-nozzle FSP synthesis of $CoMo/Al_2O_3$ catalysts (Section 4) and one-nozzle synthesis of $CoMo/Al_2O_3$-SiO_2 catalysts (Section 5).

The ODP experiments started with FSP synthesis and structural characterization of vanadia on alumina catalysts (Section 6) and a kinetic description of the ODP reaction over these catalysts (Section 7). This was continued by synthesis of alumina supported molybdenum oxide and mixed molybdenum-vanadium oxide (Section 8). Finally, conclusions and outlooks are given in Section 9.

2. Experimental

2.1 Flame spray pyrolysis (FSP)

The FSP setup at the Department of Chemical and Biochemical Engineering at the Technical University of Denmark is designed like the schematic in Figure 1.1 and photographs of the setup are shown in Figure 2.1 and Figure 2.2. The nozzle (Figure 1.1 and Figure 2.3) and filter holder were designed and constructed at ETH Zürich. The capillary has a 0.413 mm inner diameter (Hamilton Gauge 22), and is placed in the capillary holder which can move vertically to adjust the dispersion gas pressure drop across the nozzle, typically 1.5 to 3 bar. If the pressure drop is lower than 1.5 bar, large droplets are formed in the spray, while the droplet size asymptotically reaches about 5 μm with increasing the pressure drop [3]. The precursor is loaded in a 100 ml gas tight syringe (Hamilton), which is placed in a syringe pump (World Precision Instruments ALADDIN), that is calibrated to the inner diameter of the syringe, allowing flows between 0.1 and 10 ml/min, but typically 3 to 7 ml/min is used. Generally, higher flows result in larger primary particles due to the larger flame and longer residence time at high temperature [27,100-102], however the particle size of pure silica behaves non-monotonously as function of precursor flow [3,28].

Gas flows for the dispersion gas and pilot flame are controlled by calibrated mass flow controllers (Brooks) allowing up to 10 Nl/min for the oxygen dispersion gas and 5 Nl/min for the pilot flame oxygen and methane, but typically 3 to 7 Nl/min for the dispersion gas is used. Generally, the higher the flow of dispersion gas the smaller the primary particle size, due to a smaller flame and shorter residence time with increasing oxidant flow [27,100-101].

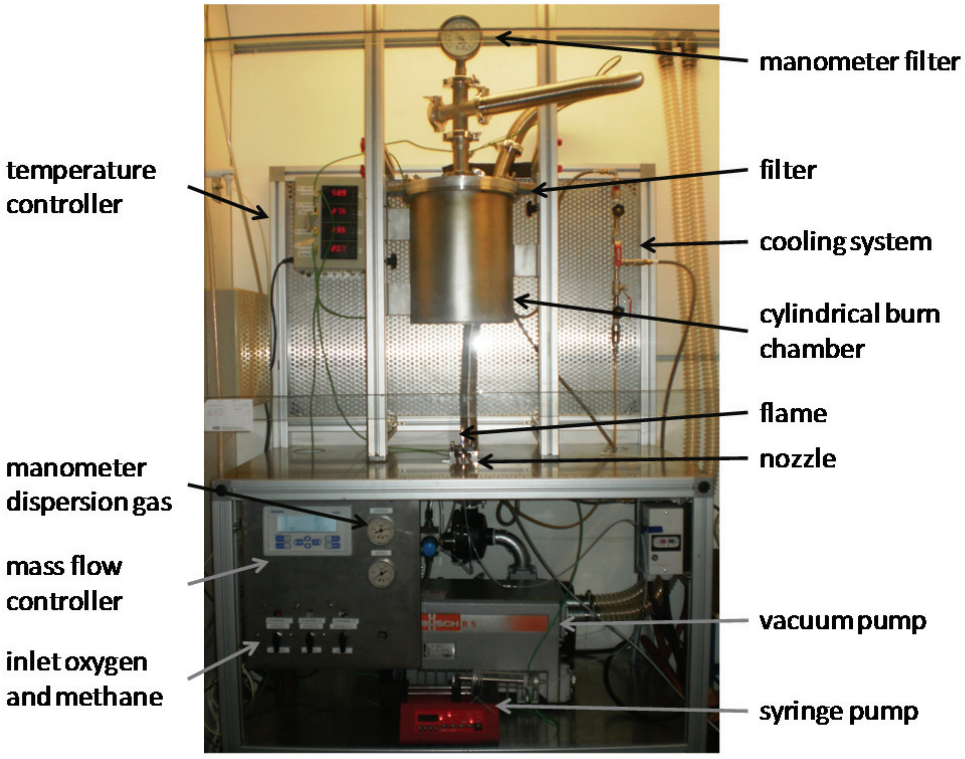

Figure 2.1: Photograph of the FSP setup with the different components labeled. The whole set-up is placed in a fume hood.

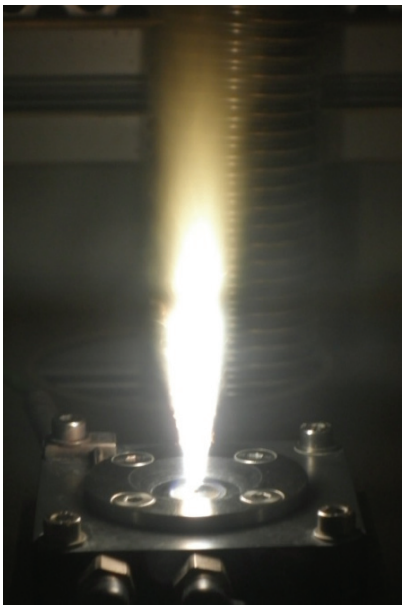

Figure 2.2: Photograph of the FSP flame in action preparing MoO_x/Al_2O_3 catalyst. The yellow flame color in the top is due to molybdenum.

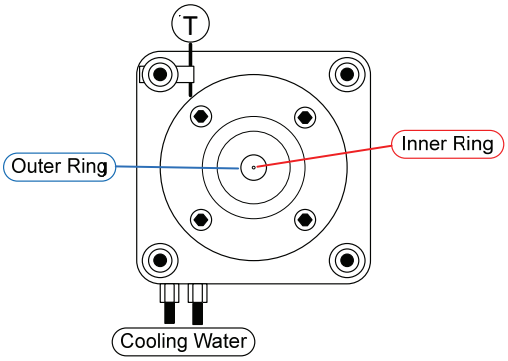

Figure 2.3: Top view of the FSP nozzle. The inner ring is the capillary and dispersion gas outlet and the outer ring is the CH_4/O_2 pilot flame.

The pilot flame is typically operated at 3 Nl/min oxygen and 1 Nl/min methane, which is 50 % excess oxygen in the pilot flame for a stable flame and rapid burnout.

Above the flame, a filter holder designed for 257 mm diameter filters was rebuild to accommodate 240 mm filters (Whatman GF6). Both the nozzle and the filter holder are water cooled and thermocouples monitor the temperature just above the filter and close to the nozzle. The temperature on the filter depends on the height above the flame (which is adjustable), the precursor flow and the combustion enthalpy of the precursor solution. Preferably, filter temperatures above 150 °C are avoided. The flow through the filter is maintained by a vacuum pump (Bush R5 0063) capable of a flow of 63 m^3/h at atmospheric pressure, which decreases as the pressure drop across the filter increases, when the filter cake build up. A manometer monitors the pressure drop, which is typically around 450 to 700 mbar at the end of the FSP synthesis.

Typically, 50 ml of a precursor solution containing 0.1 to 0.5 mol/l metal was burned and collected on a single filter, allowing about 400 to 550 mg of material to be recovered and normally two filters were prepared in each synthesis. The solid materials were recovered by scraping the filter with a spatula and sieving the material through a 600 μm sieve, to remove large pieces of filter material that may come loose during scraping. However, small amounts of fine filter material pieces are unavoidable in the product and could slightly affect the surface area measurements and the catalytic activity measurements, where accurate weighting is essential, but the filter material is expected to be catalytically inactive.

2.2 Catalytic activity measurements setup

A new catalytic activity test setup using micro reactors for 50-500 mg of sieved catalyst, total gas flow 30-300 Nml/min, temperature 200-850 °C and near ambient pressure was

in-house designed and commercially build (ChimneyLab Europe) for oxidative dehydrogenation of propane.

A photograph of the setup is shown in Figure 2.4 and the PI-diagram is shown in Figure 2.5. It contains three primary parts: 1) Gas mixing, 2) three U-shaped tubular reactors and 3) GC-MS gas analysis.

1. Gas mixing is performed by four calibrated mass flow controllers (MFC, Brooks) for mixing nitrogen, oxygen (two MFCs for low and high flow respectively) and propane. Parallel to the gas mixture, a single MFC can supply dry air to the reactors for oxidative pretreatment of the catalyst.
2. Three U-shaped quartz tubular flow reactors (4 mm inner diameter) are connected to the gas-mix and the air in a series/by-pass configuration using six 4-way valves. The reactors are placed in 50 mm diameter tubular furnaces closed in one end with individual temperature control (Watlow). Each reactor can either be supplied with the gas mixture, the dry air or be in a closed loop and disconnected without interfering with the other reactors. Each furnace can be moved away from the reactors individually.
3. A fraction of the gas mixture is delivered to the GC-MS (Thermo Fischer, Global Analyzer Solutions) for analysis after passing through one reactor or by-passing them all. The remaining gas mixture and the air are sent to the exhaust. The GC has a TCD detector for quantifying N_2, O_2, CO and CO_2 using Hayesep Q and Molsieve 5A packed columns and a FID detector, in parallel with the MS, for identifying and quantifying saturated and unsaturated light hydrocarbons and oxygenated byproducts such as acrolein using a Rt-QS-BOND column (Restek). Quantification was done by integrating the TCD or FID signals and calculating the mole fractions of

the species from straight line calibrations. The calibrations were made with certified calibration gasses (AGA and Air Liquide). A gas analysis takes about 26 min.

Figure 2.4: Photograph of the oxidative dehydrogenation activity test setup. From left: Electricity cupboard (grey painted metal), gas mixing panel, three furnaces and reactors (in polycarbonate enclosure) and GC-MS on the table.

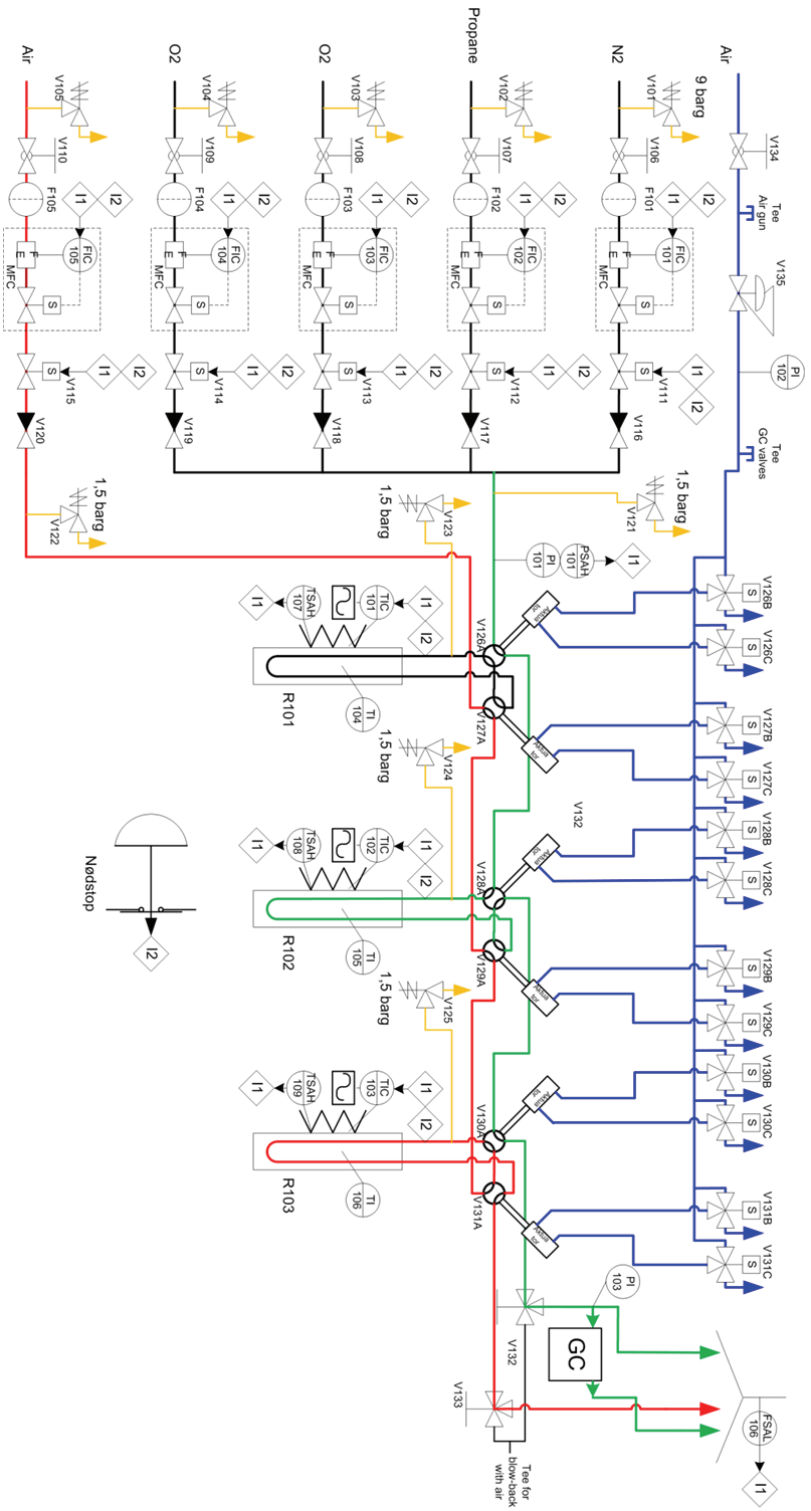

Figure 2.5: PI-diagram of the oxidative dehydrogenation activity test setup. As drawn reactor one (R101) is isolated for loading/unloading, reactor two (R102) has the flow of the gas mixture (green line) and reactor three (R103) has the flow of dry air for pre-oxidation (red line).

A thermocouple was placed inside each reactor just touching the catalyst beds to measure the reaction temperature. A pressure transducer placed upstream of the reactors measured the actual reaction pressure, which was kept close to atmospheric pressure. A pressure transducer downstream of the reactor, near the inlet of the GC, enabled measurement of the pressure drop across the catalyst bed.

After the first reactor all the tubes are heat traced to 150 °C to avoid condensation of water. All MFC set-points, valve positions, reactor temperatures and start of GC-MS analysis are controlled by a PLC. A PC running a LabView program is used to control the set-points and for data logging of process values (see Figure 2.6). All parameters can be controlled manually or automatically using a reaction sequence.

A typical catalytic activity measurement would start with oxidizing the sample in air at 550 °C. Following this treatment, the sample is cooled to the lowest reaction temperature and the air flow is swapped for the gas mixture. The exit gas composition is analyzed with GC-MS at different flows, concentrations and/or temperatures.

The test setup is designed for gas-phase oxidation of alkanes, but it can also be used for other gas-solid catalytic reactions at near ambient pressure and temperatures up to 850 °C. With the addition of live gas analysis like FTIR or MS it is possible to use the setup for temperature programmed desorption, reduction and oxidation.

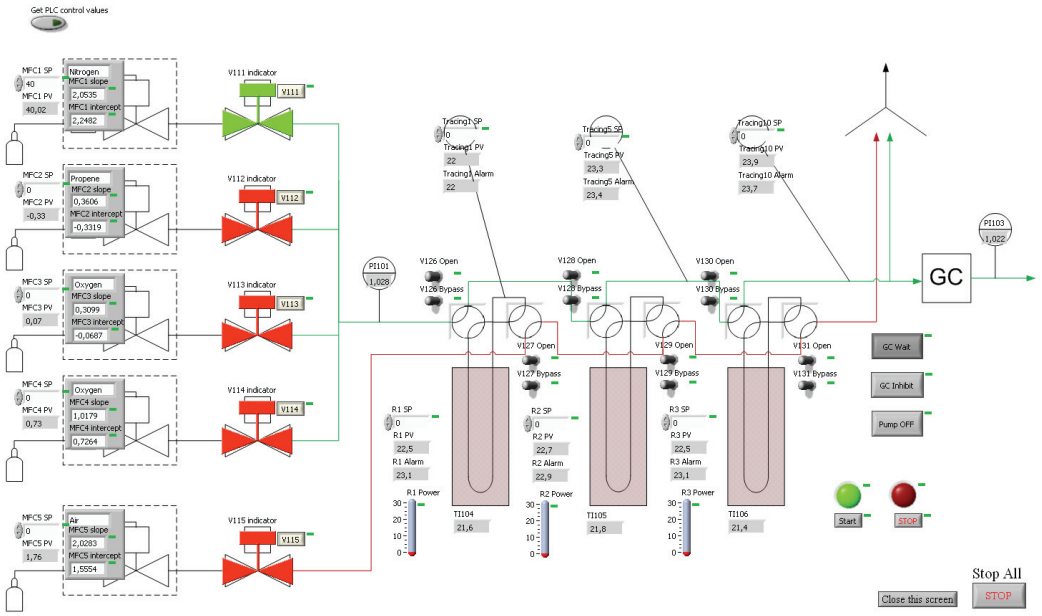

Figure 2.6: LabView control screen of the oxidative dehydrogenation activity test setup showing from left to right: MFC control, pressure reading, furnace temperature reading and control, heat-tracing temperature reading and control, GC inputs and pressure reading.

3. Flame spray synthesis of $CoMo/Al_2O_3$ hydrotreating catalysts

3.1 Introduction

In order to evaluate the potential of FSP for synthesizing the $CoMo/Al_2O_3$ oxide catalyst precursor of molybdenum sulfide hydrotreating catalysts, a series of $CoMo/Al_2O_3$ catalysts with different transition metal loadings were prepared by FSP. The series was structurally characterized and evaluated as hydrotreating catalysts after activation by sulfidation.

3.2 Experimental

3.2.1 Catalyst synthesis

Six alumina supported catalysts and one unsupported CoMo catalyst were prepared by one-step flame spray pyrolysis [3-4], with 8, 16, 24 and 32 wt.% Mo with atomic ratio Co/Mo = 1/3, 16 wt.% Mo with atomic ratios Co/Mo = 2/3 and 1/1, and unsupported CoMo-oxide with Co/Mo = 1/3 were prepared (cf. Table 3.1).

Precursor solutions were prepared by dissolving appropriate amounts of tris(acetylacetonato)aluminum ($Al(C_5H_7O_3)_3$; Sigma Aldrich), cobalt 2-ethyhexanoate ($Co[OOCCH(C_2H_5)C_4H_9]_2$; Sigma Aldrich) and molybdenum 2-ethyhexanoate ($Mo[OOCCH(C_2H_5)C_4H_9]_x$; Strem Chemicals) in toluene (Sigma Aldrich) to a total metal concentration of 0.4 mol/l. The total metal concentration was limited by the solubility of the aluminum compound.

The precursor solution was fed at 3 ml/min and dispersed by 7 Nl/min high-velocity oxygen gas at 2 bar pressure drop. The temperature at the filter was kept below 110 °C. At the end of the synthesis the pressure drop across the filter was 0.6 to 0.7 bar and 0.45 to

0.8 g of product could be collected from each filter. Two batches were prepared for each sample using the same precursor solution. Details of FSP experimental are found in Section 2.

3.2.2 Specific surface area

Specific surface areas (SSA) of the as-prepared oxide catalysts and the sulfide catalysts after catalytic activity measurements were measured by nitrogen adsorption at its boiling point (Quantachrome iQ_2), using multipoint BET theory, with six points in the p/p_0 = 0.05 to 0.25 range. Prior to adsorption, the oxide catalysts were degassed in a flow of dry nitrogen at 170 °C and the sulfide catalysts, which had been pressed and sieved before sulfidation, were degassed at 350 °C in vacuum. The spherical equivalent particle size was calculated as $d_p = 6/(\rho \cdot SSA)$, where ρ is the average density of 4.25 g/cm^3 which is weighted by the mass percentages of the oxides Al_2O_3, MoO_3 and CoO.

3.2.3 X-ray diffraction

X-ray diffraction was measured on the as-prepared oxide powders using rotating sample holders, a rotating copper anode X-ray source, nickel filter and automatic anti-scatter and divergence slits (PANalytical X'Pert PRO). 4615 points were recorded from 2θ = 10 to 70° with 327 s integration time pr. point in continues scanning mode.

3.2.4 UV-vis diffuse reflectance spectroscopy

UV-vis diffuse reflectance spectra were recorded on the as-prepared oxide powders using a Varian Cary 300 Bio spectrophotometer equipped with a Labsphere DRA-CA-30I integrating sphere. Spectralon was used as reference and the spectra were analyzed using the Kubelka-Munk theory were $F(R_\infty) = (1-R_\infty)^2/2R_\infty$, where R_∞ is the percentage re-

flection of an infinite layer of powder relative to the reference (i.e. there is no transmission through the sample cup).

Table 3.1: Specific surface area (SSA) and crystal phases observed with XRD and UV-vis of the oxide precursor and SSA of the spent sulfide catalyst.

Sample	SSA_o[a] (m^2/g)	SSA_s[b] (m^2/g)	SSA ratio[c]	Phases[d]
8 wt.% Mo Co/Mo = 1/3	221	190	0.86	γ-Al_2O_3, $CoAl_2O_4$
16 wt.% Mo Co/Mo = 1/3	202	120	0.59	γ-Al_2O_3, $CoAl_2O_4$
24 wt.% Mo Co/Mo = 1/3	163	78	0.48	γ-Al_2O_3, $CoAl_2O_4$
32 wt.% Mo Co/Mo = 1/3	126	78	0.48	γ-Al_2O_3, MoO_3, $CoAl_2O_4$
Unsupported Co/Mo = 1/3	90	34	0.38	MoO_3, β-$CoMoO_4$
16 wt.% Mo Co/Mo = 2/3	205	91	0.44	γ-Al_2O_3, $CoAl_2O_4$
16 wt.% Mo Co/Mo = 1/1	191	70	0.37	γ-Al_2O_3, $CoAl_2O_4$

[a]SSA of the as-prepared oxide catalysts, [b]SSA of the spent sulfide catalyst, [c]ratio between the surface areas of the as-prepared and the spent catalysts, [d]phases detected with XRD and UV-vis.

3.2.5 Transmission electron microscopy

Bright field transmission electron microscopy (Technei T20) was measured on powders supported on lacey carbon copper grids. The as-prepared, oxidic catalyst powder was transferred to the grid by dipping it several times in the powder and removing loosely bound excess. The spent sulfide catalysts were crushed in an agate mortar prior to transfer.

3.2.6 Catalytic activity measurements

The hydrotreating catalytic activity measurements were performed in the laboratories of Haldor Topsøe A/S.

The as-prepared catalyst powder was pressed into pellets by means of an hydraulic press. The pellets were crushed to yield 300 mg of the 600-850 μm sieve fraction, which

was diluted with 200 μm Ballotini glass beads to a bed height of 8 mm for good mass and energy transfer and placed in a fixed bed tubular flow reactor (7.5 mm inner diameter) around a thermocouple pocket (see Figure 3.1). The liquid feed to the reactor was evaporated and mixed with a hydrogen stream upon entering the reactor. The catalysts were sulfided in-situ for 4 hours at 350 °C and a total pressure of 50 atm arising from a liquid feed of dimethyldisulfide (DMDS) dissolved in *n*-heptane and from hydrogen at a partial pressure $p(H_2)$ = 42 atm. At these conditions all species are in the gas phase and DMDS decomposes to hydrogen sulfide and methane. After sulfidation, the liquid feed is switched to a model diesel composed of 3.0 wt.% dibenzothiophene (DBT), 0.5 wt.% indole, 1.0 wt.% naphthalene, 2.5 wt.% DMDS and 0.5 wt.% *n*-nonane dissolved in *n*-heptane. During the activity testing the total pressure was fixed at 50 atm and $p(H_2)$ = 38 atm. The total liquid feed rate was 0.5 ml/min and the hydrogen feed rate was 250 Nml/min. DBT is a representative sulfur compound, indole a representative nitrogen compound, naphthalene a representative aromatic compound for unhydrotreated diesel, DMDS is added to keep the catalyst sulfided (i.e. maintain a sufficient partial pressure of H_2S during the activity measurements) and *n*-nonane is an internal standard for GC analysis. Concentrations were determined using GC-FID analysis, measuring the conversion of the feed compounds and the formation of biphenyl by direct desulphurization and cyclohexyl benzene by pre-hydrogenation (hydrogenation of one benzene ring followed by sulfur removal). Conversions were calculated by integrating peaks in the chromatogram and ideally kept below 50 %. DBT, biphenyl and cyclohexyl benzene mass balances were better than 99 % in all measurements. Activity tests lasted approximately 8 h and 8 GC-FID analyses were made. Apparent pseudo first order rate coefficients for the desulfurization, denitrogenation and hydrogenation reactions were calcu-

lated when constant conversion was observed by $k = -F_v \cdot \rho_{feed}/w_{cat} \cdot \ln(1-x)$ where F_v is the volumetric flow rate, ρ_{feed} the density of the feed, w_{cat} the mass of catalyst and x the conversion of DBT, indole and naphthalene respectively.

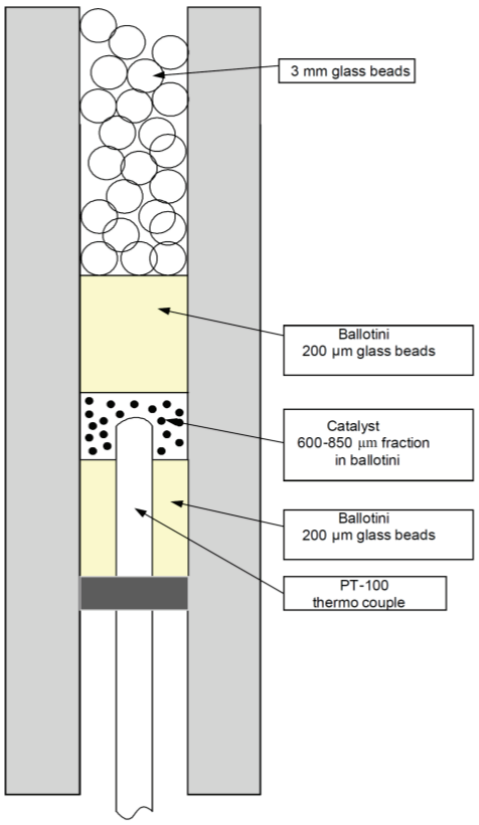

Figure 3.1: Cross section of the high-pressure reactor used for hydrotreating catalyst activity measurements in the laboratories of Haldor Topsøe A/S.

3.3 Results and discussion

Seven $CoMo/Al_2O_3$ samples were synthesized by flame spray synthesis, where an organic precursor solution containing organic compounds of all three metallic elements is sprayed as fine droplets into a flame. Combustion of the solvent and precursors result in a short residence time at high temperature, where metal oxide vapors nucleate, grow and agglomerate to form agglomerated nanoparticles. The flame product, which is the oxide

catalyst precursor similar to what is obtained after calcination in conventional hydrotreating catalyst production, was characterized by different physiochemical techniques and was evaluated as hydrotreating catalyst after sulfidation.

The specific surface area (SSA) and the phases detected by XRD and UV-vis of the oxide samples and the SSA of the spent sulfidic catalysts are summarized in Table 3.1. The SSA decreased from 221 to 90 m^2/g when increasing the Mo and Co contents. At 8 and 16 wt.% Mo the obtained SSA was just above 200 m^2/g, which is similar to what can be expected from a catalyst prepared by active metal impregnation of high-surface area alumina. After the catalytic tests, during which a sulfidation of the molybdenum oxide and partially the cobalt oxide occurs, the SSA had decreased significantly when the active metal loads were high. The ratio of the SSA before and after catalytic tests clearly shows that increasing the Mo and Co content makes the sample more prone to sintering.

3.3.1 UV-vis spectroscopy

UV-vis spectra recorded on the as-prepared oxide powders are shown in Figure 3.2. In the visible region, three clear peaks are observed at 548, 583 and 630 nm on all samples with alumina support. These are the three spin allowed *d–d* transitions of Co^{2+} in $CoAl_2O_4$ spinel [103], where Co is tetrahedrally coordinated (by oxygen), thus the *d–d* transitions have high absorption coefficients by being symmetry allowed. The higher the Co content, the higher the intensity of the transitions. Thus under the conditions in the flame the spinel phase is formed from CoO_x and AlO_x vapors. The triplet is absent for the unsupported sample, but some absorbance in the visible region is observed indicating the presence of cobalt. This is in good agreement with the alumina-supported samples appearing blue and the unsupported sample appearing brown. Absorbance in

the UV-region (<400 nm) is due to molybdenum ligand-to-metal charge transfer bands ($O^{2-} \rightarrow Mo^{6+}$) [104]. Higher energy bands centered around 240-270 nm have been assigned to monomeric tetrahedral molybdenum species, while bands centered around 290-320 nm have been assigned to oligomeric octahedral molybdenum species [45,104-105]. In this study two distinct peaks were not observed, except for the 8 wt.% sample where a shoulder to the high energy peak is seen around 300 nm. The absorbance between 300 and 400 nm increases with increasing Mo loading indicating increased oligomer formation with increasing metal loading. This is particularly pronounced for the unsupported sample. It was also observed that cobalt compounds such as $Co(NO_3)_2$, $Co(OH)_2$ and basic cobalt carbonate absorbed in the UV region, so cobalt charge transfer transitions may contribute to the observed UV bands.

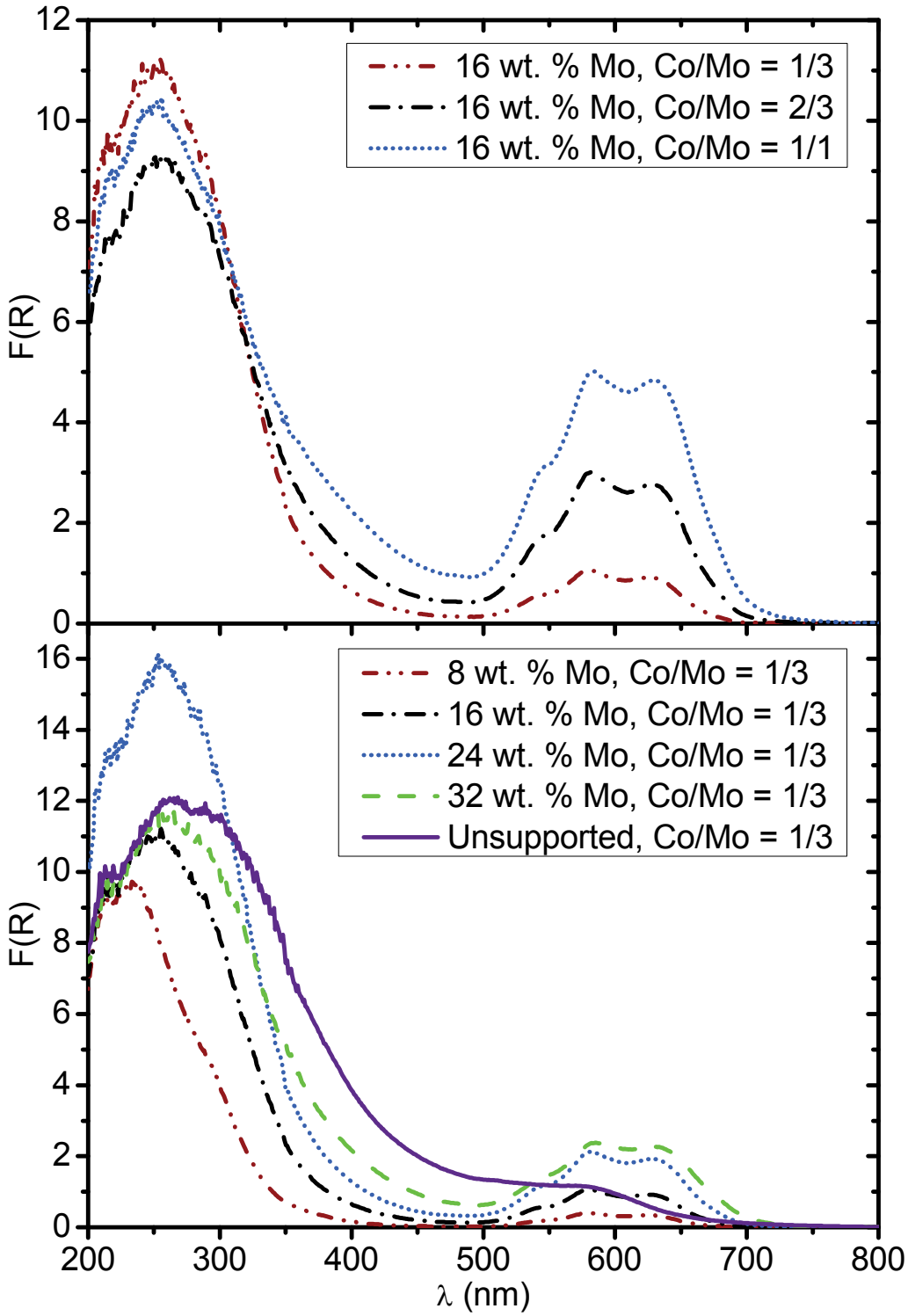

Figure 3.2: Diffuse reflectance UV-vis spectra of the as-prepared $CoMo/Al_2O_3$ oxide powders. The triplet seen at 548, 583 and 630 nm is due to $CoAl_2O_4$ spinel. Absorption in the UV region (< 400 nm) is due to molybdenum species charge transfer bands.

3.3.2 X-ray diffraction

X-ray diffractograms of the as-prepared oxide powders are shown in Figure 3.3. At 8 to 24 wt.% Mo only the reflections for pure γ-Al_2O_3 (which was also prepared by FSP) are observed, indicating that Mo and Co are well dispersed rather than forming separate molybdenum and cobalt oxide particles. Previous FSP prepared alumina also showed the γ-Al_2O_3 phase [16-17]. At 32 wt.% a new reflection at $2\theta = 26°$ appears, which is observed as an intense reflection for the unsupported sample. The unsupported sample is a mixture of MoO_3 and $CoMoO_4$ and the 32 wt.% sample is mostly γ-Al_2O_3 with small amounts of MoO_3 and $CoAl_2O_4$, i.e. still well dispersed. Increasing the Co loading with constant Mo wt.% caused the $2\theta = 67°$ (440) reflection to shift to 66°, the (422) reflection at $2\theta = 54°$ appears, while the $2\theta = 46°$ (400) reflection diminished and the $2\theta = 37°$ (311) reflection increased in intensity. This indicates a shift from the formation of γ-Al_2O_3 towards $CoAl_2O_4$, which has a similar XRD pattern, as shown by the diffractogram of a commercial $CoAl_2O_4$ sample (cf. Figure 3.3). This is in good agreement with the UV-vis measurements and shows that significant amounts of $CoAl_2O_4$ are formed. The spinel is an undesired product of the flame synthesis, since this cobalt has been shown not to be available for promotion in the sulfided catalyst [50]. For the 16 wt.% Mo sample with Co/Mo = 1/1 ratio, which has the highest Co content of all the samples, the Co/Al atomic ratio is 0.137. According to the stoichiometry a maximum of 27 % of the alumina can form $CoAl_2O_4$. For the 16 wt.% Mo sample with Co/Mo = 2/3 there is also some indication of formation of Co_3O_4, which XRD diffractogram is similar to those of γ-Al_2O_3 and $CoAl_2O_4$. The signs of Co_3O_4 are the weak reflection at $2\theta = 20°$ (111) and the relative high intensity of the $2\theta = 32°$ (220) reflection. For the 16 wt.% Mo sample with Co/Mo = 1/1 there is also some indication of MoO_3 formation by the

broad reflection around $2\theta = 26°$, observed as the most intense reflection for the unsupported sample. The mixtures of phases with overlapping peaks made the estimation of crystallite sizes using the Scherrer equation very inaccurate.

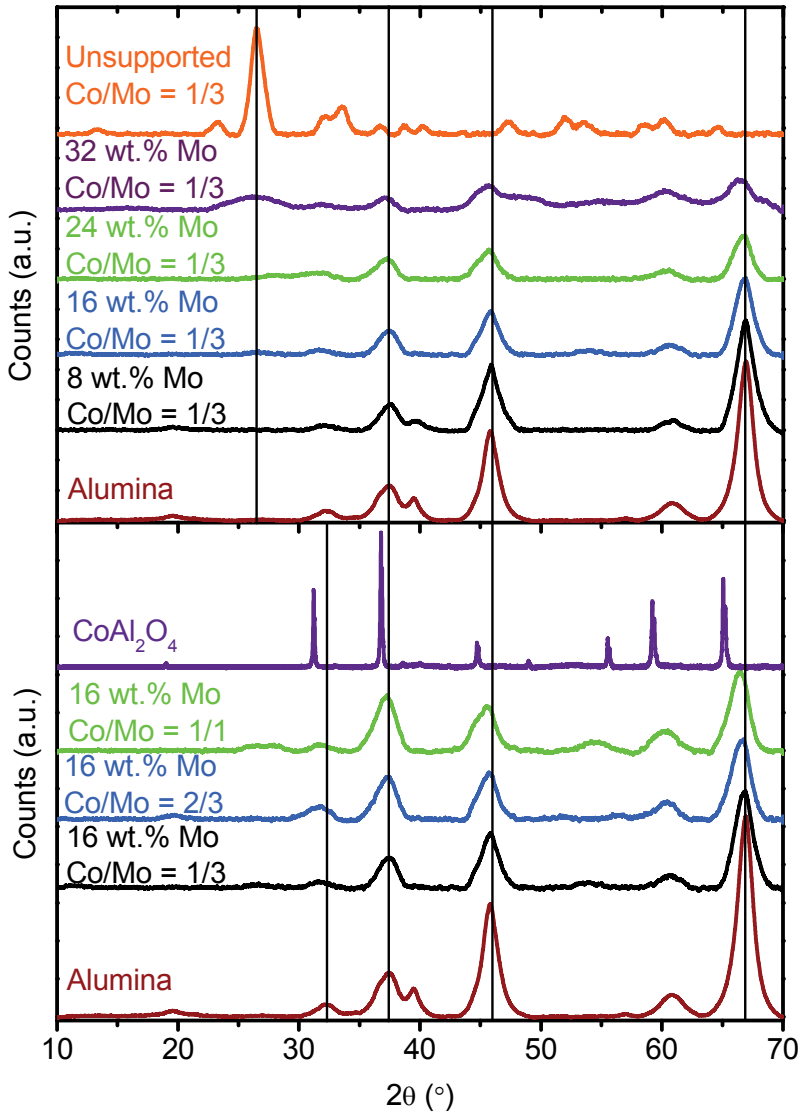

Figure 3.3: X-ray diffractograms of the as-prepared $CoMo/Al_2O_3$ oxide catalyst precursors. Up to 24 wt. % Mo only the reflections from γ-Al_2O_3 (also prepared by FSP) are observed. At 32 wt.% Mo the reflection at $2\theta = 26°$ is observed, which is seen as the most intense reflection of the unsupported sample. Increasing the Co content at constant Mo loading of 16 wt.% causes small changes in the diffractogram showing the formation of $CoAl_2O_4$, as compared to the diffractogram of a commercial $CoAl_2O_4$ sample (Alfa Asear, divided by a factor 5).

3.3.3 Transmission Electron Microscopy

The as-prepared oxide catalysts were investigated with TEM to gain further information on particle morphology and size distribution. Selected images of six samples are shown in Figure 3.4. The flame products are aggregated, polydisperse nanoparticles. The larger particles are almost spherical, while the smaller ones are more irregular. At low molybdenum loadings the particles agglomerate, but the individual particles can clearly be distinguished on the TEM images, indicating that they are held together by van der Waals forces. At 24 and 32 wt.% Mo and particularly on the unsupported samples, the particles have started to sinter and aggregate. This may be due to the lower melting point of molybdenum oxide compared to alumina, enhancing the rate of sintering.

Based on measuring the diameter of N = 150 to 250 particles for each sample, the average particle diameter was calculated as $d_p = (\sum d_i)/N$ and shown in Figure 3.5, along with the BET surface area equivalent diameter assuming spherical particles and estimating the average density from the composition and the densities of the bulk oxides $d_p = 6/(SSA \cdot \rho)$. The average particle size determined with TEM is generally slightly larger than the BET derived size, which may be due to the irregular shape of the particles.

The unsupported sample is an exception since the TEM particle size is smaller than the BET particle size. This may be due to the difficulty in determining the appropriate size of the individual particles, due to the high degree of sintering. The variation in particle size is also large, as shown by the one standard deviation error bars in Figure 3.5. This is particularly pronounced as the molybdenum content is increased. Figure 3.6 shows the fitted log-normal particle size distributions, normalized to unit area under the curve, demonstrating that the standard deviation increases when going from 8 to 32 wt.% Mo and it is even higher for the unsupported sample. The insert in Figure 3.6 shows the

counts binned in 1 nm intervals and the fit for the 16 wt.% Mo sample. For all samples a log-normal distribution fitted the measured particle size distribution well.

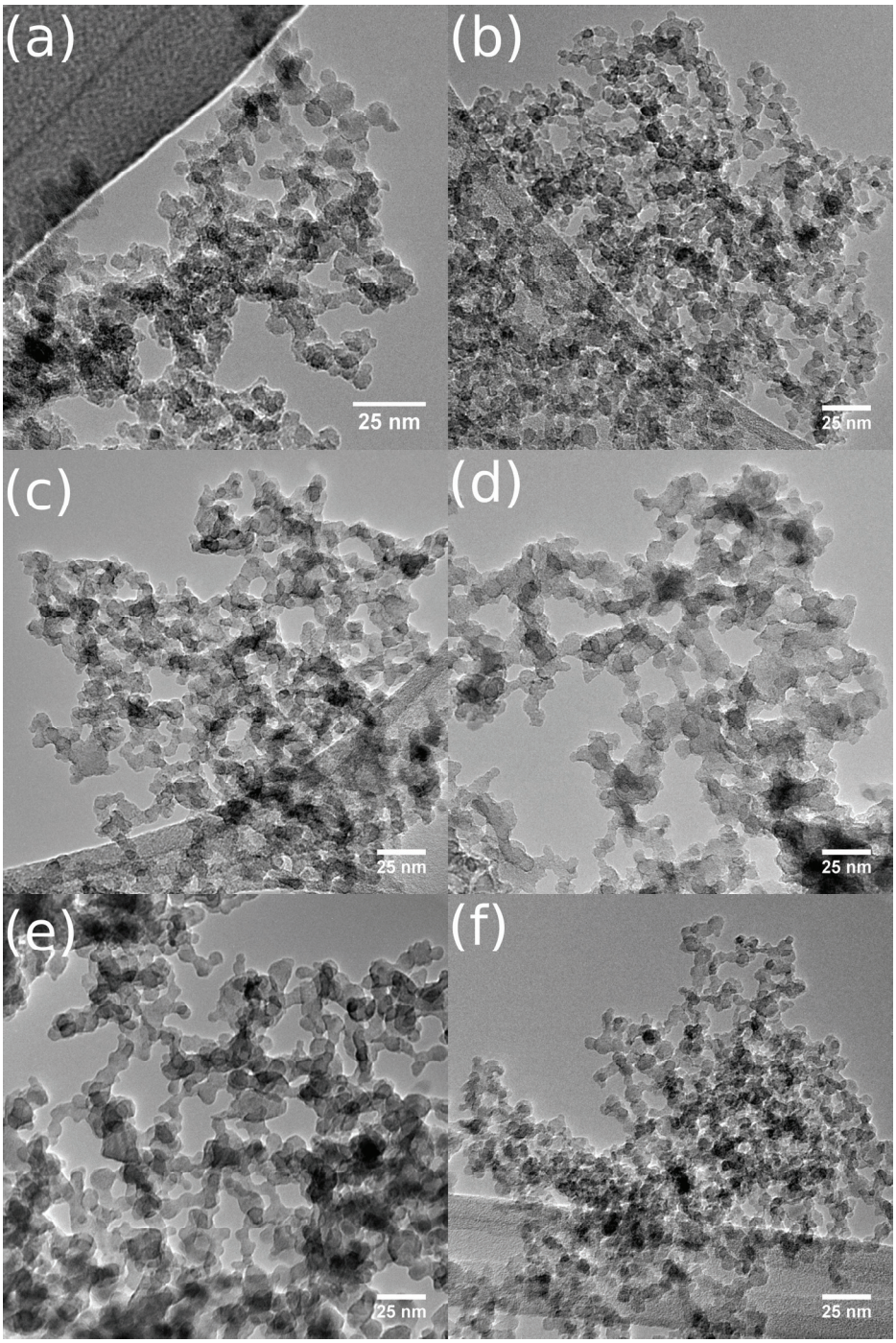

Figure 3.4: Bright field TEM images of the as-prepared oxide catalysts. (a) 8 wt.% Mo, Co/Mo = 1/3 (note different scale), (b) 16 wt.% Mo, Co/Mo = 1/3, (c) 24 wt.% Mo, Co/Mo = 1/3, (d) 32 wt.% Mo, Co/Mo = 1/3, (e) Unsupported, Co/Mo = 1/3 and (f) 16 wt.% Mo, Co/Mo = 1/1.

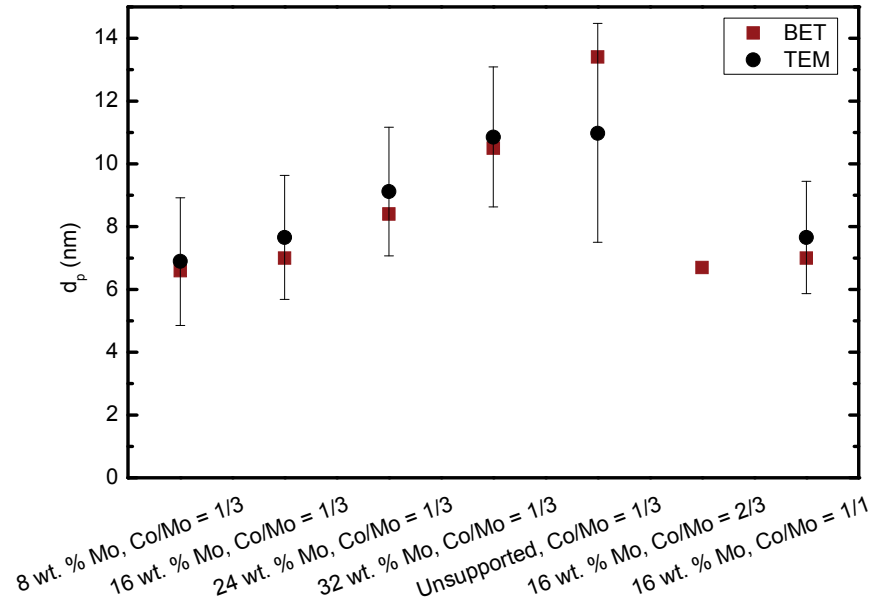

Figure 3.5: Average particle diameters as determined by BET and TEM. BET diameters assume spherical particles ($d_p = 6/[\rho \cdot SSA]$) and the densities are estimated from the composition and densities of the bulk oxides. The TEM particle size is the number average diameter after counting 150 to 250 particles. TEM error bars are one standard deviation (68 %) on the lognormal particle size distribution.

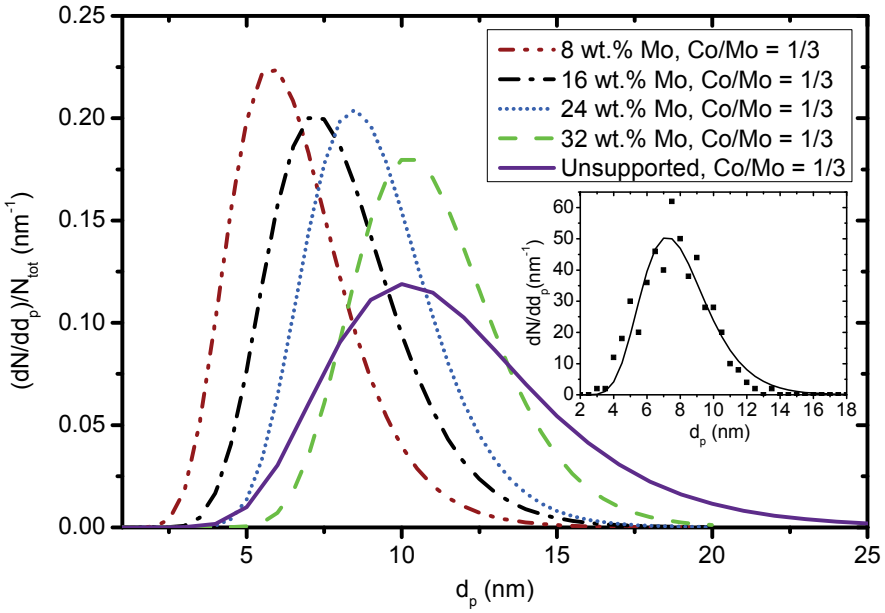

Figure 3.6: Particle size distributions of the oxide catalysts estimated from TEM images. Lognormal distributions normalized to unit area. The insert shows the counts and fit for the 16 wt.% Mo, Co/Mo = 1/3 sample.

Figure 3.7 shows TEM images of the sulfided catalysts after the catalytic tests. The formation of the layered MoS_2 structures is clearly seen by the intense black (non-straight) lines in the TEM images. The MoS_2 particles may contain one or more layers. The TEM images only reveal MoS_2 particles whose layers are oriented parallel (plus/minus a few degrees) to the electron beam; for this reason the observed size of the particles is referred to as their length. On the 8 wt.% Mo sample mostly single-layer MoS_2 structures were observed. With increasing Mo content more and more multi-layer structures are observed. Figure 3.8 summarizes the average particle length and the average number of layers per MoS_2 particle as determined by counting on the TEM images. The particle length on the supported samples increases slightly with increasing Mo content, but lies between 3 to 4 nm, which is normal for supported samples [51]. The unsupported sample contains significantly longer particles with an average length of 8.5 nm. The number of layers per MoS_2 particle increases with increasing Mo content in the sample. At 8 and 16 wt.% Mo most of the particles have only one layer, with up to three being observed. At 24 wt.% Mo the average is approximately two layers, with up to 4 layers being observed, at 32 wt.% Mo the average is approximately 2.5 layers, with up to 6 being observed and for the unsupported sample the average is 3.4 layers, with up to six layers being observed.

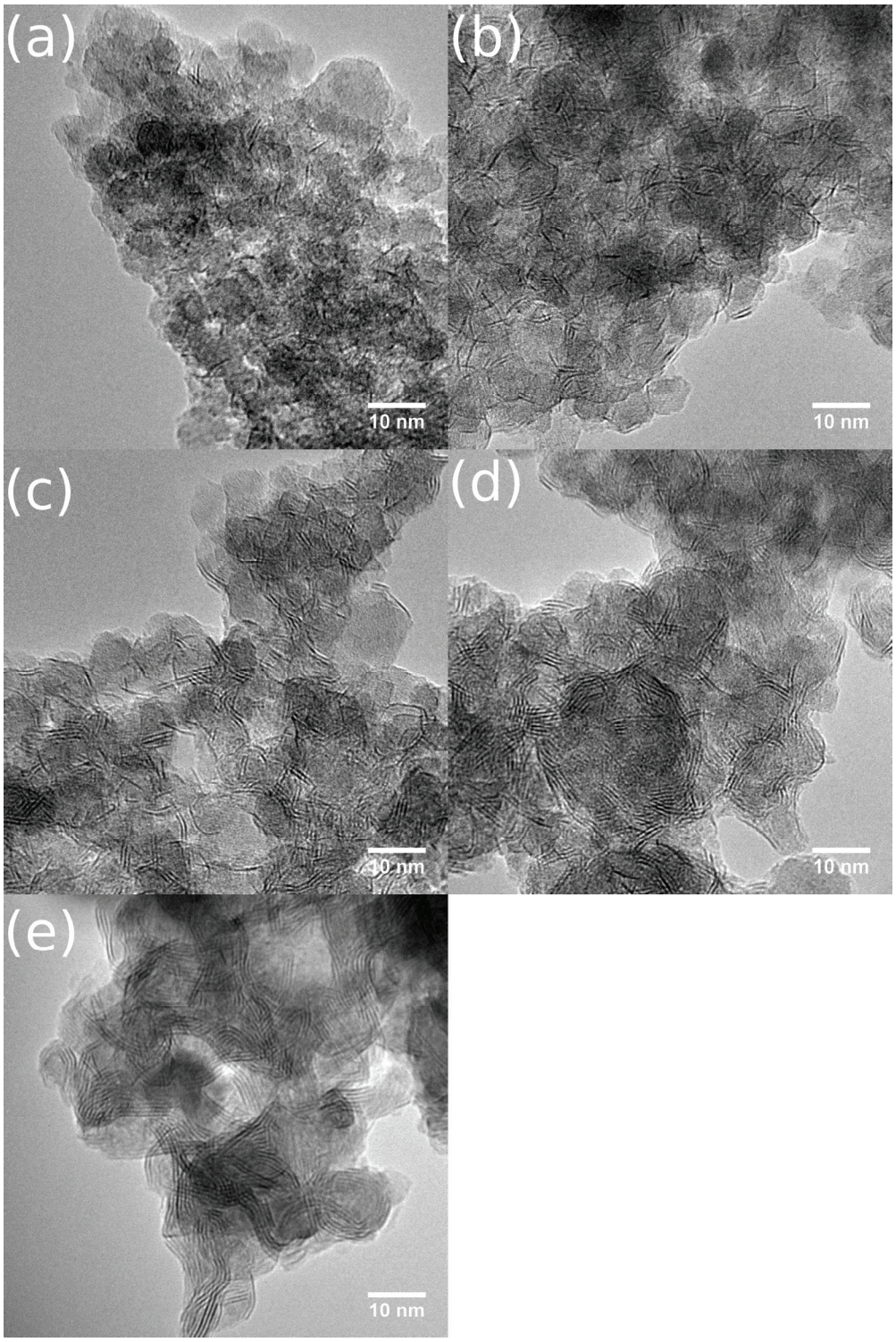

Figure 3.7: TEM images of the spent sulfide catalyst. (a) 8 wt.% Mo, Co/Mo = 1/3, (b) 16 wt.% Mo, Co/Mo = 1/3, (c) 24 wt.% Mo, Co/Mo = 1/3, (d) 32 wt.% Mo, Co/Mo = 1/3 and (e) Unsupported, Co/Mo = 1/3.

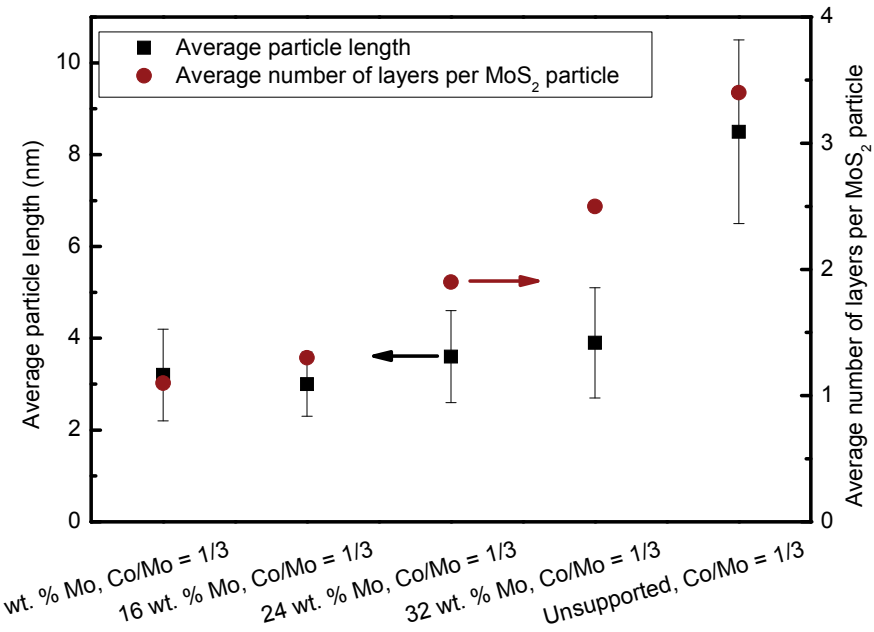

Figure 3.8: Average particle length with one standard deviation assuming log-normal distribution error bars and the average number of layers per MoS_2 particle counting on TEM images of the sulfided samples after catalytic tests.

3.3.4 Catalytic activity measurements

The catalysts were simultaneously tested for HDS of dibenzothiophene, HDN of indole and HYD of naphthalene. The pseudo first order rate constants for HDS, HDN and HYD of all the catalysts are shown in Figure 3.9, along with those of a commercial alumina-supported CoMo catalyst. The optimum for HDS was found to be 16 wt.% Mo with Co/Mo = 1/3. The observed activity is similar to what was observed for a 8 wt.% Mo sample with Co promotion prepared by impregnation on carbon support [56]. The activity is significantly higher than for unpromoted MoS_2 supported on alumina and carbon [56,106], showing that the oxide precursor prepared by one-step flame synthesis forms the cobalt-promoted active phase upon sulfidation. However, increasing the Co content to Co/Mo = 2/3 lowered the activity slightly and further increasing the Co content to Co/Mo = 1/1 reduced the activity even further. From BET measurements it was concluded that increasing the cobalt content caused a significant drop in specific surface

area. The surface area of the spent Co/Mo = 1/1 sample is only 37 % of the surface area of the oxide precursor. For the Co/Mo = 2/3 and 1/3 samples this ratio is 44 % and 59 % respectively. This could qualitatively explain the lower activity. As observed with UV-vis and XRD, addition of more cobalt resulted in the formation of significant amounts of $CoAl_2O_4$. Thus, the extra cobalt is associated with inactive components prone to sintering, rather than with molybdenum sulfide whose activity for HDS it could have enhanced.

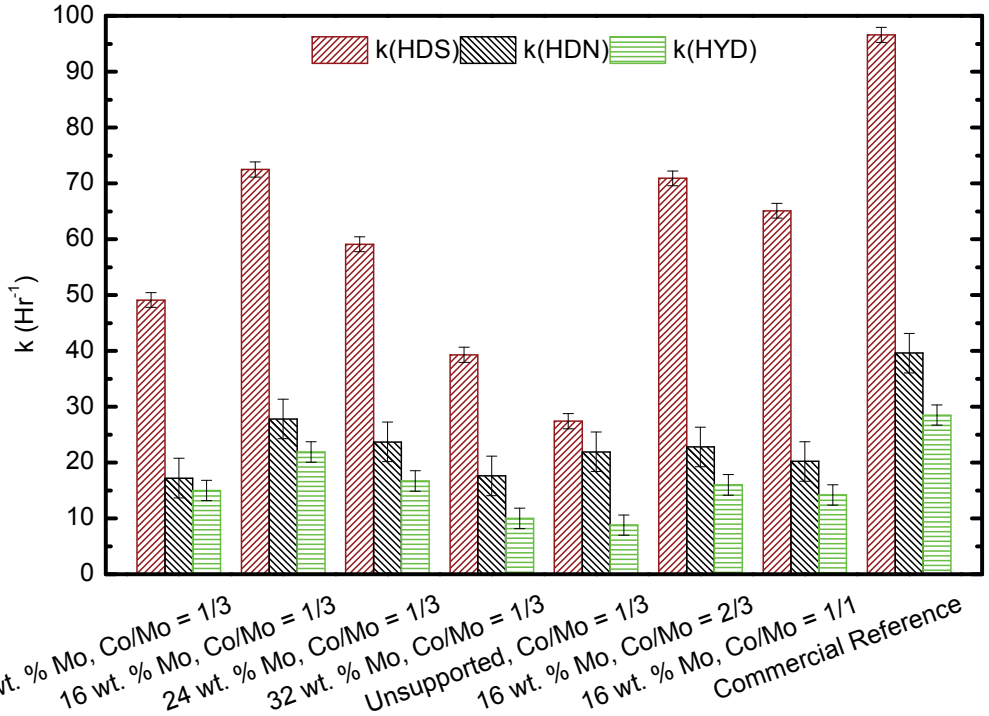

Figure 3.9: HDS, HDN and HYD pseudo first order rate constants of all the FSP catalysts and one commercial reference catalyst by monitoring the conversion of dibenzothiophene, indole and naphthalene. Error bars are one standard deviation of three measurement of the commercial reference. Liquid feed 0.5 ml/min of 3.0 wt.% dibenzothiophene, 0.5 wt.% indole, 1.0 wt.% naphthalene, 2.5 wt.% DMDS and 0.5 wt.% *n*-nonane dissolved in *n*-heptane. Temperature 350 °C and pressure p(total) = 50 atm and $p(H_2)$ = 38 atm. Hydrogen flow rate 250 Nml/min. 300 mg catalyst.

The highest surface area (221 m^2/g) and the lowest sintering (14 % loss of surface area after test) is seen for the 8 wt.% molybdenum sample, with decreasing surface area (down to 90 m^2/g) and increased sintering (up to 62 % loss of surface area) as the Mo

content increases to unsupported CoMo. The 8 wt.% molybdenum sample shows lower HDS activity than the 16 wt.% sample, probably due to the less active material, despite the lower sintering and smaller MoS_2 particles. Increasing the molybdenum content above 16 wt.% again lowers the HDS activity, possibly due to sintering or, as observed with TEM, that the high Mo samples have more layers per MoS_2 particle. The active sites are believed to be at the particle edges [53], so larger particles and more layers per particle may make edges inaccessible to the relatively large dibenzothiophene molecules [55]. In a study of noble metal promotion of MoS_2, the promoters resulting in the smallest MoS_2 particles showed the highest activity [106], in good agreement with the observation here.

The HDS activity of the best FSP prepared catalyst is approximately 75 % of that of a commercial alumina supported CoMo catalyst. This shows the potential of the FSP technique since the commercial sample is the product of many years development, while the FSP catalysts are the first examples of their kind. Further development of the FSP material could make it a serious competitor to the traditional catalyst, especially considering the preparation is one step.

The HYD activity has the same trend as the HDS activity for all samples. Also the HDN activity showed the same trend as HDS and HYD for all the supported samples. This shows that active sites for all three hydrotreating reactions are formed in the same ratio on all samples. Possibly they are the same sites. One exception is the unsupported sample which was more active in the HDN reaction than the 32 wt.% sample and the 8 wt.% Mo samples. The reason for this is not clear, but some sites favorable for coordination and reaction of indole must form on the unsupported cobalt-molybdenum sulfide.

The HDS selectivity for all the samples (including the commercial sample) is between 83 and 88 % towards biphenyl and between 12 and 17 % towards cyclohexyl benzene, making the direct desulfurization selectivity 20 to 25 percentage points higher than for a carbon supported sample [56].

These first results show that FSP is a very interesting technique for preparation of hydrotreating catalysts.

3.4 Conclusions

A series of $CoMo/Al_2O_3$ hydrotreating catalysts with different Mo and Co loadings were prepared using one-step flame spray pyrolysis. The product consisted of γ-Al_2O_3 with some $CoAl_2O_4$, while the MoO_3 was XRD amorphous, except for the highest Mo loadings. The catalysts showed high activity and high selectivity towards direct desulphurization, indicating that the desired promoted Co-Mo-S phase was formed upon sulfidation of the oxide flame synthesis product, despite formation of some $CoAl_2O_4$ during the flame synthesis. The best catalyst contained 16 wt.% Mo with atomic ratio Co/Mo = 1/3. Higher loadings (24 or 32 wt.% Mo) and a sample without alumina support had a significantly lower HDS activity. This is attributed to the sintering and increased stacking of MoS_2 layers in larger particles. The best Co/Mo ratio was 1/3, and even lower Co/Mo ratio may be beneficial, although the influence of Co loading is not as strong as the influence of Mo loading. The drop in activity with increasing Co content is attributed to the formation of $CoAl_2O_4$ during flame synthesis, which causes the catalyst to sinter at reaction conditions.

There is room for further optimization of the catalysts by extending the formulations in the concentration range 8 to 24 wt.% Mo and Co/Mo $\leq$ 1/3 and by suppressing the formation of $CoAl_2O_4$.

4. Two-nozzle FSP synthesis of $CoMo/Al_2O_3$ hydrotreating catalysts

4.1 Introduction

In order to reduce the amount of $CoAl_2O_4$ formed during the flame synthesis of $CoMo/Al_2O_3$ hydrotreating catalysts (see Section 3), two-nozzle FSP was investigated. This method has previously been shown to reduce the amount of the analogous compound $BaAl_2O_4$, by spraying Ba and Al in separate flames, during FSP synthesis of $Pt/Ba/Al_2O_3$ NO_x storage-reduction catalysts [31].

4.2 Experimental

4.2.1 Catalyst Preparation

Seven alumina-supported cobalt-molybdenum catalysts were prepared via either one- or two-nozzle FSP according to the descriptions in ref. [3] and [31], respectively. The catalysts were designed to have 16 wt.% Mo and an atomic ratio of 1/3 for Co/Mo as previously investigated (see Section 3). Precursor solutions were prepared by dissolving aluminum acetylacetonate (99%, Sigma-Aldrich), molybdenum 2-ethylhexanoate (15% Mo, Strem Chemicals), and cobalt(II)2-ethylhexanoate solution (65wt.% in mineral spirits, Sigma-Aldrich) in toluene to a total metal concentration of 0.4 mol/L, which was limited by the solubility of the aluminum compound. For one-nozzle FSP, the precursors were combined at the appropriate amounts into a single solution then heated to fully dissolve the aluminum acetylacetonate and cooled to room temperature before spraying. For two-nozzle FSP, the precursor solutions were prepared in pairs as either a Mo-Al solution and Co solution or a Al solution and Co-Mo solution, where the appro-

priate precursors were combined then heated to dissolve the aluminum acetylacetonate and cooled to room temperature before spraying.

For one-nozzle FSP, the precursor solution was fed through a capillary tube at 3 mL/min by a syringe pump and dispersed with 7 Nl/min oxygen gas at 2 bar annular nozzle pressure. The spray was ignited by the surrounding premixed methane flame (1 Nl/min CH_4 and 3 Nl/min O_2). The powder samples were collected at 52 cm from the nozzle onto water-cooled glass-fiber filters (Whatman GF6, 240 mm) supported by a vacuum pump (Bush R5 0063).

For two-nozzle FSP the precursor solutions were fed through capillary tubes at 4 mL/min by syringe pumps and dispersed with 7 Nl/min oxygen gas at 1.6 bar annular nozzle pressure. The sprays were ignited by the surrounding premixed methane flame (1.5 Nl/min CH_4 and 3.2 Nl/min O_2). The powder samples were collected at 50 cm from the nozzle onto water-cooled glass-fiber filters (Whatman GF6, 257mm) supported by a vacuum pump (Busch SV1025C). During preparation of the two-nozzle FSP samples, the setup was changed such that an angle θ from 15 to 32° was used (see Figure 4.1), resulting in mixing distances m ranging from 8.1 to 17.5 cm (see Table 4.1).

4.2.2 Catalyst charaterization

Details of specific surface area, UV-vis, XRD and TEM measurements are given in sections 3.2.2 through to 3.2.5.

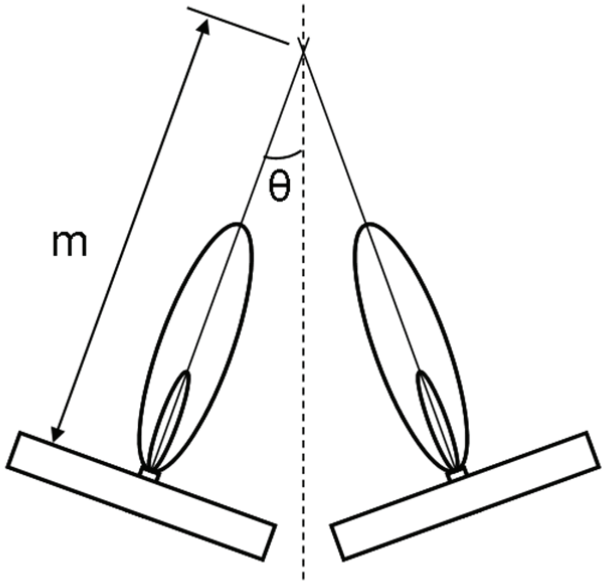

Figure 4.1: Two-nozzle FSP setup, where θ is the angle between the center and mixing lines, and m is the mixing distance from the nozzle to the mixing point.

Table 4.1: List of samples, two-nozzle preparation parameters, specific surface area (SSA) and crystalline phases observed with XRD, Raman and UV-vis of the oxide precursor and SSA of the as prepared (SSA_o) and the sulfide catalyst after catalytic activity measurements (SSA_s).

Sample	θ (°)[a]	m (cm)[a]	SSA_o (m^2/g)[b]	SSA_s (m^2/g)[c]	Ratio[d]	Oxide phases[e]
One-nozzle	-	-	202	145	0.72	γ-Al_2O_3, $CoAl_2O_4$, β-$CoMoO_4$
Mo-Al//Co@15°	15	17.5	162	130	0.80	γ-Al_2O_3, β-$CoMoO_4$
Mo-Al//Co@20°	20	12.2	198	156	0.79	γ-Al_2O_3, β-$CoMoO_4$
Mo-Al//Co@23°	23	10.1	161	129	0.80	γ-Al_2O_3, β-$CoMoO_4$
Mo-Al//Co@28°	28	10.1	148	123	0.83	γ-Al_2O_3, β-$CoMoO_4$
Mo-Al//Co@32°	32	8.1	139	121	0.87	γ-Al_2O_3, $CoAl_2O_4$, β-$CoMoO_4$
Al//Co-Mo@20°	20	12.2	193	158	0.82	γ-Al_2O_3, β-$CoMoO_4$

[a]angle between the nozzle and vertical and mixing distance of the two flames (see Figure 4.1), [b]specific surface area of the oxide catalysts, [c]specific surface area of the sulfide catalysts, [d]ratio between the specific surface areas of the sulfide and oxide catalysts, [e]crystalline phases detected by XRD, diffuse reflectance UV-vis and Raman spectroscopy.

4.2.3 Raman spectroscopy

Laser Raman spectroscopy was performed on a Horiba Jobin Yvon LabRAM HR system with an argon ion laser tuned to the green 514.5 nm line using an oscillating crystal. The as-prepared oxide samples were pressed and sieved to 150-300 μm particles and loaded in a modified in-situ cell (Linkham). The samples were dehydrated in a flow of dry air at 550 °C for 15 minutes and then cooled to room temperature before measuring the Raman spectrum from 100 to 1100 cm^{-1} using a monochromator with 1800 gratings pr. mm. The integration time was 120 s and the average of ten scans was used.

4.2.4 Catalytic activity measurements

Details of the catalytic activity measurements can be found in Section 3.2.6.

4.3 Results and discussion

4.3.1 Catalyst preparation and specific surface area

Alumina supported cobalt-molybdenum hydrotreating catalysts were prepared with two-nozzle FSP at different angle and mixing distances (see Figure 4.1 and Table 4.1). The aim was to reduce the amount of $CoAl_2O_4$ in the product compared to one-nozzle FSP (see Section 3), since cobalt in this spinel phase is not available for promoting the catalytically active MoS_2 phase formed during catalyst activation.

The products of both one- and two-nozzle FSP were powders with very low density due to high inter particle porosity compared to wet synthesis of alumina nanoparticles. The powders prepared by two-nozzle FSP appeared grey, except for the Mo-Al//Co@32° sample which appeared light blue. The one-nozzle product also appeared blue.

The specific surface area ranged from 139 to 202 m^2/g. Assuming spherical particles this is equivalent to average particle diameters from 7 to 10 nm. Note that the BET sur-

face area of the two-nozzle oxide catalysts decreases with decreasing mixing distance (see Table 4.1). This may indicate increased residence time and therefore a longer time for particle growth in the case of shorter mixing distance.

4.3.2 X-ray diffraction

X-ray diffraction measured on the as-prepared oxide catalysts only showed γ-Al_2O_3 for the Mo-Al//Co samples, but for the Al//Co-Mo@20° sample a broad reflection at 2θ = 27° was also observed (see Figure 4.2). This could be assigned to β-$CoMoO_4$ [107-108], in agreement with previous FSP synthesis of mixed CoMo-oxide without alumina (see Section 3.3.2). There were no signs of crystalline MoO_3, but the diffraction pattern of crystalline $CoAl_2O_4$ nanoparticles is similar to that of γ-Al_2O_3, hence, small amounts of $CoAl_2O_4$ cannot be excluded by XRD (see Section 3.3.2).

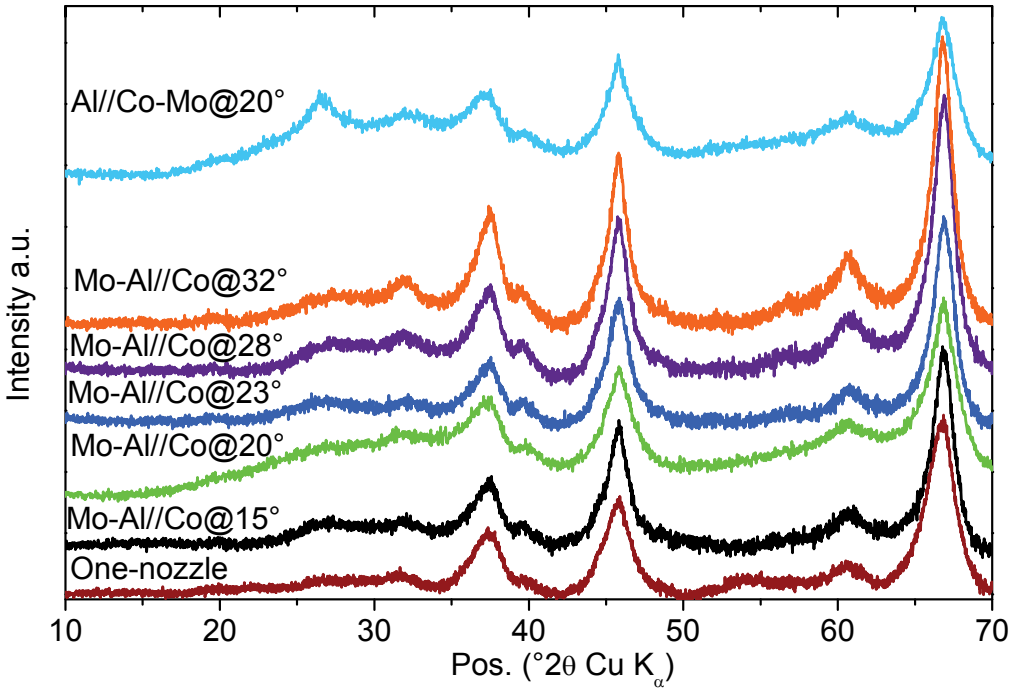

Figure 4.2: X-ray diffraction. γ-A2O3 is the only crystalline phase detected after both one- and two-nozzle synthesis of Co-AlMo. The reflection at 2θ = 27° for the CoMo-Al sample was also observed when synthesizing CoMo-oxide without alumina using one-nozzle FSP and is assigned to β-$CoMoO_4$.

4.3.3 Diffuse reflectance UV-vis spectroscopy

Since the *d–d* transitions of tetrahedrally coordinated Co^{2+} of $CoAl_2O_4$ are symmetry allowed, they are relatively intense and three peaks at 548, 583 and 630 nm, corresponding to the expected spin-allowed transitions, can easily be observed by diffuse reflectance UV-vis spectroscopy (see Section 3.3.1).

Diffuse reflectance UV-vis spectra were recorded on the as-prepared oxide catalysts. Comparing the visible region of the spectrum, only the Mo-Al//Co@32° sample clearly showed the three peaks associated with $CoAl_2O_4$, while only very weak traces could be observed for the other two-nozzle samples (see Figure 4.3). This is consistent with the Mo-Al//Co@32° sample appearing blue and the other samples appearing gray-black. Comparing to the one-nozzle FSP product, the amount of $CoAl_2O_4$ is significantly reduced.

When the mixing distance of the two flames is reduced, it is expected that two-nozzle FSP will be similar to one-nozzle FSP, consistent with the UV-vis spectrum of the Mo-Al//Co@32° sample exhibiting the closest resemblance to the spectrum of the one-nozzle product.

The other two-nozzle samples exhibit broad transitions in the whole visible region of the spectrum, with no distinct features that allows their assignment, except that they belong to other cobalt species like $CoMoO_4$ or cobalt oxide. The particular strong absorption by the Mo-Al//Co@20° sample in the 650 to 750 nm range is likely due to cobalt oxide. When preparing only alumina supported molybdenum oxide by FSP light blue samples are obtained, with only weak absorption in the red and near infra red part of the spectrum, which is assigned to partly reduced molybdenum like Mo^{5+} (see Section 8.3.4).

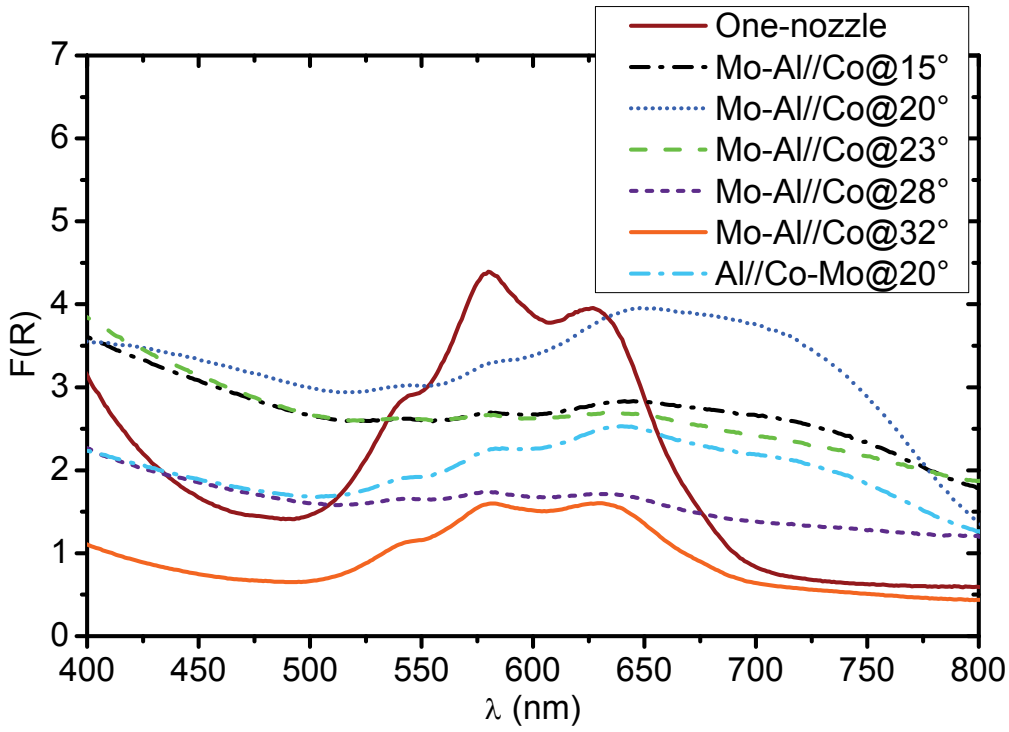

Figure 4.3: Diffuse reflectance spectroscopy in the visible region. The three T_d Co^{2+} *d–d* bands due to $CoAl_2O_4$ (530 to 650 nm) are very weak when using two-nozzle synthesis showing that this phase was successfully diminished. When decreasing the mixing distance of the flames the product is more like the one-nozzle product. Absorption between 650 and 750 is due to other cobalt species like β-$CoMoO_4$ or cobalt oxides.

4.3.4 Raman spectroscopy

The oxide catalysts were investigated with Raman spectroscopy after dehydration at 550 °C in a flow of dry air. The spectra showed that a mixture of supported molybdenum oxide, crystalline β-$CoMoO_4$ and possibly crystalline MoO_3 was present on the surface of the catalysts (see Figure 4.4). β-$CoMoO_4$ is observed from the peaks at 818, 880, 937 and 947 cm^{-1} [109-110] and possibly also crystalline MoO_3 is the origin of the 818 cm^{-1} peak (see Section 8.3.3). Despite β-$CoMoO_4$ is a meta-stable phase (α-$CoMoO_4$ is the thermodynamically stable one [109]) it can be stabilized by the alumina support [111]. Supported MoO_x species are observed for all samples by the shoulder around 1004 cm^{-1} (symmetric Mo=O molybdenyl stretching mode [112]) and the broad peak from 800 to 900 cm^{-1} (Mo-O-Mo asymmetric stretching mode or Mo-O-Al stretching modes), by

comparison with the Raman spectrum of an alumina supported molybdenum oxide sample prepared by one-nozzle FSP (also shown in Figure 4.4, see Section 8.3.3 too) and the Raman spectra of supported molybdenum oxide prepared by one-nozzle FSP and impregnation reported in the literature [69,113].

The β-$CoMoO_4$ phase was only observed by XRD for the Al//Co-Mo@20° sample, where molybdenum and cobalt are prepared in the same flame. The Raman band for the supported MoO_x species is also relatively weak, compared to the β-$CoMoO_4$ bands for this sample.

The intensity of the β-$CoMoO_4$ Raman bands for the Mo-Al//Co@32° sample might indicate that this phase should also appear in XRD; however Raman intensities are also reduced when the excitation light is absorbed. By diffuse reflectance UV-vis it was observed that at 515 nm the absorption is low for the Mo-Al//Co@32° sample, leading to higher intensity in the Raman spectra.

The Raman spectra of alumina supported cobalt- and molybdenum oxide catalysts prepared by impregnation with ammonium heptamolybdate and calcined at 450 to 500 °C typically resemble the Raman spectrum of the heptamolybdate complex [41,47,114]. This may evolve into β-$CoMoO_4$ with increasing calcination temperature [111]. These Raman spectra are recorded in the hydrated state, which is very different from the dehydrated state [112]. In this study only an intense fluorescence background was observed in the as-prepared hydrated state, possibly due to carbonaceous residues from the FSP synthesis, making dehydration and oxidation necessary. The observation of a mixture of supported MoO_x species and β-$CoMoO_4$ after the thermal treatment show that the structure of the oxide catalysts prepared by FSP is similar to the structure of impregnated and calcined catalysts.

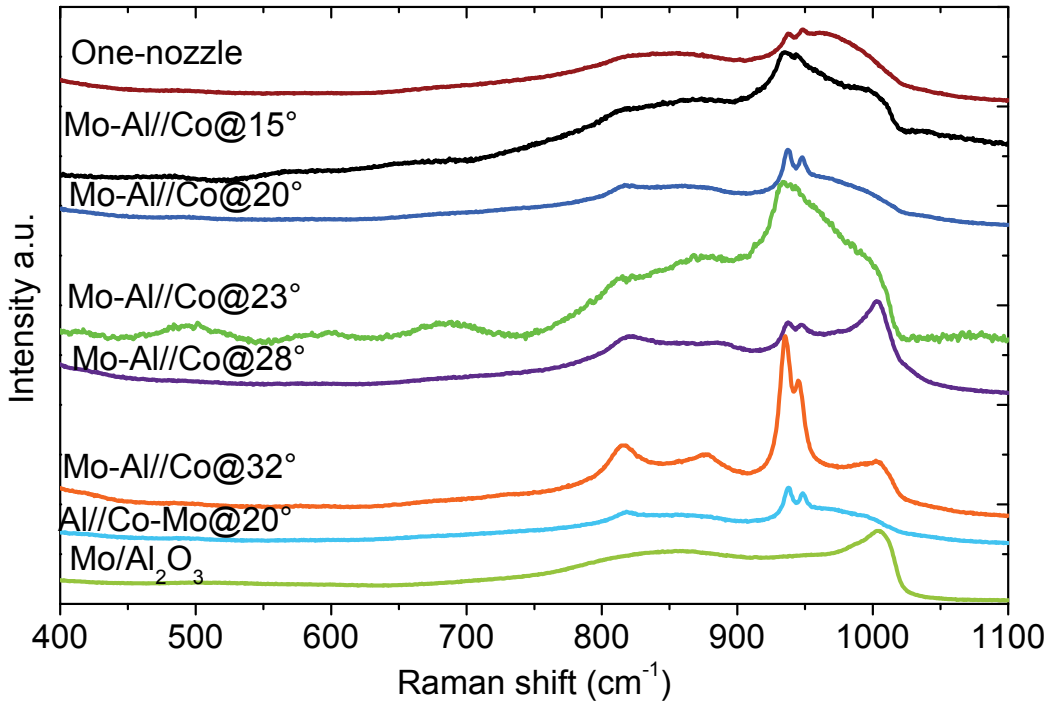

Figure 4.4: Raman spectra measured at room temperature after dehydration at 550 °C in dry air. The two peaks at 937 and 947 cm^{-1} indicates β-$CoMoO_4$, a meta-stable phase stabilized by the alumina support. The shoulder at 1004 cm^{-1} indicates supported MoO_x species by comparison to Mo/Al_2O_3 prepared by one-nozzle FSP (scaled to 1/4 intensity). The peaks at 818 and 880 cm^{-1} are also expected for β-$CoMoO_4$ or the 818 cm^{-1} peak could indicate crystalline MoO_3.

4.3.5 Electron microscopy

The catalysts were investigated by transmission electron microscopy (TEM), both the as-prepared oxide catalysts and the sulfide catalysts after pressing, sieving, sulfiding and performing catalytic activity measurements. The oxide catalysts showed loosely packed nanoparticles with diameters between approximately 5 and 15 nm (see Figure 4.5). Measuring at least 250 particles from different TEM images of the same samples resulted in number average particle diameters from 8 to 11 nm, which is in good agreement with the spherical equivalent particle diameters calculated from the BET surface areas (see Figure 4.6).

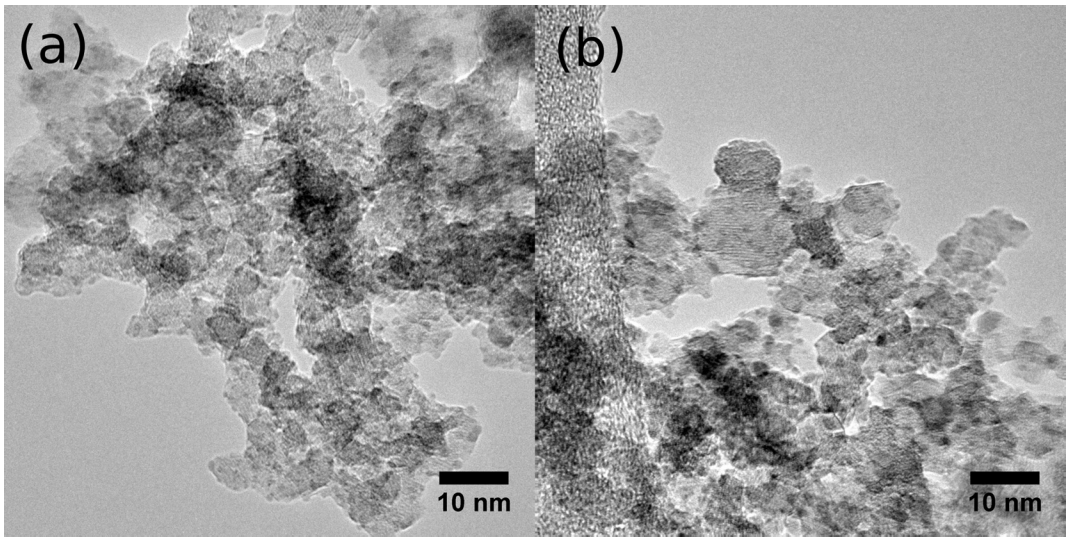

Figure 4.5: Transmission electron microscopy images of two of the oxide catalysts. Dark spots around 2 nm may be β-$CoMoO_4$ (a) Mo-Al//Co@20° (b) Al//Co-Mo@20°

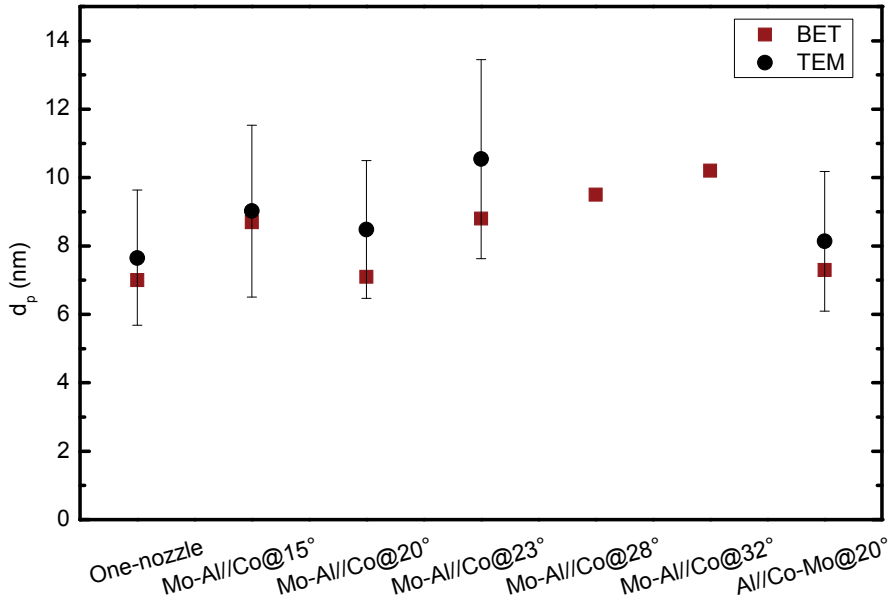

Figure 4.6: Spherical equivalent particle size from BET surface area and number average particle size with one standard deviation error bars measured from more than 200 particles on TEM images.

On some of the images darker spots of around 2 nm in diameter were observed on top of the alumina particles of approximately 10 nm diameter, indicating molybdenum containing domains of e.g. β-$CoMoO_4$, however no larger particles of MoO_3 or $CoMoO_4$ were observed, in agreement with the XRD and Raman results.

After sulfidation the nanoparticles have been compacted and the agglomerates seem much denser. Molybdenum sulfide is observed as dark lines on the surface of the alumina nanoparticles (see Figure 4.7, cf. Refs. [59-60]). Each line is one layer of molybdenum atoms sandwiched between two layers of sulfur atoms viewed edge on. Multiple parallel lines show that larger particles of MoS_2 are formed. The average particle lengths was around 3 nm and the average number of layers per particle was around 1.5 for the two-nozzle FSP catalysts, which is similar to the catalyst prepared by one-nozzle FSP (see Section 3.3.3). A study of supported MoS_2 catalysts with different noble metal promoter atoms showed that those promoters leading to short, single layer MoS_2 particles around 2 nm and 1.1 to 1.3 layers per particle had the highest catalytic activity [106]. This shows that there is room for optimizing the MoS_2 particle size of the FSP prepared catalysts.

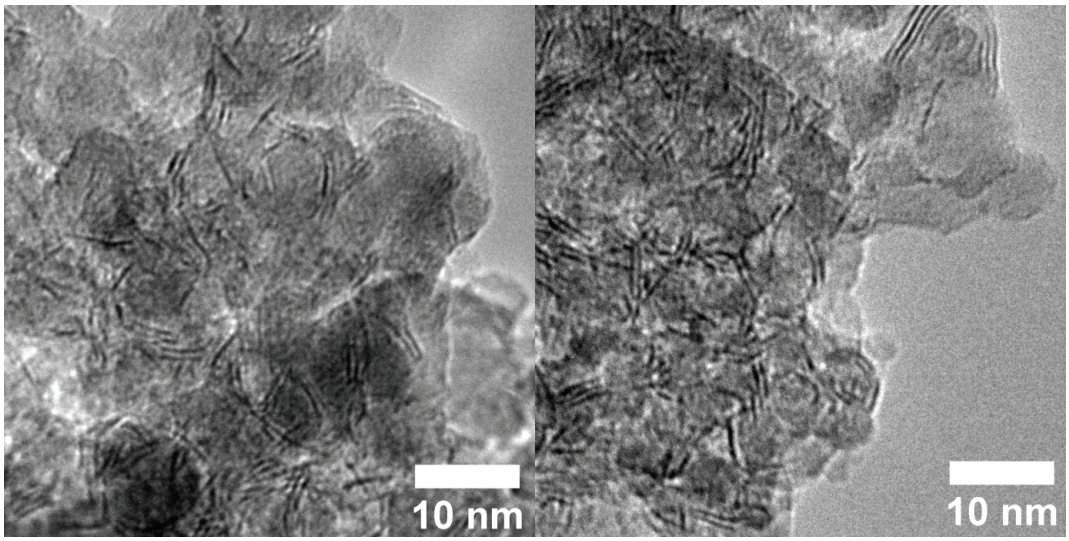

Figure 4.7: Transmission electron microscopy images of two of the sulfide catalysts after catalytic activity measurements showing that MoS_2 was formed. (a) Mo-Al//Co@20° (b) Al//Co-Mo@20°

4.3.6 Catalytic activity measurements

After sulfidation the activity of the catalyst was measured for the three hydrotreating reactions HDS, HDN and HYD. Catalytic activity is reported as first order rate constants for the conversion of dibenzothiophene, indole and naphthalene respectively at 350 °C and 50 atm, relative to the activity of a commercial reference (see Figure 4.8 and Section 3.3.4). Comparing the HDS activity for the two flame products there is a trend of increasing activity with decreasing mixing distance. The Mo-Al//Co@15° sample, which was prepared with the longest mixing distance, had approximately 73 % of the activity of the commercial reference, which is lower than the activity of the one-nozzle sample at 75 %. The Mo-Al//Co@20° sample is more active than the one-nozzle sample at 81 %. The Mo-Al//Co@23° and Mo-Al//Co@28°, which were prepared with the same mixing distance but different angles, have similar HDS activity at 84 and 83 % respectively. The most active catalyst in the two-nozzle series is the Mo-Al//Co@32° sample at 91 %. The Al//Co-Mo@20° sample had 77 % activity, which is lower than the

similar Mo-Al//Co@20° sample, showing that molybdenum and aluminum should preferably be sprayed in the same flame.

This shows that by two- instead of one-nozzle FSP the catalytic activity for HDS could be increased from 75 to 91 % of the commercial reference. The best catalyst contained significantly lower, but measureable, amounts of $CoAl_2O_4$ compared to the one-nozzle sample according to UV-vis. Both supported MoO_x species and β-$CoMoO_4$ were clearly observed by Raman spectroscopy. This shows that separating cobalt and molybdenum in each flame did indeed result in better promotion of the catalytically active MoS_2 phase after sulfidation. However, also the residence time in the flame and therefore the better growth of β-$CoMoO_4$ may have a positive influence.

The trends in HDN and HYD activities are less pronounced than for HDS, but for all two-nozzle samples there is a significant improvement. Comparing the one-nozzle FSP catalyst to the best two-nozzle catalyst the HDN activity increased from 70 to 90 % and the HYD activity increased from 77 to 95 % of the commercial reference. Like for HDS the highest HDN activity is desirable, but high HYD activity my result in high consumption of hydrogen without improving the quality of the fuel product.

All the catalysts had lower surface area after catalytic tests, but the ratio between the surface area of the sulfide and oxide catalysts was between 0.8 and 0.9 for all two-nozzle samples (see Table 4.1).

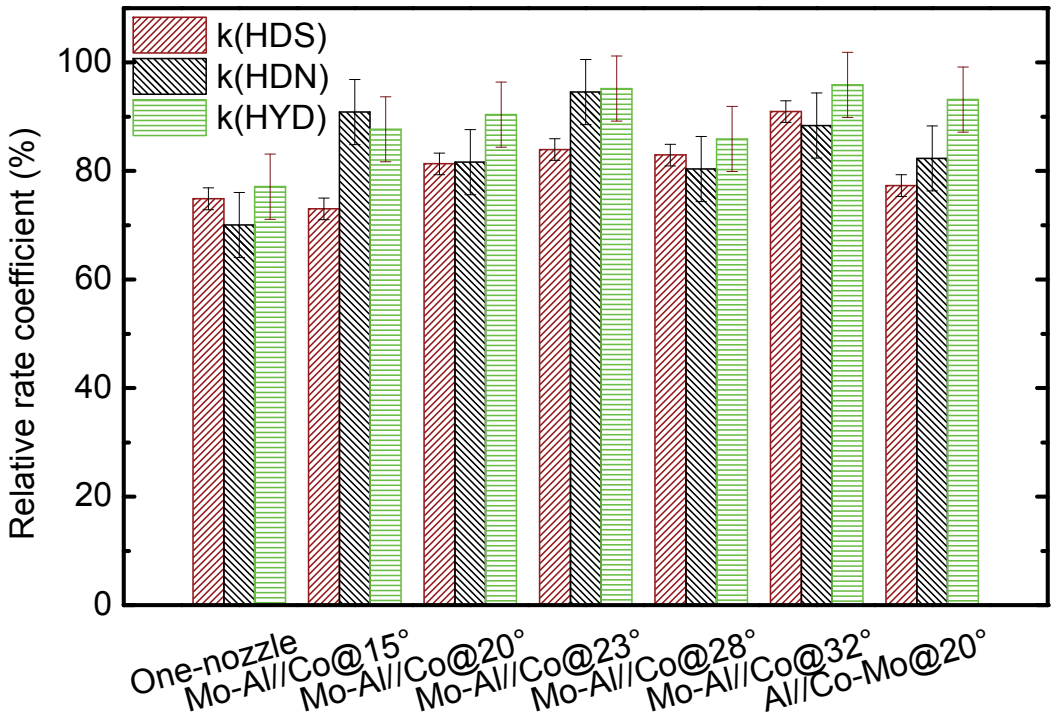

Figure 4.8: Catalytic activity in terms of first order rate constants for the conversion of dibenzothiophene (HDS), indole (HDN) and naphthalene (HYD) relative to a commercial reference. A significant improvement is obtained by two-nozzle synthesis, particular with cobalt in one flame and aluminum and molybdenum in the other at short mixing distance.

4.4 Conclusions

Highly active alumina supported cobalt-molybdenum hydrotreating catalysts have been prepared by two-nozzle FSP. The only crystalline phase detected by XRD was γ-Al_2O_3. The $CoAl_2O_4$ phase produced by one-nozzle FSP, as determined from diffuse reflectance UV-vis spectroscopy, was successfully diminished by two-nozzle FSP, but was detected at short mixing distances between the two flames. Other species observed by Raman spectroscopy were β-$CoMoO_4$ and supported MoO_x species. β-$CoMoO_4$ appeared when Co and Mo were sprayed together and at short mixing distances when the cobalt precursor was sprayed independently from the molybdenum and alumina precursors. This may derive from the longer residence time until quenching. The catalytic ac-

tivity after sulfidation for HDS increased from about 75 to 91 % of the activity of a commercial reference from for the best two-nozzle catalyst compared to the one-nozzle catalyst. Also the HDN activity improved from 70 to about 90 % of the commercial reference. TEM images of the used catalysts showed that the catalytically active MoS_2 phase was formed during the sulfidation step with relatively small particles of approximately 3 nm in length and on average 2 layers per particle, which could still be improved. All catalysts lost surface area during the activation and activity measurements, with all the two-nozzle catalysts retaining 80 to 90 % of the surface area.

5. One-nozzle FSP synthesis of $CoMo/Al_2O_3$-SiO_2 hydrotreating catalysts

5.1 Introduction

The $CoAl_2O_4$ is an undesired phase formed during the one-nozzle synthesis of $CoMo/Al_2O_3$ catalysts (see Section 3), since this cobalt is unavailable for promotion of the catalytically active MoS_2 phase. Besides two-nozzle synthesis of $CoMo/Al_2O_3$, where cobalt and aluminum were separated in different flames (see Section 4), changing the support material from pure Al_2O_3 to Al_2O_3-SiO_2 mixtures may also reduce the amount of $CoAl_2O_4$ formed. Alumina is generally found to be a better support material than silica for hydrotreating catalysts [115-116], but mixtures of alumina and silica have been employed with good results [105,117-118].

This section describes the FSP synthesis, structural characterization and catalytic evaluation of $CoMo/Al_2O_3$-SiO_2 catalysts.

5.2 Experimental

Five catalysts were synthesized by dissolving molybdenum 2-ethylhexanoate, cobalt 2-ethylhexanoate, aluminum acetylacetonate and hexamethyl disiloxane in toluene to a total metal concentration of 0.4 M. The catalysts were prepared with 16 wt.% Mo and Co/Mo = 1/3 atomic ratio (the best transition metal loading obtained in the initial study, see Section 3) and Si/Al ratios of 5/95, 15/85, 25/75, 50/50 and 100/0. The precursors were sprayed at 3 ml/min using 7 Nl/min of O_2 dispersion gas. See Section 2 for details on FSP experimental.

The catalysts were characterized by nitrogen adsorption (BET), UV-vis and XRD and evaluated as catalysts for the three hydrotreating reactions HDS, HDN and HYD (see

Sections 3.2.2 through to 3.2.6 for details on characterization and catalytic activity measurements).

5.3 Results and discussion

The products of the FSP synthesis of the silica-alumina supported CoMo-oxide catalysts were light blue, low density powders, while the pure silica supported samples appeared light pink and had very low density. The specific surface areas of the as-prepared oxide catalysts and the spent sulfide catalysts (after pressing, sieving, activation by sulfidation and catalytic activity measurements) are summarized in Table 5.1. There was a trend of increasing surface area with increasing silica content, from 202 m^2/g for the pure alumina supported sample, between 218 and 261 m^2/g for the mixed silica-alumina supported samples to 369 m^2/g for the pure silica supported sample. The same trend was observed for the spent catalysts.

Table 5.1: Specific surface areas of the fresh oxide and spent sulfide catalysts, ratio between the spent and initial surface areas and the phases detected by XRD and UV-vis spectroscopy.

Si/Al	SSA_o[a] (m^2/g)	SSA_s[b] (m^2/g)	SSA ratio[c]	Phases[d]
0/100	202	145	0.72	γ-Al_2O_3, $CoAl_2O_4$
5/95	226	168	0.74	γ-Al_2O_3, $CoAl_2O_4$
15/85	218	170	0.78	Amorphous
25/75	230	175	0.76	Amorphous
50/50	261	185	0.71	Amorphous
100/0	369	309	0.84	Amorphous

[a]SSA of the as-prepared oxide catalysts, [b]SSA of the spent sulfide catalyst, [c]ratio between the surface areas of the as-prepared and the spent catalysts, [d]phases detected with XRD and UV-vis.

5.3.1 X-ray diffraction

X-ray diffractograms of the as-prepared oxide catalysts were measured in order to investigate the interaction between silica and alumina. At low Si/Al ratios the only crystalline phase detected was γ-Al_2O_3 (see Figure 5.1), with the possibility of the reflections of $CoAl_2O_4$ overlapping and thus not being detected (see Section 3.3.2). At Si/Al =

15/85 and upwards, the materials became amorphous and only the very wide bump of amorphous silica between 2θ = 20 and 30° was observed. No signs of crystalline MoO_3 or cobalt oxides were observed. This indicated strong interaction between silica and alumina after FSP synthesis, forming amorphous silica-alumina mixtures instead of separate silica and alumina nanoparticles. FSP made amorphous silica-alumina mixtures have been shown to be highly acidic and were used as support for noble metal hydrogenation catalysts [119-120].

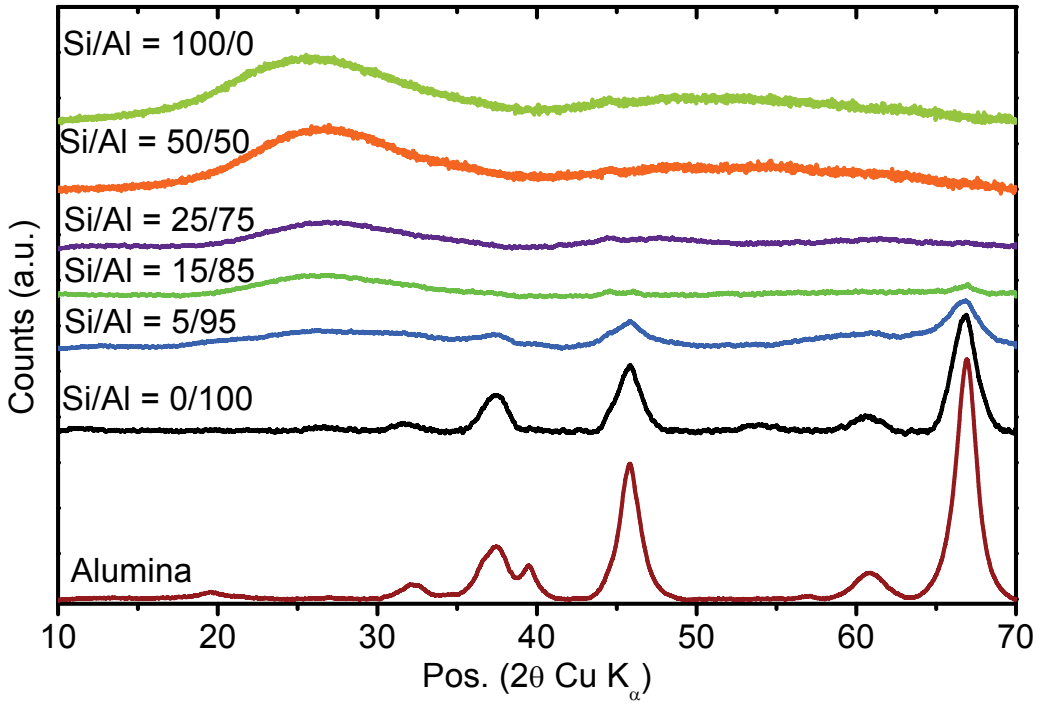

Figure 5.1: X-ray diffractograms of the as-prepared oxide catalysts, showing that the materials become amorphous at Si/Al ratios larger than 15/85.

5.3.2 UV-vis spectroscopy

UV-vis diffuse reflectance spectra recorded of the as-prepared oxide catalysts showed that the amount of $CoAl_2O_4$ was significantly reduced when using silica-alumina mixtures as support material (see Figure 5.2). At Si/Al = 5/95 the intensity of the 548, 583

and 630 nm bands, representative of tetrahedrally coordinated Co^{2+} in $CoAl_2O_4$, were reduced compared to the pure alumina supported sample. At ratios 15/85, 25/75 and 50/50 the intensity of those bands were significantly reduced, a new band around 505 nm appeared and the background absorption above 700 nm increased, indicating that other cobalt species are formed. For the pure silica supported sample the UV-vis absorption spectrum was completely different, in line with the sample appearing pink.

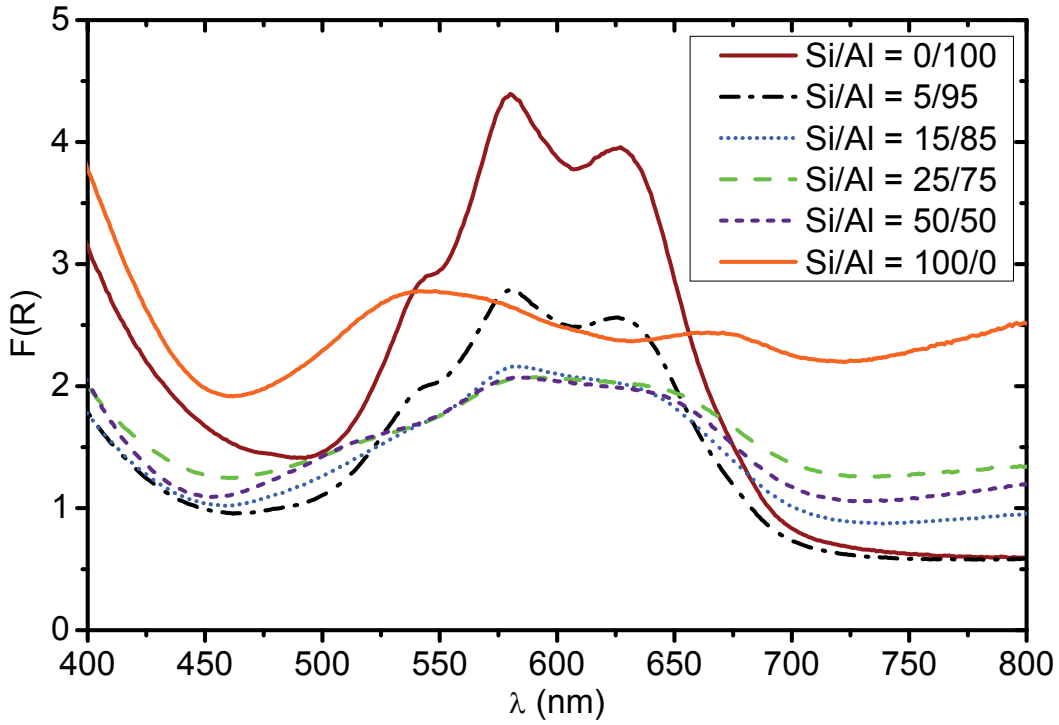

Figure 5.2: Diffuse reflectance UV-vis spectra of the as-prepared oxide catalyst in the visible region of the spectrum. The three bands observed at 548, 583 and 630 nm are expected for T_d Co^{2+} in $CoAl_2O_4$.

5.3.3 Catalytic activity

The catalytic activity of the silica-alumina supported catalysts was measured for the three hydrotreating reactions hydrodesulfurization (HDS), hydrodenitrogenation (HDN) and hydrogenation (HYD). The activities are reported as first order reaction rate con-

stants relative to a commercial sample, which was measured both before and after the FSP series (see Figure 5.3 and Section 3.3.4 for comparison). The HDS activity of the silica-alumina supported samples was approximately the same as the activity of the pure alumina supported sample. However; the purely silica supported sample showed significantly lower HDS activity than the other samples, despite the significantly higher surface area. This is in line with previous observations that silica is not as good a support material for molybdenum sulfide based hydrotreating catalysts as alumina [115-116]. Despite significantly reducing the amount of $CoAl_2O_4$, no significant improvement in HDS activity was achieved, which may relate to unfavorable support interactions. The hydrotreating selectivity was similar to the pure alumina supported sample, with approximately 85 % selectivity towards direct desulphurization, with biphenyl as the product, and approximately 15 % selectivity towards pre-hydrogenation, with cyclohexyl benzene as the product.

For the HDN activity there is significant improvement at Si/Al ratios 5/95 and 15/85, where the FSP made catalyst is better than the commercial reference. The HDN activity then declines significantly at Si/Al ratios 25/75, 50/50 and 100/0, to values below the activity of the pure alumina supported sample. The reason for the HDN activity improvement is not clear, however at these Si/Al ratios FSP made amorphous silica-alumina have shown to contain high concentration of acidic sites [119]. This might help the HDN activity, despite the model nitrogen heterocyclic compound used (indole) is not a basic molecule, but following an initial hydrogenation step the higher acidity may facilitate HDN.

The HYD activity for hydrogenation of naphthalene also increased at Si/Al = 5/95, but decreased to values below the pure alumina supported sample at higher ratios, however this is within the experimental uncertainty.

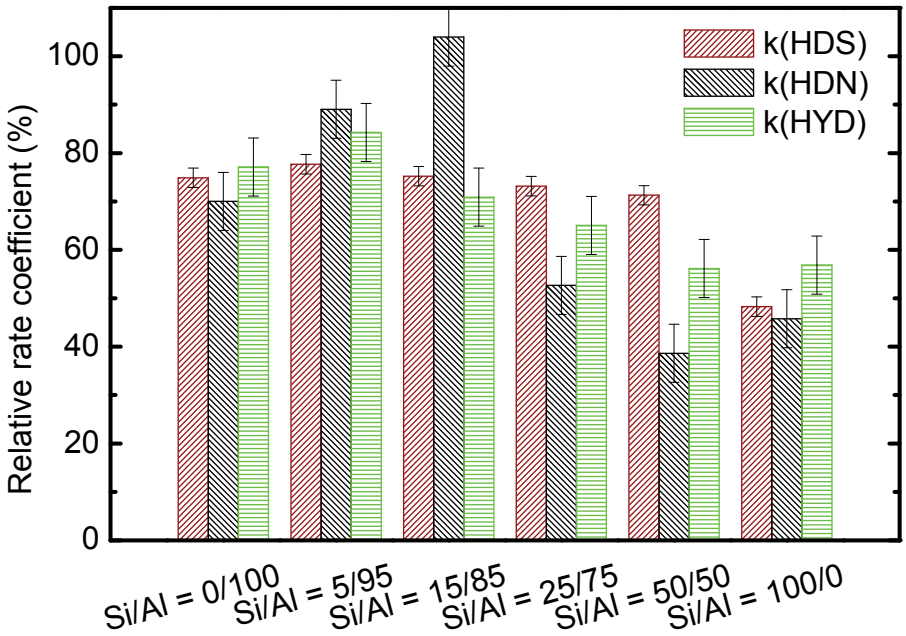

Figure 5.3: Catalytic activity of the silica-alumina supported CoMo catalysts reported as first order rate coefficients relative to the commercial reference (see Section 3.3.4)

5.4 Conclusions

Formation of $CoAl_2O_4$ during one-nozzle FSP synthesis of supported CoMo catalysts was successfully diminished by employing silica-alumina mixtures as support, instead of pure alumina, as determined with UV-vis diffuse reflectance spectroscopy. The resulting materials were mostly amorphous, showing good interaction between the silica and alumina after FSP synthesis and not just separate silica and alumina nanoparticles. The specific surface area of the catalysts increased with increasing silica content. The HDS catalytic activity remained the same for silica-alumina mixtures as for pure alumina support, so increased surface area and decreased $CoAl_2O_4$ content did not improve

the HDS activity. For pure silica support the HDS activity decreased, as is normally observed for molybdenum sulfide based hydrotreating catalysts. The HDN activity improved significantly at low Si/Al ratios, but decreased again at high ratios. A similar trend was observed for the HYD activity.

6. Structure of alumina supported vanadia catalysts for oxidative dehydrogenation of propane prepared by flame spray pyrolysis

6.1 Introduction

The ability of FSP to prepare thermally stable and high surface area oxides, which can be used as catalysts directly after synthesis, makes it interesting for oxidative dehydrogenation of propane, where oxide catalysts are typically employed. A series of vanadia on alumina catalysts were prepared, characterized and evaluated as catalysts for the ODP reaction.

6.2 Experimental

6.2.1 Catalyst preparation

Aluminium(III)acetylacetonate and vanadium(III)acetylacetonate (used as received from Sigma Aldrich) were dissolved in anhydrous toluene to a total metal concentration of 0.4 M in ratios for preparation of 2, 3, 5, 7.5 and 10 wt.% V on alumina assuming the products are V_2O_5 and Al_2O_3 (see Table 6.1). After stirring and gentle heating to about 50 °C clear green-brown solutions were obtained. The precursor solutions were sprayed at 5 ml/min with 5 Nl/min O_2 as dispersion gas at 1.8 bar pressure drop. Details of FSP experimental are found in Section 2.

6.2.2 Catalyst characterization

The specific surface area (SSA) was measured on the as-prepared FSP powder, after degassing at 170 °C in a flow of dry nitrogen, by nitrogen adsorption at its boiling point (Quantachrome iQ_2) using multipoint BET theory with six points in the p/p_0 = 0.05 to 0.25 range. The BET average particle diameter assuming spherical particles was calcu-

lated as $d_p = 6/(SSA \cdot \rho)$, where ρ is the Al_2O_3 and V_2O_5 wt.% weighted average density. The apparent VO_x/m^2 surface density was calculated from the vanadium loading and the SSA.

Powder X-ray diffraction was measured on as-prepared powders using rotating sample holders, a rotating copper anode X-ray source, nickel filter and automatic anti-scatter and divergence slits with a scan speed of 0.0102 °/s (PANalytical X'Pert PRO).

Laser Raman spectroscopy was performed with a Horiba Jobin Yvon spectrometer (LabRAM HR) attached to an Olympus microscope. An Argon ion laser, tuned to the 514.5 nm line was used for excitation and the Raman scattered light was collected from 100 to 1100 cm^{-1} with a 1800 gratings/mm monochromator, 120 s integration time and 10 repeats to reduce the signal-to-noise ratio. The catalysts were pressed and crushed to 150 to 300 μm particles and placed in a modified fluidized bed in-situ cell (Linkham CCR1000). The catalysts were dehydrated in a flow of dry air at 550 °C and cooled to room temperature in flowing air before measuring the Raman spectra.

UV-vis diffuse reflectance spectra (Varian Cary 300 Bio) were recorded on the as-prepared powders using an integrating sphere (Labsphere DRA-CA-30I) with Spectralon as reference. Spectra were analyzed using the Kubelka-Munk theory, $F(R_\infty) = (1-R_\infty)^2/(2R_\infty)$ where R_∞ is the reflectance of an infinite layer relative to the reference. The absorption edge energy was determined as the *hv*-axis intercept of a straight line fitted to the low energy rise of a plot of $(F(R_\infty) \cdot hv)^2$ as function of *hv*, where *hv* is the photon energy in eV. For the 5, 7.5 and 10 wt.% V catalysts two absorption edges were observed and a straight line was fitted to each section on the $(F(R_\infty) \cdot hv)^2$ plot.

X-ray absorption spectroscopy was performed at the ANKA-XAS beamline at the ANKA synchrotron radiation source (Karlsruhe, Germany). The 10 wt.% V sample was

diluted with cellulose powder and pressed as a pellet for ex-situ measurement in transmission mode. The as-prepared FSP powder (3 to 5 mg) of the 3, 5 and 7.5 wt.% samples were placed in an in-situ transmission cell with graphite windows. EXAFS spectra of the as-prepared catalysts were recorded of all three samples. The 2 wt.% sample was loaded in a Kapton capillary to minimize background absorption for ex-situ measurement. The ex-situ EXAFS spectra were recorded from E = 5.315 to 6.445 keV in 385 steps with 1 s integration time per step at low energy and progressively longer integration time up to 4 s at the highest energy. Fourier transformations of the EXAFS spectra were performed with k^2-weighting in the k = 2 to 11 $Å^{-1}$ range. The 3, 5 and 7.5 wt.% V catalysts were investigated in-situ with simultaneous catalytic activity measurements and XANES when loaded in the transmission cell (7.5 wt.% V catalyst) or in a quartz capillary above a hot air blower (3 and 5 wt.% V catalysts) [121]. The catalysts were first oxidized at 550 °C in 10% O_2/He. Then the temperature was reduced to 400 °C and oxidative dehydrogenation of propane was performed using two reaction gas mixtures (2.5 % C_3H_8, 6.7 % O_2 or 5.0 % C_3H_8, 3.3 % O_2 and He balance) by ramping the temperature from 400 to 500 °C at 1°C/min. After re-oxidation in 10 % O_2/He at 500 °C, in-situ TPR (5 % H_2/He) with a temperature ramp of 5 °C/min from room temperature to 600 °C was performed. The 3 and 5 wt.% catalysts were only investigated in the richer gas mixture at slightly lower temperatures due to differences between the temperature of the capillary and the hot air blower. The total gas flow was 30 Nml/min in all experiments. XANES spectra were recorded from E = 5.400 to 6.000 keV in 1628 steps with 0.075 s integration time. This resulted in approximately 6 minutes for each spectrum including the time for initialization and monochromator movement. After normalization of the spectra the absorption edge energy E_0 values were determined as a set frac-

tion of the white-line intensity (0.80). Online gas analysis was performed by means of both mass spectrometry (Pfeiffer ThermoStar) and FTIR (MKS instruments) based gas analyzers. The reaction gas passed by the tip of the MS capillary, after which it was diluted with 200 or 400 Nml/min of nitrogen before flushing through the measurement cell of the FTIR gas analyzer. The conversion of oxygen was determined on basis of the m/z = 32 MS signal and the conversion of propane was determined on basis of its FTIR signal for the 7.5 wt.% V catalyst and on basis of the m/z = 29 MS signal for the 3 and 5. wt.% V catalysts. The FTIR was used to monitor the distribution between the three main reaction products CO, CO_2 and C_3H_6.

6.2.3 Catalytic activity and selectivity

The FSP powder was pressed and crushed to 150 to 300 μm sized particles, diluted with SiC (also 150 to 300 μm) and loaded in a fixed bed U-shaped quartz reactor with 4 mm inner diameter. The amounts of catalyst and SiC depended on the vanadia loading (see Table 6.3). For all activity measurement experiments the catalysts were pre-oxidized in dry air at 550 °C before cooling down to the lowest reaction temperature and introducing the ODP reaction gas with a fixed gas composition of $C_3H_8/O_2/N_2$ = 5/25/70 and flows of 50, 80, 120, 180 and 260 Nml/min. The temperatures were chosen to achieve 25 to 40 % propane conversion at the highest temperature and lowest flow rate.

The gas analysis was performed using a dual channel GC-MS. The nitrogen signal was used as internal standard so that all measured mole fractions were corrected for expansion of the gas due to combustion according to $y_i^{corr} = y_i \frac{y_{N_2}^{bypass}}{y_{N_2}}$. The conversion of propane, the selectivity to propene and the carbon atom based yields of propene and CO_x

were calculated according to $X = 1 - \frac{y_{C_3H_8}^{corr}}{y_{C_3H_8}^{bypass}}$, $S = \frac{y_{C_3H_6}^{corr}}{y_{C_3H_8}^{bypass} - y_{C_3H_8}^{corr}}$, $Y_{C_3H_6} = \frac{y_{C_3H_6}^{corr}}{y_{C_3H_8}^{bypass}}$ and $Y_{CO_x} = \frac{y_{CO}^{corr} + y_{CO_2}^{corr}}{3 \cdot y_{C_3H_8}^{bypass}}$.

The space time yield was calculated as $STY = \frac{[C_3H_6] \cdot F \cdot M_{C3H6}}{w}$, where $[C_3H_6]$ is the outlet concentration of propene in mol/l, F is the flow in Nl/h, M_{C3H6} the molar mass of propene in g/mol and w the mass of catalyst in g.

Further details of the catalytic activity setup are given in Section 2.2.

6.3 Results and discussion

6.3.1 Catalyst preparation, surface area and vanadia surface density

Five representative alumina supported vanadia catalysts prepared by FSP are listed in Table 6.1. Approximately 1 g of catalyst powder was obtained for each sample after combusting 100 ml precursor solution and collecting on two filters. All samples appeared yellow directly after synthesis, but slowly turned green after storage in ambient atmosphere.

The BET surface area of all the samples was in the range of 143 to 169 m^2/g, corresponding to average particle diameters from 9.0 to 10.9 nm assuming spherical particles (see Table 6.1), hence the FSP synthesis resulted in high surface area alumina supported vanadia. The surface area was much higher with the preparation method used here compared to Rossetti et al. [98]. The apparent vanadia surface density was calculated from the vanadium loading and the measured BET surface area. This ranged from 1.4 to 8.4 VO_x/nm^2, covering the range from sub-monolayer of vanadia monomers at around 2.3

to 2.5 VO_x/nm^2 to above the monolayer coverage of vanadia oligomers at around 7.5 to 8.0 VO_x/nm^2 [34,67].

Table 6.1: Overview of the VO_x/Al_2O_3 catalysts prepared by flame spray pyrolysis, specific surface area (SSA), BET equivalent particle diameter and apparent vanadium surface density.

Sample	*SSA* (m^2/g)[a]	d_p (nm)[b]	$VO_x/(nm^2)$[c]
2 wt.% V	166	9.2	1.4
3 wt.% V	169	9.0	2.1
5 wt.% V	168	9.1	3.6
7.5 wt.% V	148	10.4	6.0
10 wt.% V	143	10.9	8.4

[a]6 point BET measurement, [b]calculated from the *SSA* assuming spherical particles, [c]calculated from the *SSA* and the vanadia loading.

6.3.2 Powder X-ray diffraction

The as-prepared catalysts were first investigated with XRD. All samples showed the γ-alumina phase with very broad reflections, in agreement with small primary particles (see Figure 6.1). The reflections are broader and decrease in intensity with increasing vanadia loading, possibly due to distortion of the crystalline alumina phase with increasing vanadia content. Up to 7.5 wt.% vanadium loading, γ-alumina was the only phase observed, but at 10 wt.% V traces of crystalline V_2O_5 were observed by a very broad reflection at around $2\theta = 27°$ [122]. This was in agreement with the surface density of the 10 wt.% V sample being above the theoretical monolayer. However, earlier studies showed that vanadia supported on titania prepared by FSP did not exhibit crystalline vanadia until significantly above the theoretical monolayer [34,123-124]. On titania supported samples the V_2O_5 reflection at $2\theta = 27°$ may be hard to observe if the particles are small and the reflection broad, since it will overlap with the anatase reflection at $2\theta = 25°$.

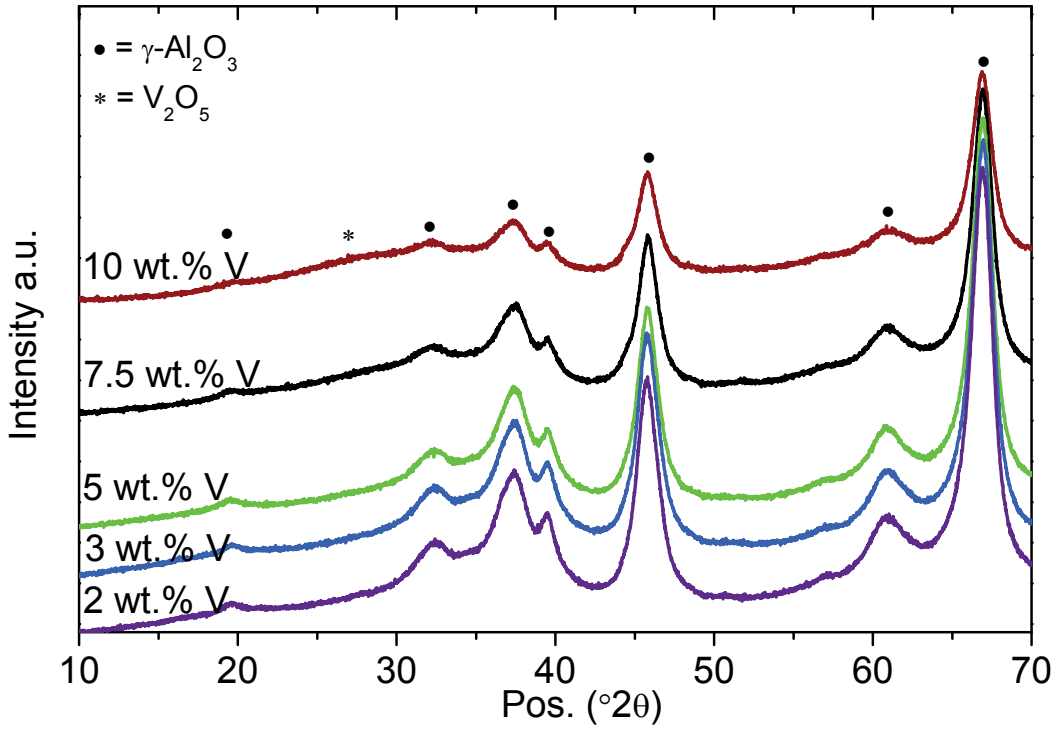

Figure 6.1: Powder X-ray diffraction patterns of the five FSP synthesized VO_x/Al_2O_3 catalysts measured on the as-prepared powders. Only γ-Al_2O_3 is observed, with very weak traces of crystalline vanadia around $2\theta = 27°$ for the 10 wt.% V catalyst.

6.3.3 Raman spectroscopy

Raman spectroscopy was performed on all five samples. Prior to measuring the Raman spectrum at room temperature the samples were dehydrated in dry air at 550 °C, similarly to the pre-oxidation step in the catalytic tests (see Section 6.3.6). The high quality of the spectra allowed several bands to be clearly observed (see Figure 6.2). There has been much debate in the literature about the assignment of the broad bands observed between 750 to 1000 cm^{-1} and the vanadyl (V=O) stretching band around 1031 cm^{-1} [67,84,86-87,91,125-131]. All five samples showed the vanadyl stretching band at 1031 cm^{-1}. This was typically assigned to vanadia monomers [91,129], however, since it was observed at all loadings in this study it must also be indicative of vanadia oligomers

[87]. The bands around 900 to 950 have been assigned to V-O-V stretching bands of the vanadia oligomers, but also to V-O-Al stretching bands for both monomers and oligomers [87]. Since they were observed at all loadings in this study this supports the latter interpretation. Bands at 534 and 775 cm^{-1} were clearly observed for the 5, 7.5 and 10 wt.% V samples, only weakly observed at 3 wt.% V and not observed at 2 wt.% V. These bands could thus be due to V-O-V stretching of vanadia oligomers, since these vibrations are expected at lower frequency than the V-O-Al vibrations [87]. A band at 1015 cm^{-1} was observed for the 10 wt.% V sample, and as a shoulder to the vanadyl stretching band of the 7.5 wt.% V catalyst, which may be due to formation of small crystalline domains of V_2O_5 in agreement with the XRD results. However, for highly loaded vanadia on alumina catalysts the vanadyl stretching band of bulk V_2O_5 was observed around 997 cm^{-1} [91]. Since the Raman scattering cross section for crystalline V_2O_5 is much higher than that of the supported vanadia species the amount of crystalline vanadia must be very low [131]. In summary, the 2 and 3 wt.% V samples contained mainly vanadia monomers, the 5 wt.% V sample contained a mixture of monomers and oligomers and the 7.5 and 10 wt.% V samples contained mainly vanadia oligomers with few small domains of crystalline V_2O_5. From the Raman and XRD results it was concluded that very little crystalline V_2O_5 is formed after FSP synthesis and dehydration at 550 °C compared to the studies by Argyle et al. [91] using incipient wetness impregnation, Kondratenko and Baerns [132] using evaporation impregnation and Rossetti et al. [16] using FSP based on an aluminium nitrate precursor in alcoholic solution.

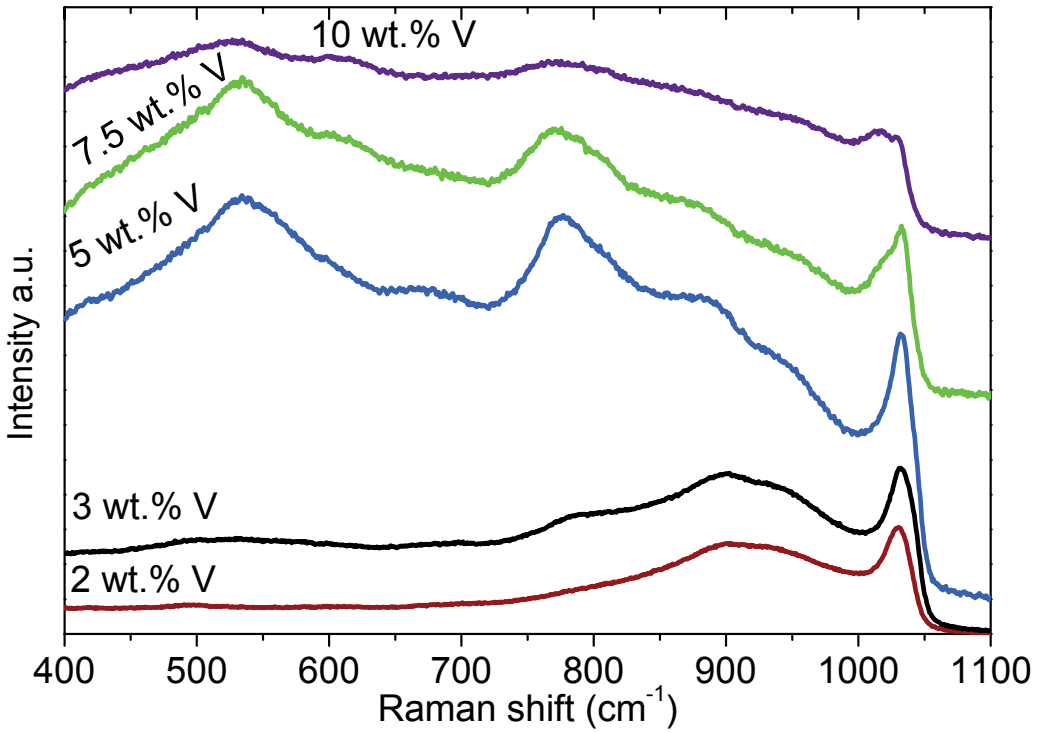

Figure 6.2: Laser Raman spectra of the five FSP synthesized VO_x/Al_2O_3 catalysts measured at room temperature in a flow of dry air after dehydration at 550 °C. Traces of crystalline vanadia were observed for the 10 wt.% V catalyst (band at 1015 cm^{-1}), otherwise supported vanadia was observed. Mostly monomers for the 2 and 3 wt.% V catalysts, a mixture of monomers and oligomers for the 5 wt. % catalyst and mostly oligomers for the 7.5 and 10 wt.% V catalysts are observed.

6.3.4 UV-vis diffuse reflectance spectroscopy

The as-prepared FSP powders were additionally investigated with diffuse reflectance UV-vis spectroscopy. The visible colors of the powders were from light to dark green. The reflectance spectra in terms of the Kubelka-Munk function showed a minimum in absorption around 500 to 550 nm, in agreement with the green color (see Figure 6.3).

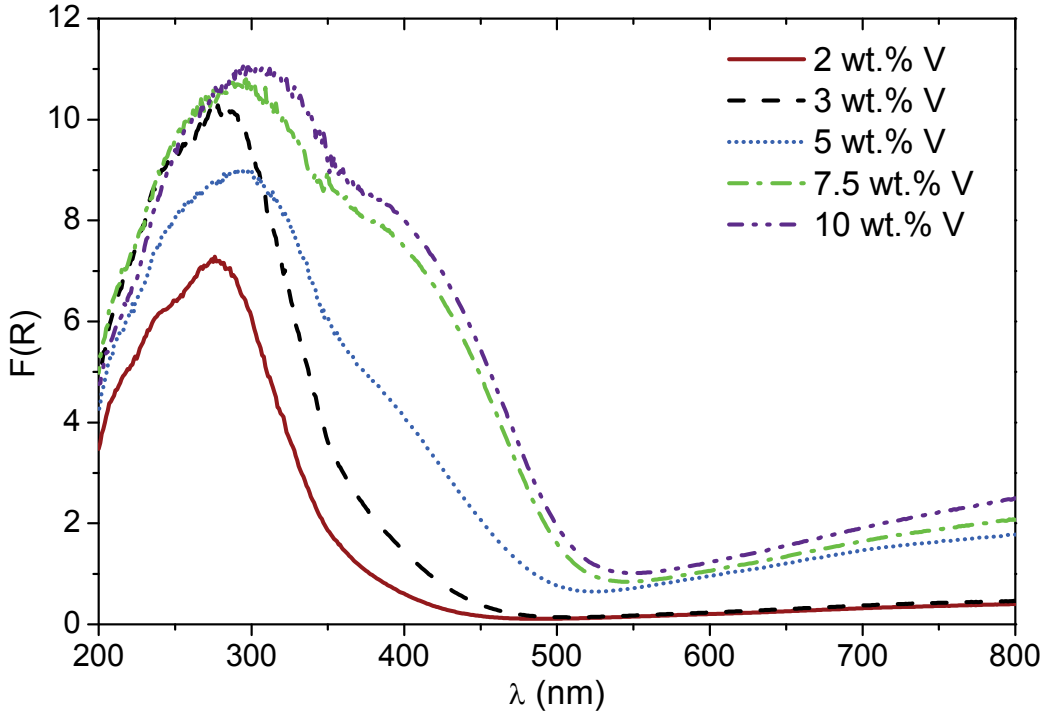

Figure 6.3: UV-vis spectra of the five FSP synthesized VO_x/Al_2O_3 catalysts measured at room temperature in the hydrated state of the as-prepared catalysts. The observation of two vanadia LMCT absorption bands for the 5 to 10 wt.% V catalysts (Table 6.2) indicates oligomers, whereas for the 2 and 3 wt.% V catalysts only one LMCT absorption edge was observed indicating mostly monomers. Absorption in the 600 to 800 nm region was due to *d–d* transitions of reduced vanadia stabilized in the form of oligomers.

The 2 and 3 wt.% V catalysts had very low absorption in the visible region of the spectrum. In the UV-region a strong ligand to metal charge transfer (LMCT) band due to the $O \rightarrow V^{5+}$ transition was observed around 275 nm. This is in agreement with the results derived from Raman spectroscopy for those catalysts indicating mostly the presence of vanadia monomers. The 5, 7.5 and 10 wt.% V catalysts had some absorption in the visible part of the spectra, possibly due to *d–d* transitions of V^{3+} or V^{4+} species, indicating that vanadia may be partly reduced and stabilized in the form of oligomers directly after synthesis [130,132]. For these catalysts the $O \rightarrow V^{5+}$ LMCT band was observed around 295 to 305 nm, with another $O \rightarrow V^{5+}$ LMCT band at lower energy around 400 to 430

nm appearing as a shoulder to the high energy LMCT band, as previously observed for alumina supported vanadia [133-134]. The intensity of this LMCT band was much higher for the 7.5 and 10 wt.% V catalysts compared to the 5 wt.% V catalyst. This indicated that the 400 to 430 nm LMCT band, appearing weakly for the 5 wt.% V catalyst and strongly for the 7.5 and 10 wt.% V catalysts, was due to vanadia oligomers. For better comparison, the positions of the absorption edges were determined (see Table 6.2). For the 2 and 3 wt.% V catalyst only one LMCT band and one absorption edge was observed and for the 5, 7.5 and 10 wt.% V catalysts two LMCT bands and two absorption edges were observed. The first absorption edge was observed between 3.06 and 3.75 eV and the second absorption edge was observed between 2.56 and 2.75 eV. With increasing vanadia content the edge energy decreased, corresponding to a decrease in the band gap, indicating formation of larger domains of vanadia oligomers. This is in agreement with vanadia impregnated hexagonal mesoporous silica where high loadings lead to absorption edges around 2.4 eV, interpreted as mainly octahedrally coordinated vanadia oligomers [135]. At low loadings absorption edges around 3.5 to 3.8 eV were observed, interpreted as a mixture of vanadia monomers and oligomers in tetrahedral coordination [135]. The absorption edge for tetrahedrally coordinated oligomers is expected around 3.16 eV and for monomers at 3.82 eV [135]. The absorption edge energies determined in this study where however still significantly higher than the absorption edge energy of bulk V_2O_5 (octahedrally coordinated vanadia oligomers) at approximately 2.00 to 2.26 eV [91,131,135].

Table 6.2: UV-vis diffuse reflectance spectroscopy edge energies in the hydrated state of the VO_x/Al_2O_3 catalysts prepared by flame spray pyrolysis

Sample	Edge 1 (eV)[a]	Edge 2 (eV)[a,b]
2 wt.% V	3.75	-
3 wt.% V	3.61	-
5 wt.% V	3.32	2.75
7.5 wt.% V	3.10	2.59
10 wt.% V	3.06	2.56

[a]Determined as the *x*-axis intercept of a straight line fitted to the low energy rise of a plot of $(F(R_\infty) \cdot h\nu)^2$ as function of $h\nu$ (photon energy in eV). [b]Two absorption edges and two straight sections observed in the $(F(R_\infty) \cdot h\nu)^2$ plot.

6.3.5 X-ray absorption spectroscopy

All five vanadia samples were investigated ex-situ with extended X-ray absorption fine structure (EXAFS) spectroscopy. The normalized X-ray absorption near edge structure (XANES) spectra and k^2-weighted EXAFS functions (see Figure 6.4 and Figure 6.5(a)) fell in two categories, with the 2 and 3 wt.% V samples being similar and the 5, 7.5 and 10 wt.% V samples being similar, respectively. This is in good agreement with the UV-vis and Raman spectroscopy data. The k^2-weighted Fourier transformed EXAFS functions only showed the nearest neighbor V-O backscattering shell (see Figure 6.5 (b)). This is in agreement with other EXAFS studies of supported vanadia catalysts in the hydrated state [127,136] and is consistent with the Raman and XRD results which showed little or no formation of crystalline V_2O_5.

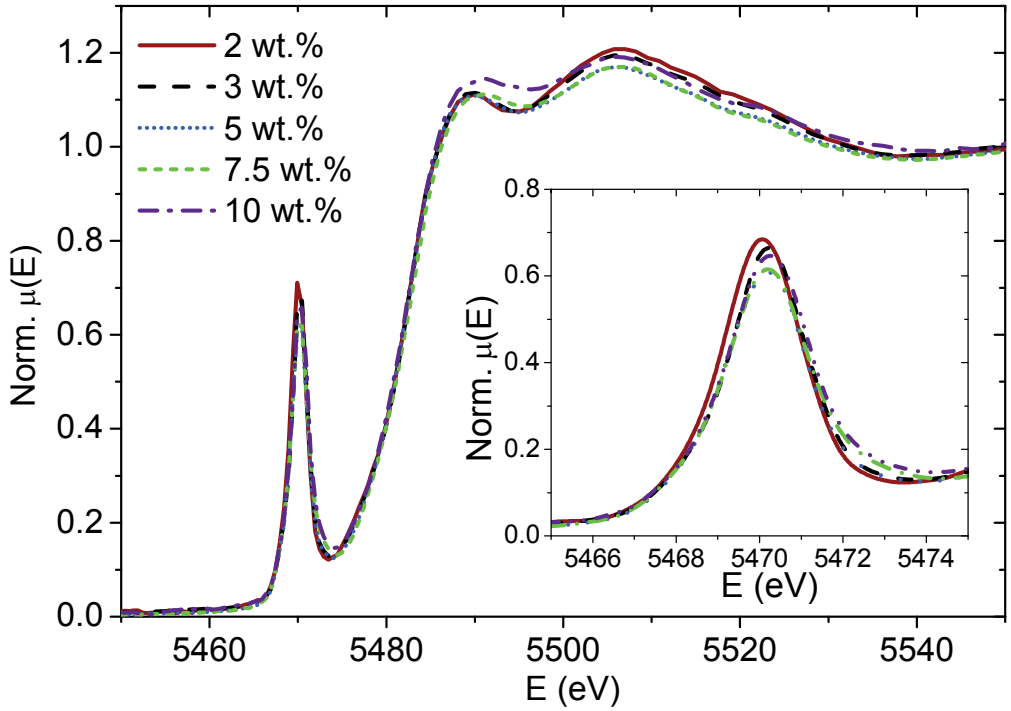

Figure 6.4: Normalized XANES spectra of the five FSP synthesized VO_x/Al_2O_3 catalysts measured at room temperature in the hydrated state of the as-prepared catalysts. The 2 and 3 wt.% V samples and 5 and 7.5 wt.% V samples are similar. The insert shows a magnification of the pre-edge region.

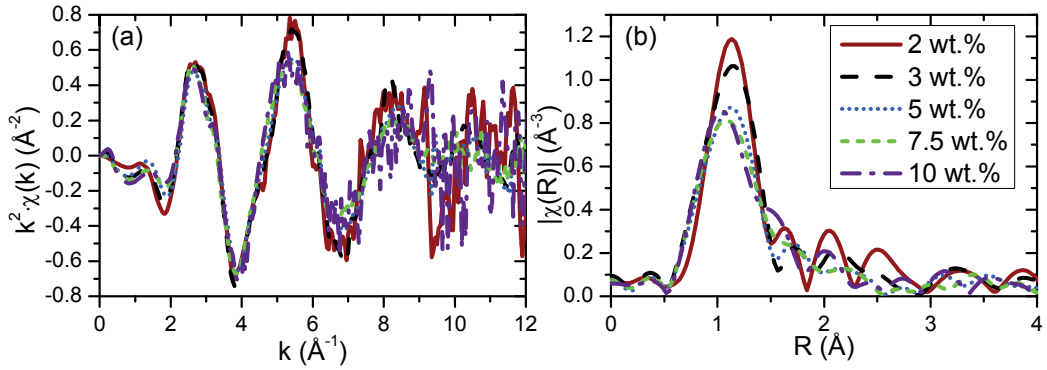

Figure 6.5: (a) k^2-weighted EXAFS spectra of the five FSP synthesized VO_x/Al_2O_3 catalysts measured at room temperature in the hydrated state (as-prepared catalysts); (b) Fourier transformed k^2-weighted EXAFS spectra (k = 2 to 11 Å-1) of the five corresponding VO_x/Al_2O_3 catalysts measured at room temperature. The 2 and 3 wt.% V samples as well as the 5, 7.5 and 10 wt.% V samples are similar, in good agreement with Raman (Figure 6.2) and UV-vis spectroscopy (Figure 6.3).

The 7.5 wt.% V sample was investigated by XANES spectroscopy while simultaneously performing the ODP reaction. After heating the sample to 550 °C in flowing 10 % O_2/He and cooling to 400 °C, propane was introduced to create a reaction mixture of 6.7 % O_2/2.5 % C_3H_8/He. During a temperature ramp of 1 °C/min to 500 °C a propane conversion of up to 20 % and an oxygen conversion of up to 40 % was observed. XANES spectra were recorded simultaneously (approximately 6 minutes for each spectrum). The edge position did not change significantly during this experiment, showing that the vanadia stayed fully oxidized (see Figure 6.6). The temperature was lowered to 400 °C and the gas composition was changed to a richer reaction mixture of 3.3 % O_2/5.0 % C_3H_8/He. Ramping the temperature to 500 °C resulted in propane conversion of up to 8 % and oxygen conversion of up to 75 %. From 460 to 500 °C, where the oxygen conversion is approximately 60 to 75 %, there was a significant reduction in the absorption edge energy showing that the vanadia was reduced from V^{5+} to V^{4+}/V^{3+}. This is consistent with conclusions from previous in-situ UV-vis diffuse reflectance spectroscopy experiments by Gao et al. [130]. Following the evolution of the products it was observed that CO and CO_2 were the main products (see Figure 6.6). When the vanadia reduction occurred in the richer reaction mixture the rates of CO and CO_2 formation reduced, while the propene formation rate was constantly low throughout the experiment.

Similar experiments were performed with the 3 and 5 wt.% V catalysts using only the richer reaction mixture with the catalysts loaded in a capillary cell. For the 5 wt.% V catalyst the conversion of oxygen was up to 80 %, with some indication of vanadia reduction at 479 °C, the highest temperature investigated (see Figure 6.7). Propene was the main product below 410 °C, but with increasing temperature the main products were CO and CO_2. For the 3 wt.% V catalyst the conversion of oxygen was only up to 20 %

at 506 °C (see Figure 6.8), due to the much lower activity of this catalyst (see Section 3.6). There was no indication of vanadia reduction and propene was the main product in the whole temperature range (369 to 506 °C).

This showed that operating the catalysts at almost complete oxygen conversion, in order to optimize the selectivity to propene, may result in reduction of the active vanadium sites leading to lower activity. Since this only occurred for the 7.5 wt.% V catalyst, it appeared to be particular significant for vanadia oligomers, in agreement with the investigation by Gao et al. [130]. Another disadvantage of low oxygen concentration is the increased potential for coke formation, which should be avoided in order to retain the benefits of oxidative dehydrogenation over anaerobic dehydrogenation.

To verify the reduction of the vanadia the investigated 7.5 wt.% V sample was re-oxidized in 10 % O_2/He and after cooling to room temperature, in-situ XAS studies during temperature programmed reduction (TPR) in 5 % H_2/He was performed (see Figure 6.9). The MS traces of the gas analysis showed consumption of hydrogen and formation of water between 350 and 550 °C, indicating reduction of the vanadia, which correlated with a significant shift of the absorption edge energy by 4 eV, in fact to values lower than what was obtained in the in-situ ODP experiments (see Figure 6.10). Hence, vanadia was only partly reduced in the ODP experiment (maximum shift observed was 2 eV). For comparison the measured absorption edge energies during the in-situ ODP experiments in the richer gas mixture and during the TPR experiment for the 3 and 5 wt.% V samples are shown in Figure 6.11, showing that the catalyst stays oxidized during the ODP experiments.

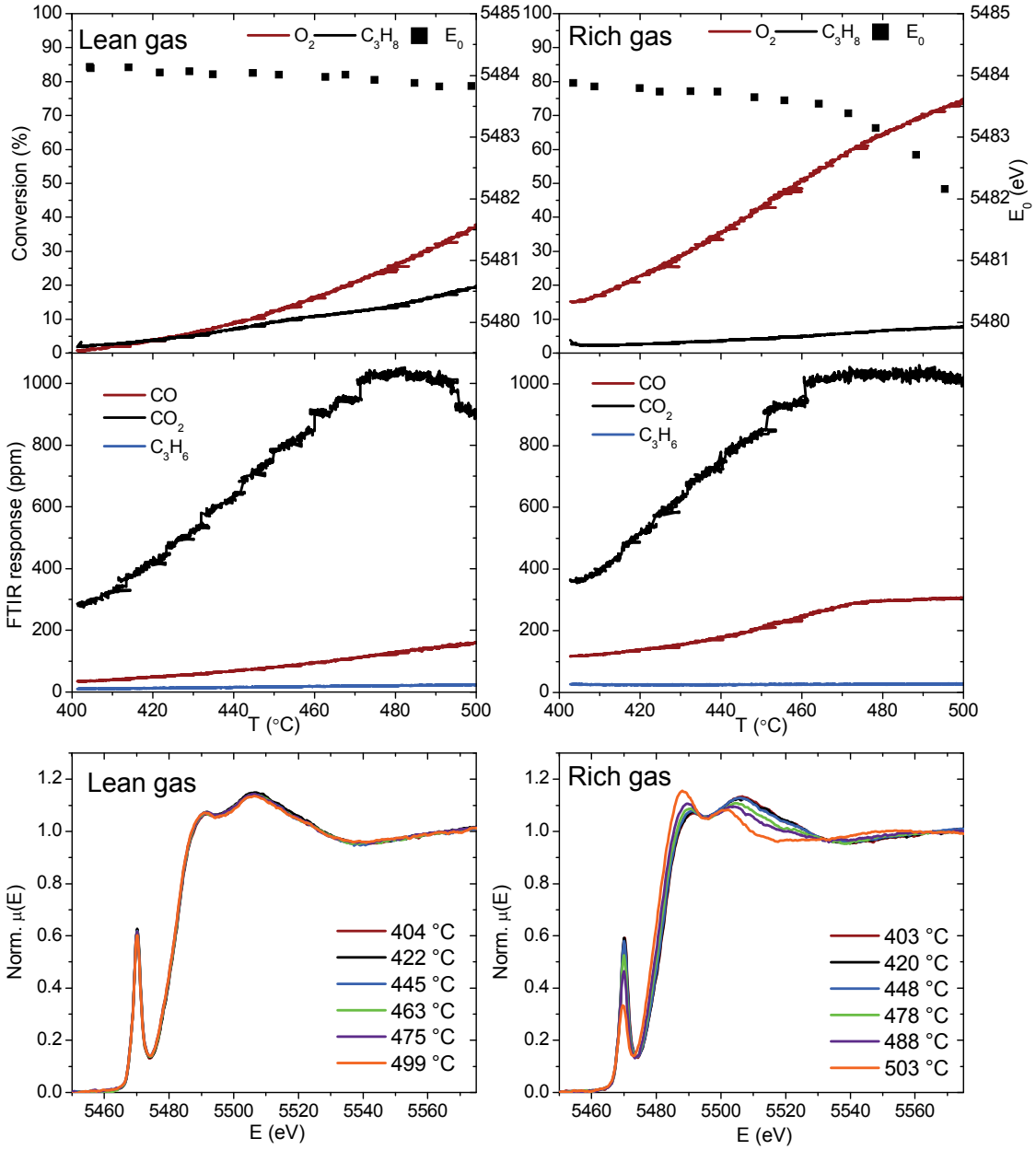

Figure 6.6: X-ray absorption edge energy (E_0, top) determined from XANES spectra (bottom), oxygen and propane conversion (top) and FTIR gas analyzer traces for the three main products CO, CO_2 and propene (middle) during in-situ oxidative dehydrogenation experiments with the 7.5 wt. % V catalyst using lean (6.7 % O_2/2.5 % C_3H_8/He) and rich (3.3 % O_2/5.0 % C_3H_8/He) gas mixtures. Decreasing absorption edge energy corresponds to reduction of vanadium to $V^{3+/4+}$.

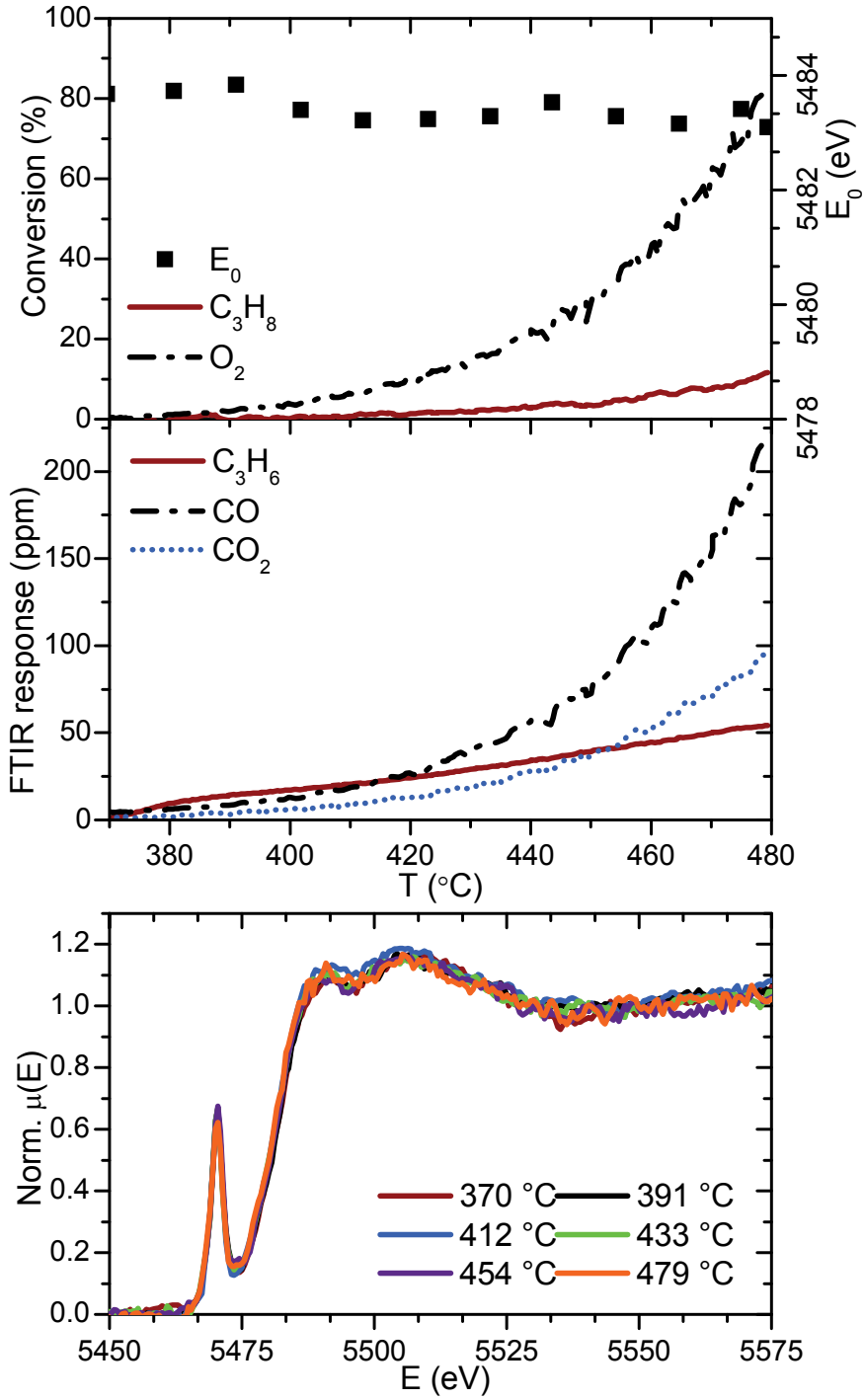

Figure 6.7: X-ray absorption edge energy (E_0, top) determined from XANES spectra (bottom), oxygen and propane conversion (top) and FTIR gas analyzer traces for the three main products CO, CO_2 and propene (middle) during in-situ oxidative dehydrogenation experiments with the 5 wt. % V catalyst using rich (3.3 % O_2/5.0 % C_3H_8/He) gas mixtures. Constant edge energy indicates that the vanadia remained oxidized.

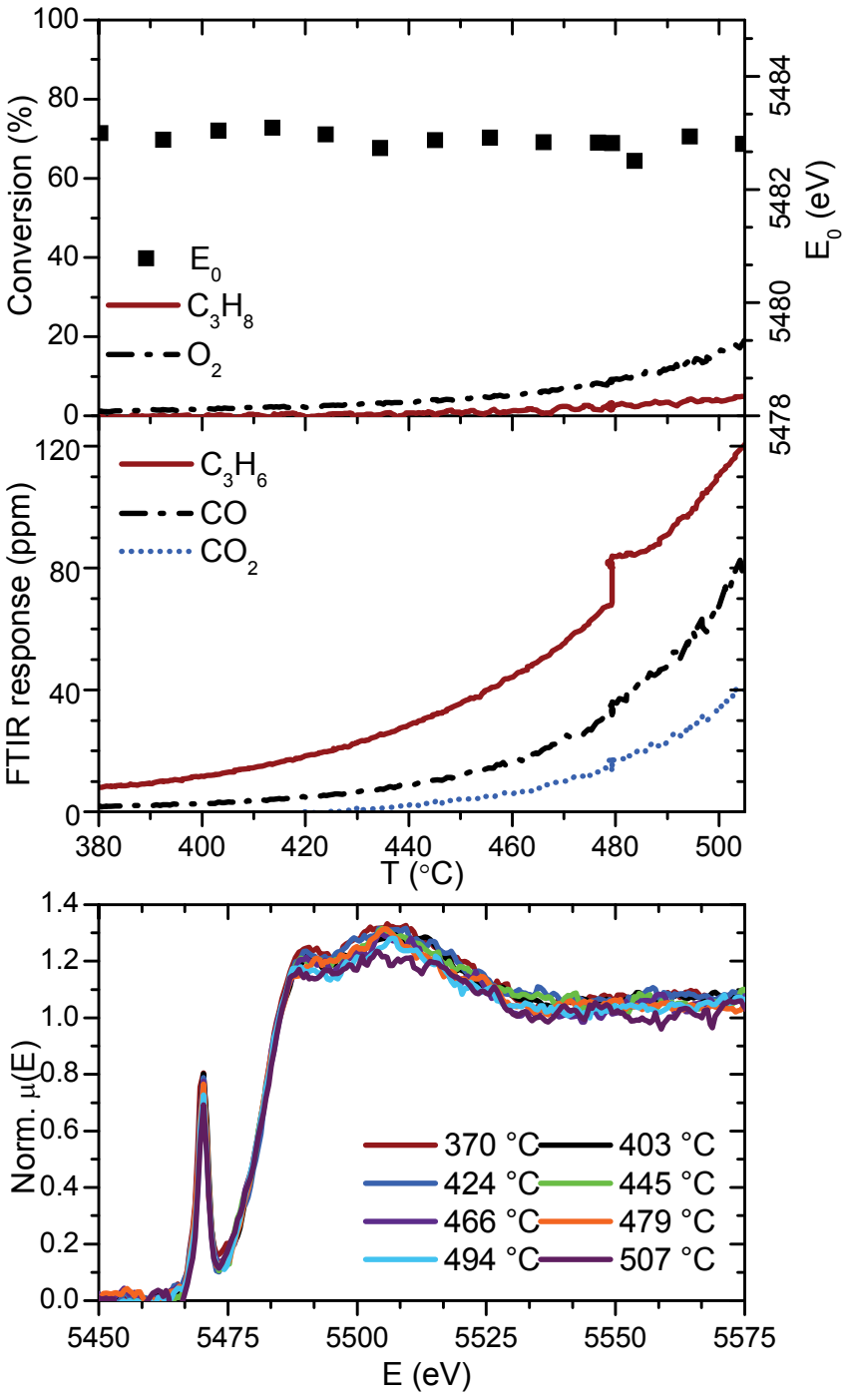

Figure 6.8: In-situ XANES data during the oxidative dehydrogenation experiments over the 3 wt. % V catalyst using rich (3.3 % O_2/5.0 % C_3H_8/He) gas mixtures with X-ray absorption edge energy (E_0, top) determined from XANES spectra (bottom), oxygen and propane conversion (top) and FTIR gas analyzer traces for the three main products CO, CO_2 and propene (middle). Constant edge energy indicates that the vanadia remained oxidized.

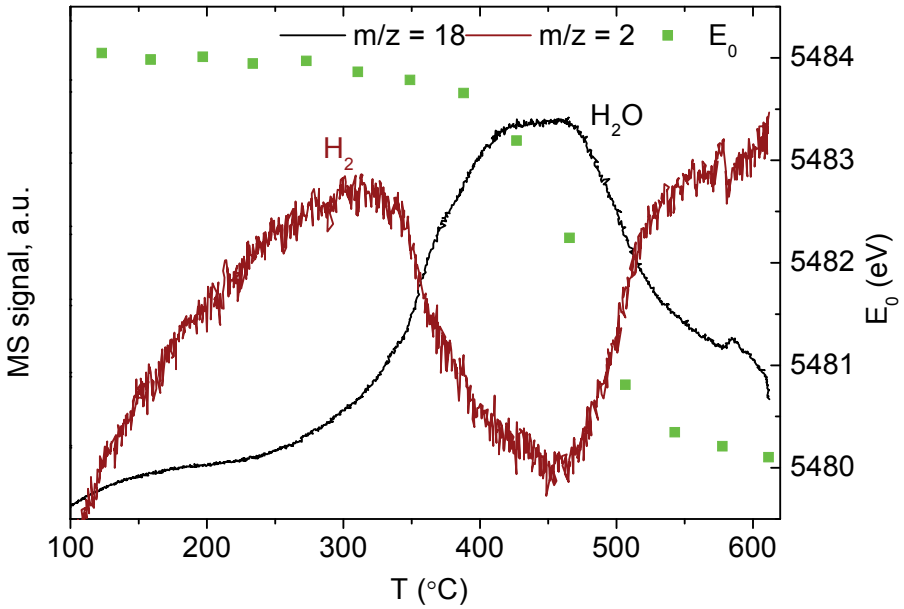

Figure 6.9: In-situ XANES studies of the 7.5 wt. % V catalyst during H_2-TPR (5 % H_2/He, 30 ml/min, 5°C/min to 600 °C) with MS gas analysis: X-ray absorption edge energy E_0, formation of water and consumption of hydrogen as function of temperature. The decrease in absorption edge energy is correlated with the consumption of hydrogen and the formation of water confirming the reduction of vanadium.

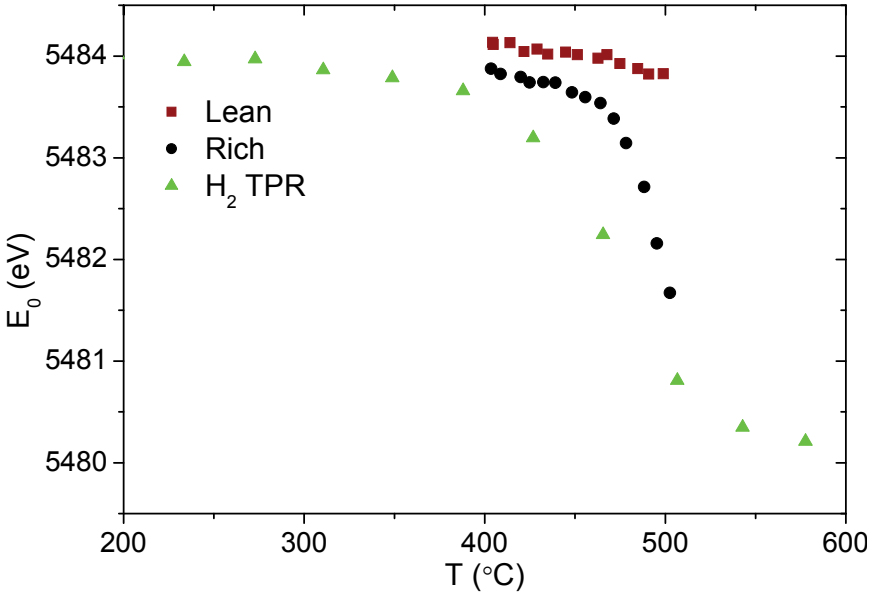

Figure 6.10: Comparison of the absorption edge energies for the 7.5 wt.% V sample during in-situ experiments in lean (6.7 % O_2/2.5 % C_3H_8/He) and rich (3.3 % O_2/5.0 % C_3H_8/He) reaction gas mixtures and TPR gas mixture (5 % H_2/He).

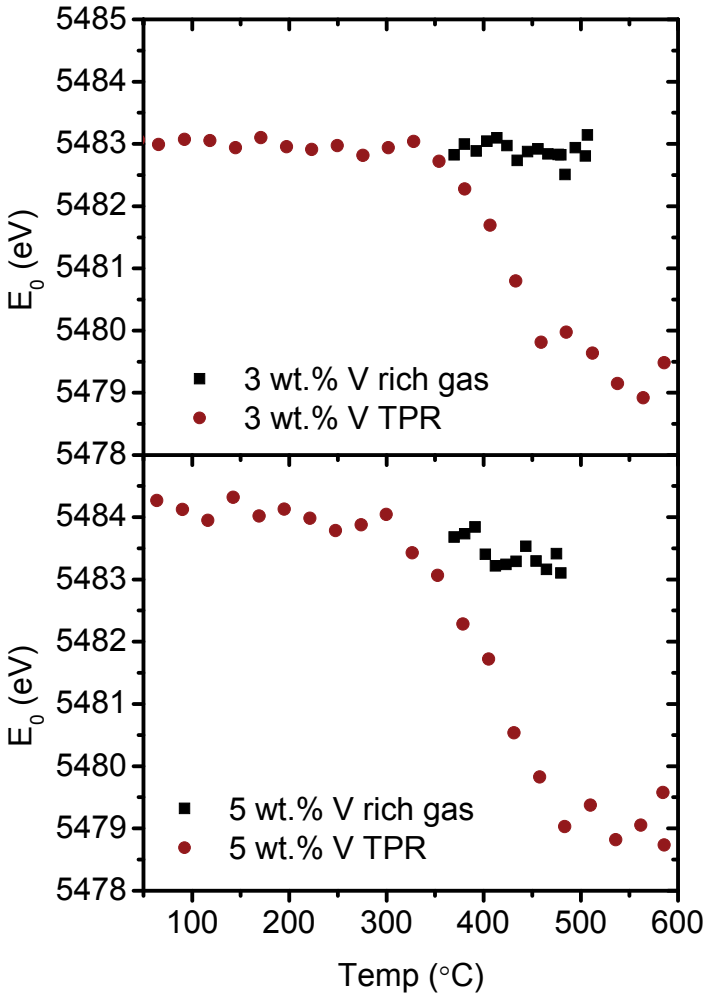

Figure 6.11: Comparison of the absorption edge energies for the 3 (top) and 5 wt.% V (bottom) samples during in-situ experiments in rich reaction gas mixture (3.3 % O_2/5.0 % C_3H_8/He) and TPR gas mixture (5 % H_2/He).

6.3.6 Catalytic activity and selectivity

The five selected and above in depth characterized catalysts were evaluated for the oxidative dehydrogenation of propane in a lab scale experiment. The catalysts were pre-oxidized in air at 550 °C before the experiments to make sure that the vanadia was fully oxidized and to remove any carbonaceous deposits from the FSP synthesis. Due to the different amounts of vanadia the amount of catalyst and the reaction temperature were

optimized for the individual catalysts (see Table 6.3). The inlet gas composition was always $C_3H_8/O_2/N_2$ = 5/25/70 and the flows were 50, 80, 120, 180 and 260 Nml/min. The high concentration of oxygen was chosen to avoid reduction of the catalyst and to perform truly oxidative dehydrogenation. The temperature was kept below 500 °C since homogeneous combustion of propane was observed from approximately 520 °C and above. The pressure was kept close to ambient pressure; typically the pressure drop over the catalyst bed was between 0.05 to 0.3 bar, with the highest pressure drop at the highest flow and temperature.

Table 6.3: Variable conditions for the catalytic activity measurements. All experiments were performed with a gas mixture of $C_3H_8/O_2/N_2$ = 5/25/70 and flows from 50 to 260 Nml/min.

Sample	m_{cat} (mg)	m_{SiC} (mg)	T (°C)[a]
2 wt.% V	150	350	460-500
3 wt.% V	100	400	440-480
5 wt.% V	75	450	390-430
7.5 wt.% V	75	450	360-400
10 wt.% V	75	450	360-400

[a]Three temperatures in steps of 20 °C were investigated

Besides propene, CO and CO_2 were the main products. The selectivity to ethylene and acrolein was below 0.5 % in all experiments and only traces of acetylene and acetaldehyde were observed when the propane conversion was above 30 %. This showed that cracking and non-oxidative dehydrogenation only occurred to a very small extent. For all reaction conditions the carbon atom mass balance was better than 98 % and the sum of selectivities between 80 and 110 %. The uncertainty in the selectivity measurements increased with decreasing propane conversion.

The 2 and 3 wt.% V catalysts had almost similar selectivity as function of propane conversion (see Figure 6.12), and the maximum propene yields were also approximately the same, 12.6 and 11.1 % respectively, for the two catalysts (see Table 6.4). Due to the

lower amount of active material the weight based activity of the 2 wt.% catalyst was lower than that of the 3 wt.% catalyst. The maximum space time yield (STY) obtained for the 3 wt.% V catalyst was 0.782 $g_{propene}/(g_{cat} \cdot h)$, significantly better than the maximum STY of the 2 wt.% V catalyst of 0.577 $g_{propene}/(g_{cat} \cdot h)$ (see Table 6.4). The 5 wt.% V catalyst, which contained a mixture of vanadia monomers and oligomers, had intermediate selectivity and propene yield, while the 7.5 and 10 wt.% V catalysts, which contained mostly vanadia oligomers, had low selectivities and propene yields (see Figure 6.12 and Table 6.4). The 7.5 and 10 wt.% V catalysts had almost the same selectivity as function of propane conversion (see Figure 6.12). This showed that the most selective catalysts were obtained at the lowest vanadia loadings, where vanadia monomers were the most abundant vanadia species. This is in agreement with the results reported by Argyle et al. [91] and Bulánek et al. [135] but in contrast to the results reported by Kondratenko and Baerns [132]. The difference may lie in the synthesis method of Kondratenko and Baerns, where high vanadia loadings resulted in low specific surface area and formation of large amounts of crystalline V_2O_5. The maximum STY obtained decreased when the vanadia loading increased from 3 to 10 wt.% V, since the propene selectivity decreased. Comparing the maximum STY (see Table 6.4) of the 3 wt.% V catalyst prepared by FSP with literature values compiled by Cavani et al. the performance of this catalyst was very good, since only a few catalysts reported have STY above 0.75 $g_{propene}/(g_{cat} \cdot h)$ [61]. Comparing the selectivity as function of conversion, the 2 and 3 wt.% V catalysts prepared by FSP showed better selectivity than the vanadia on alumina catalysts prepared by impregnation reported by Lemonidou et al. [78] and similar selectivity to those reported by Dinse et al. [77], Frank et al. [137] and Kondratenko and Baerns [132], despite the much higher oxygen to propane ratio used in this study. The

selectivity as function of conversion was also significantly better in this study than for the V-Al-oxide catalysts prepared by FSP by Rossetti et al. [98]. Note however, that the surface area for those catalysts was significantly lower. This shows that the formation of supported vanadia species on high surface area alumina rather than crystalline vanadia or vanadium aluminate is important for high selectivity in ODP.

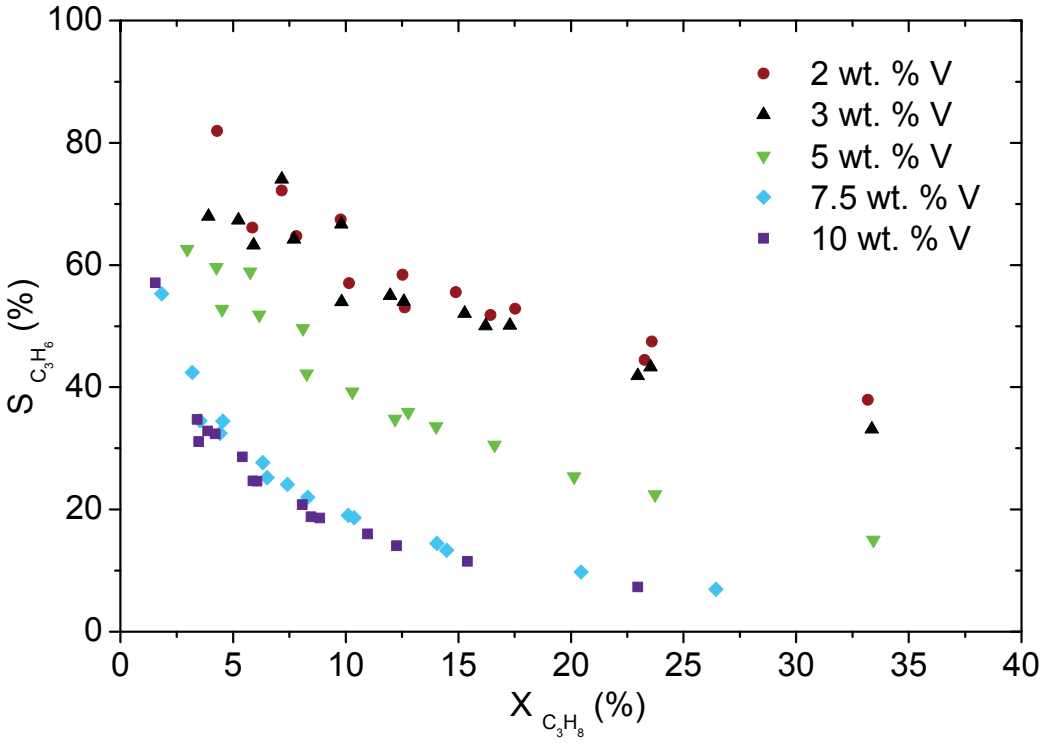

Figure 6.12: Propene selectivity as function of propane conversion measured on the five FSP synthesized VO_x/Al_2O_3 catalysts. The catalysts were pre-oxidized in air at 550 °C. The gas composition during oxidative dehydrogenation was $C_3H_8/O_2/ N_2$ = 5/25/70 and flows from 50 to 260 Nml/min (see Table 6.3).

Table 6.4: Maximum propene yields obtained and the corresponding propane conversions and the maximum space time yields obtained at the highest temperature and flow rate (260 Nml/min).

Sample	***Y* (%)**	***X* (%)**	***STY* ($g_{propene}/[g_{cat}\cdot h]$)[a]**	***T*(°C)[b]**
2 wt.% V	12.6	33.2	0.577	505
3 wt.% V	11.1	33.4	0.782	488
5 wt.% V	5.3	23.7	0.517	444
7.5 wt.% V	2.0	14.2	0.353	410
10 wt.% V	1.8	15.4	0.300	414

[a] maximum measured space time yield [b] temperature measured in the catalyst bed

6.4 Conclusions

Highly active and selective vanadia on alumina oxidative dehydrogenation of propane catalysts have been prepared by flame spray pyrolysis. The catalysts had higher specific surface areas than previous flame-made vanadia on alumina catalysts with 143 to 169 m^2/g and apparent vanadia surface densities from 1.4 to 8.4 VO_x/nm^2. The only alumina phase formed was γ-Al_2O_3, as observed with XRD. At low vanadia loadings of 2 and 3 wt.% V mainly supported vanadia monomers were produced, at intermediate loading of 5 wt.% V a mixture of supported vanadia monomers and oligomers were formed and at high loadings of 7.5 and 10 wt.% V mainly vanadia oligomers and traces of crystalline vanadia were formed, as observed with XRD, Raman spectroscopy, diffuse reflectance UV-vis spectroscopy and X-ray absorption spectroscopy. At 2 and 3 wt.% V the propene selectivity was high, resulting in propene yields of up to 12 % and space time yields of up to 0.78 $g_{propene}/(g_{cat} \cdot h)$, which is high compared to values obtained for vanadia on alumina catalysts prepared by impregnation. The propene selectivity decreased with increasing vanadia loading showing that the most selective active species were vanadia monomers. In-situ XANES showed that the vanadia can be reduced when the oxygen concentration is low, particular for vanadia oligomers, resulting in lower catalytic activity, but improved selectivity.

7. Kinetics of oxidative dehydrogenation of propane over vanadia on alumina catalysts prepared by flame spray pyrolysis

7.1 Introduction

In order to find the optimal reaction conditions the kinetics of the ODP reaction, over the previously synthesized and characterized vanadia on alumina catalysts (see Section 6), were investigated.

7.2 Experimental

7.2.1 Catalyst preparation and characterization

The catalysts were prepared and characterized as described in Section 6.1.

7.2.2 Catalytic evaluation

The catalysts evaluated as described in Section 6.1. The 7.5 wt.% V catalyst was also evaluated using 15 mg of catalyst and temperatures from 440 to 480 °C furnace set-points (compared to 75 mg and 360 to 400 °C as described in Section 6.1), for experimental comparison to the predictions of the kinetic model. Besides, a series of experiments with the 7.5 wt. % V catalyst were performed at reducing conditions with gas compositions $C_3H_8/O_2/N_2$ = 5/10/85, 5/5/90, 5/3/92 and 5/2/93 using 15 mg of catalyst, temperatures of 460 and 480 °C and a total gas flow of 100 Nml/min.

Oxidation of propene was investigated with the 5 wt.% V catalyst using 60 mg of catalyst, gas composition $C_3H_6/O_2/N_2$ = 1/25/74, total flows of 180 and 260 Nml/min and temperatures from 340 to 400 °C.

7.3 Kinetic model

The reaction scheme consisting of three reactions with rate constants k_1', k_2' and k_3' were:

$$C_3H_8 + \frac{1}{2}O_2 \xrightarrow{k_1'} C_3H_6 + H_2O \quad (A)$$

$$C_3H_8 + \left(2 + \frac{3}{2}x\right)O_2 \xrightarrow{k_2'} 3CO_x + 4H_2O \quad (B)$$

$$C_3H_6 + \left(\frac{3}{2} + \frac{3}{2}x\right)O_2 \xrightarrow{k_3'} 3CO_x + 3H_2O \quad (C)$$

This does not take formation of any minor byproducts like ethene and acrolein into account; however, the total selectivity to these products was less than 0.5 % in all experiments. This leads to the following rate expressions

$$r_1 = k_1'[C_3H_8]^n[O_2]^m = k_1[C_3H_8] \quad (1)$$

$$r_2 = k_2'[C_3H_8]^n[O_2]^m = k_2[C_3H_8] \quad (2)$$

$$r_3 = k_3'[C_3H_6]^n[O_2]^m = k_3[C_3H_6] \quad (3)$$

Previous studies showed that the reaction order in oxygen was zero under oxidizing conditions, as long as the water concentration was low, and that the reaction order in propane was one [75]. For the propene combustion reaction, the reaction order in propene and oxygen was indirectly shown to be one and zero, respectively, by comparing simulated and experimental selectivity as function of conversion curves at different propene to oxygen ratios [89]. The plug flow reactor (PFR) design equations for the conversion of propane, the formation of propene and the formation of CO_x become:

$$F\frac{d[C_3H_8]}{dw} = -(r_1 + r_2) = -(k_1 + k_2)[C_3H_8] \quad (4)$$

$$F\frac{d[C_3H_6]}{dw} = r_1 - r_3 = k_1[C_3H_8] - k_3[C_3H_6] \quad (5)$$

$$F\frac{d[CO_x]}{dw} = 3(r_2 + r_3) = 3(k_2[C_3H_8] + k_3[C_3H_6]) \quad (6)$$

Where F is the volumetric flow of gas at the reaction temperature and pressure in cm^3/s, $[C_3H_8]$ and $[C_3H_6]$ the concentration of propane and propene in mol/cm^3 and w the mass of catalyst in g. The volume of the gas was assumed to be constant, which is reasonable since the worst case scenario of complete conversion of propane to CO will result in 12.5 % expansion. Keeping the conversion of propane lower than 40 % and assuming a mixture of the three main products is formed the expansion of the gas was estimated to be less than 3 %.

Solving eq. (4) by integrating over the whole catalyst mass lead to:

$$[C_3H_8] = [C_3H_8]_0 \, e^{-\frac{w}{F}(k_1+k_2)} \quad (7)$$

$$X = 1 - e^{-\frac{w}{F}(k_1+k_2)} \quad (8)$$

Here X is the fractional conversion of propane, w the total mass of catalyst in g and w/F the weight based contact time in $(g \cdot s)/cm^3$.

Inserting (7) into equations (5) and (6) and integrating over the whole catalyst mass lead to:

$$Y_{C_3H_6} = \frac{k_1}{k_3 - k_2 - k_1}\left(e^{-\frac{w}{F}(k_1+k_2)} - e^{-\frac{w}{F}k_3}\right) \quad (9)$$

$$Y_{CO_x} = \frac{(k_2 - k_3)e^{-\frac{w}{F}(k_1+k_2)} + k_1 e^{-\frac{w}{F}k_3} + k_3 - k_2 - k_1}{k_3 - k_2 - k_1} \quad (10)$$

Here $Y_{C_3H_6} = \frac{[C_3H_6]}{[C_3H_8]_0}$ is the carbon atom based fractional yield of propene and $Y_{CO_x} = \frac{[CO_x]}{3[C_3H_8]_0}$ is the carbon atom based fractional yield of CO_x. At each temperature, the sum of k_1 and k_2 was determined by fitting the experimental propane conversion to Equation (8). Then all three reaction rate constants were determined by fitting Equation (9) to the experimental propene yields with the $k_1 + k_2$ sum determined from the propane conversion as constraint in the fitting procedure. The apparent activation energy and the pre-exponential factors were demined from straight line fits to the logarithmic form of the Arrhenius equation $\ln(k_x) = \ln(k_{0,x}) - \frac{E_{a,x}}{R} \cdot \frac{1}{T}$. Fits were performed in the Origin Pro 8.1 software with user defined function files according to Equations (8) and (9).

Assuming the catalyst particles are spherical the Thiele modulus φ and effectiveness factor η are given as:

$$\varphi = R \cdot \sqrt{\frac{k \cdot \rho}{D_{eff}}}, \quad \eta = \frac{3}{\varphi}\left(\frac{1}{\tanh(\varphi)} - \frac{1}{\varphi}\right) \tag{11}$$

The effectiveness factor is larger than 0.99 for the particle radius R = 0.015 cm (the upper limit of the sieve fraction), rate constant k = 6.4 cm^3/(g·s) (the highest rate constant measured for the oxidative dehydrogenation of propane), catalyst density ρ = 2 g/cm^3 and a conservative estimate of the effective diffusivity D_{eff} = 0.02 cm^2/s. From this it is safe to assume that the measured reaction rates were only limited by the kinetics on the catalyst surface.

7.4 Results and discussion

7.4.1 Catalyst preparation and characterization

The catalyst preparation and the investigation of the structure of supported vanadia was discussed above (see Section 6.3). The results relevant for this study are summarized in Table 7.1. The products of the flame spray synthesis had high surface area and well dispersed vanadia. Only traces of crystalline vanadia were observed with XRD and Raman spectroscopy at the highest vanadium loading of 10 wt.% V. At 2 and 3 wt.% V mostly vanadia monomers were formed, at 5 wt.% V a mixture of monomers and oligomers were detected and at 7.5 and 10 wt.% V mostly oligomers were formed. This makes the series of FSP catalysts ideal for studying the catalytic activity and selectivity as function of the structure of the vanadia species on the surface.

Table 7.1: Overview of the VO_x/Al_2O_3 catalysts prepared by flame spray pyrolysis, specific surface area (SSA), BET equivalent particle diameter and apparent vanadium surface density.

Sample	SSA (m^2/g)[a]	d_p (nm)[b]	VO_x/nm^2,[c]	Vanadia phase[d]
2 wt.% V	166	9.2	1.4	Monomeric
3 wt.% V	169	9.0	2.1	Monomeric
5 wt.% V	168	9.1	3.6	Mixed
7.5 wt.% V	148	10.4	6.0	Oligomeric
10 wt.% V	143	10.9	8.4	Oligomeric

[a]6 point BET measurement, [b]calculated from the SSA assuming spherical particles, [c]calculated from the SSA and the vanadia loading, [d]determined by Raman and UV-vis spectroscopy

7.4.2 Catalytic activity and selectivity at high oxygen concentration

All the catalysts were investigated at high oxygen concentration with a gas composition of $C_3H_8/O_2/N_2$ = 5/25/70. The high oxygen concentration was chosen to keep the catalyst oxidized and avoid mass transfer limitations in oxygen. The amount of catalyst and the reaction temperature was optimized individually for each catalyst to achieve approximately 30 to 35 % propane conversion at the highest temperature and the longest con-

tact time. The experimental conditions are summarized in Table 7.2. The measured propane conversion at three different temperatures and the one parameter fits to Equation (8) for the 5 wt.% V catalyst are shown in Figure 7.1. The maximum propane conversion was 33 % at 444 °C. It was possible to fit the measured conversion to the model with high accuracy at all three temperatures. The measured propene yield and the three parameter fit to Equation (9), with the value of $k_1 + k_2$ determined from the fit to Equation (8) as constraint, are shown in Figure 7.2(a). Also for the propene yield it was possible to accurately fit the experimental data to the model at all three temperatures. At all three temperatures there was a maximum in the propene yield, which shifted to shorter contact time with increasing temperature. The rate constants determined for all five catalysts are summarized in Table 7.3. Using the three rate constants determined from the fit to Equation (9) the CO_x yield was calculated according to Equation (10) and compared to the experimental data, see Figure 7.2(b). The agreement between the experimental data and the predicted data was very good giving validity to the model since these data were not used in the fitting procedure.

Table 7.2: Variable conditions for the catalytic activity measurements. All experiments were performed with a gas mixture of C3H8/ O2/N2 = 5/25/70 and flows from 50 to 260 Nml/min.

Sample	m_{cat} (mg)	m_{SiC} (mg)	Temp. (°C)[a]	w/F (g·s/cm^3)[b]
2 wt.% V	150	350	460-500	0.0165-0.0721
3 wt.% V	100	400	440-480	0.0111-0.0490
5 wt.% V	75	450	390-430	0.0116-0.0527
7.5 wt.% V	75	450	360-400	0.0088-0.0414
10 wt.% V	75	450	360-400	0.0090-0.0417

[a]set point of the oven, three temperatures in steps of 20 °C were investigated, [b] weight based contact time at the measured reaction temperature and pressure.

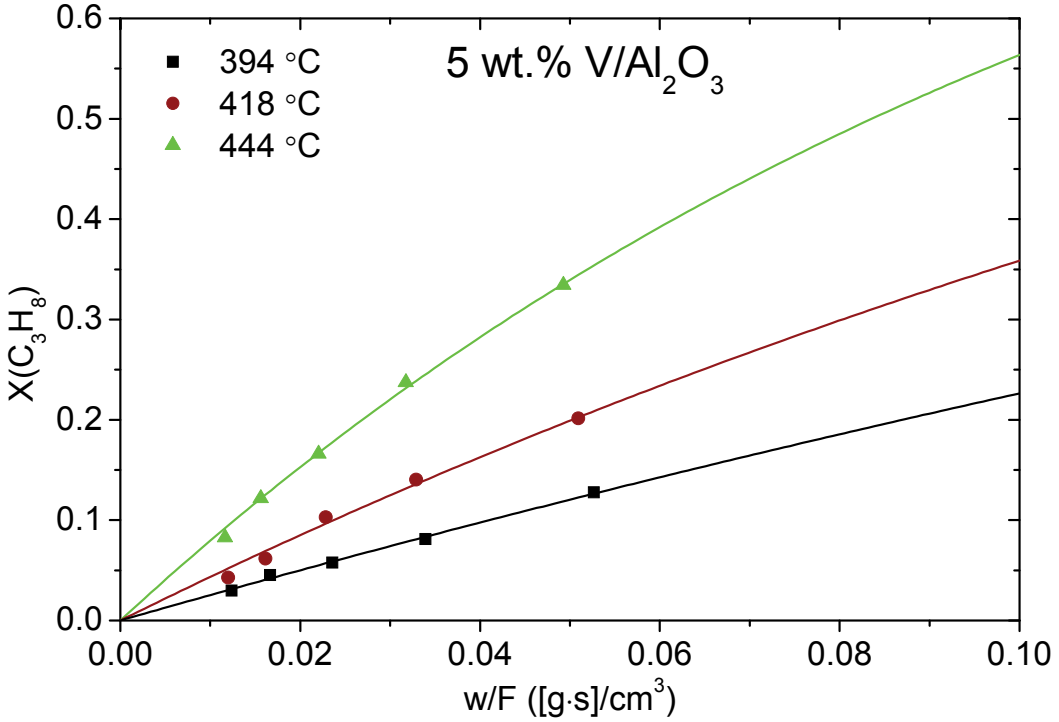

Figure 7.1: Measured propane conversion and fit to equation (8) for the 5 wt. % V catalyst. Temperatures were measured in the catalyst bed and the gas composition was $C_3H_8/O_2/N_2$ = 5/25/70.

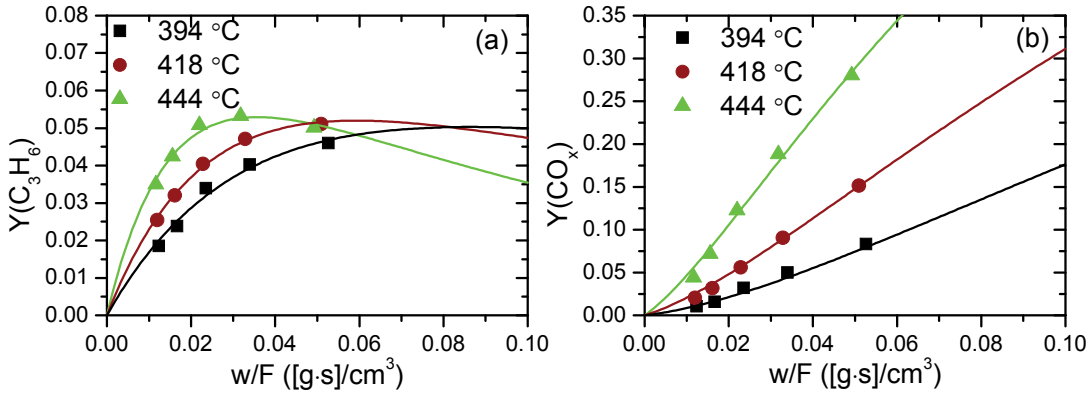

Figure 7.2: (a) Measured propene yield and fit to equation (9) using the value of k_1+k_2 determined from Figure 7.1 as fitting constraint. (b) Measured CO_x yield and results of equation (10) using the three rate constants determined from the fit to equation (9) for the 5 wt. % V catalyst. Temperatures were measured in the catalyst bed and the gas composition was $C_3H_8/O_2/N_2$ = 5/25/70.

Table 7.3: Fitted first order rate constants for the oxidative dehydrogenation (k_1), the combustion of propane (k_2) and the combustion of propene (k_3) for the five vanadia on alumina catalysts at the experimental conditions summarized in Table 7.2.

Sample	Temp. (°C)[a]	k_1 ($cm^3/(g \cdot s)$)	k_2 ($cm^3/(g \cdot s)$)	k_3 ($cm^3/(g \cdot s)$)
2 wt.% V	462	1.9	0.3	11.7
	483	2.8	1.1	14.7
	505	4.5	1.6	21.0
3 wt.% V	444	2.9	0.4	21.3
	466	4.2	1.4	26.1
	488	6.4	2.5	35.9
5 wt.% V	395	2.0	0.6	31.7
	418	2.9	1.6	42.6
	444	4.7	3.6	66.5
7.5 wt.% V	362	1.5	0.8	72.3
	386	2.4	1.7	106.7
	410	3.9	4.5	162.9
10 wt.% V	364	1.3	0.9	72.6
	387	2.0	1.3	103.5
	414	3.1	3.7	150.8

[a]Measured in the catalyst bed.

Arrhenius plots of the rate constants with straight line fits are shown in Figure 7.3. The apparent activation energy and the pre-exponential factor for all three reactions and all the catalysts are summarized in Table 7.4. It is seen from these data that the higher the vanadia loading, the higher the reaction rate for both ODP and the combustion reactions. The trend in activation energy was $E_{a,2} > E_{a,1} > E_{a,3}$, in good agreement with other studies [75]. The decrease in activation energy with increasing vanadia loading was particularly significant for the direct combustion of propane, which decreased from 180 to 104 kJ/mol when the vanadium loading increased from 3 to 10 wt. %. Comparing the relative rate constants k_2/k_1 and k_3/k_1, which both should be minimized in order to optimize the propene yield, the high loaded 7.5 and 10 wt.% V catalysts have much higher ratios than the low loaded 2 and 3 wt.% V catalysts in the relevant temperature range (see Figure 7.4). The 5 wt.% V catalyst is intermediate between the low and high loaded catalyst. This will result in much lower propene yield for the high loaded catalysts con-

taining mostly vanadia oligomers, thus vanadia monomers are favorable for high selectivity. Particularly the ratio between the competing ODP and propane combustion reactions (k_2/k_1) should be much smaller than 1 in order to achieve good selectivity, but for the high loaded catalysts it is larger than 1 above 410 °C. Unfortunately, Figure 7.4 further demonstrates that the ratio of the rate constants have opposite trends with respect to temperature indicating that it will be difficult to obtain a high yield of propene.

It was previously observed that lower UV-vis absorption edge energy results in higher ODP rates [138], which is consistent with the high loaded catalysts having the highest activity and the lowest UV-vis absorption edge energy (see Section 6.3.4).

Table 7.4: Pre-exponential factors and apparent activation energies determined from straight line fits to Arrhenius plots of the first order rate constants from Table 7.3.

Sample	**$k_{0,1}$ (cm^3/(g·s))**	**$E_{a,1}$ (kJ/mol)**	**$k_{0,2}$ (cm^3/(g·s))**	**$E_{a,2}$ (kJ/mol)**	**$k_{0,3}$ (cm^3/(g·s))**	**$E_{a,3}$ (kJ/mol)**
2 wt.% V	$1.11 \cdot 10^7$	95.4	$3.51 \cdot 10^{11}$	168.3	$4.52 \cdot 10^5$	64.7
3 wt.% V	$1.85 \cdot 10^6$	79.7	$5.96 \cdot 10^{12}$	179.8	$1.59 \cdot 10^5$	53.3
5 wt.% V	$7.64 \cdot 10^5$	71.6	$3.08 \cdot 10^{11}$	149.8	$1.85 \cdot 10^6$	61.1
7.5 wt.% V	$1.52 \cdot 10^6$	73.2	$2.83 \cdot 10^{10}$	128.4	$7.17 \cdot 10^6$	60.8
10 wt.% V	$2.41 \cdot 10^5$	64.3	$2.55 \cdot 10^8$	103.8	$1.60 \cdot 10^6$	53.0

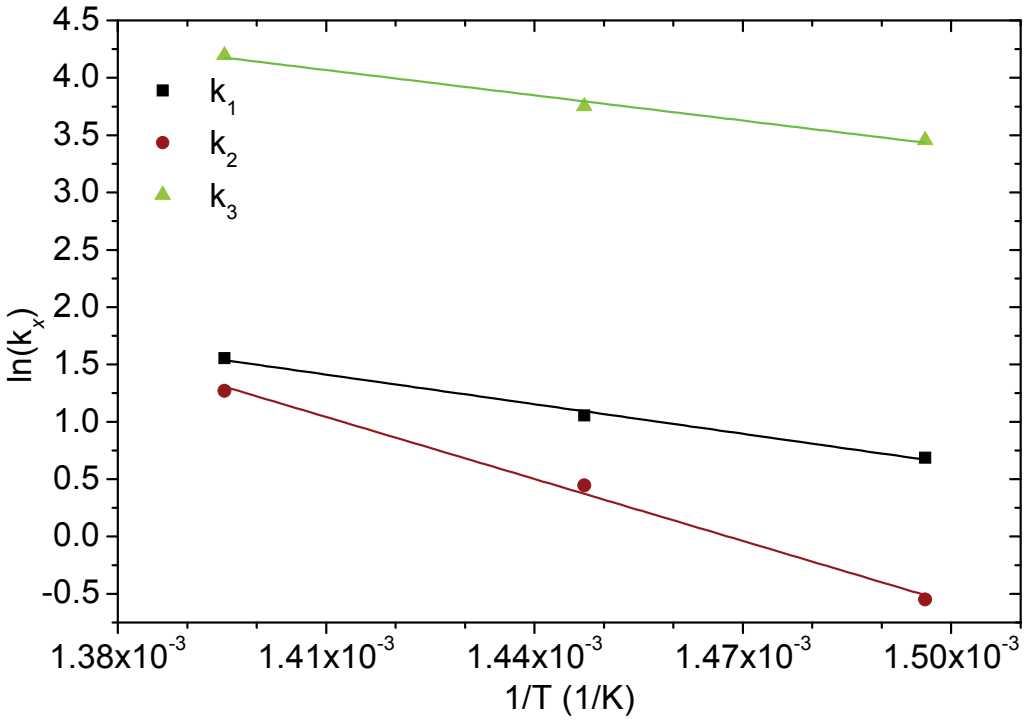

Figure 7.3: Arrhenius plots with straight line fits of the reaction rate constants as determined from the fit to equation (9) (see Figure 7.2) for the 5 wt. % V catalyst. Temperatures were measured in the catalyst bed and the gas composition was $C_3H_8/O_2/N_2 = 5/25/70$.

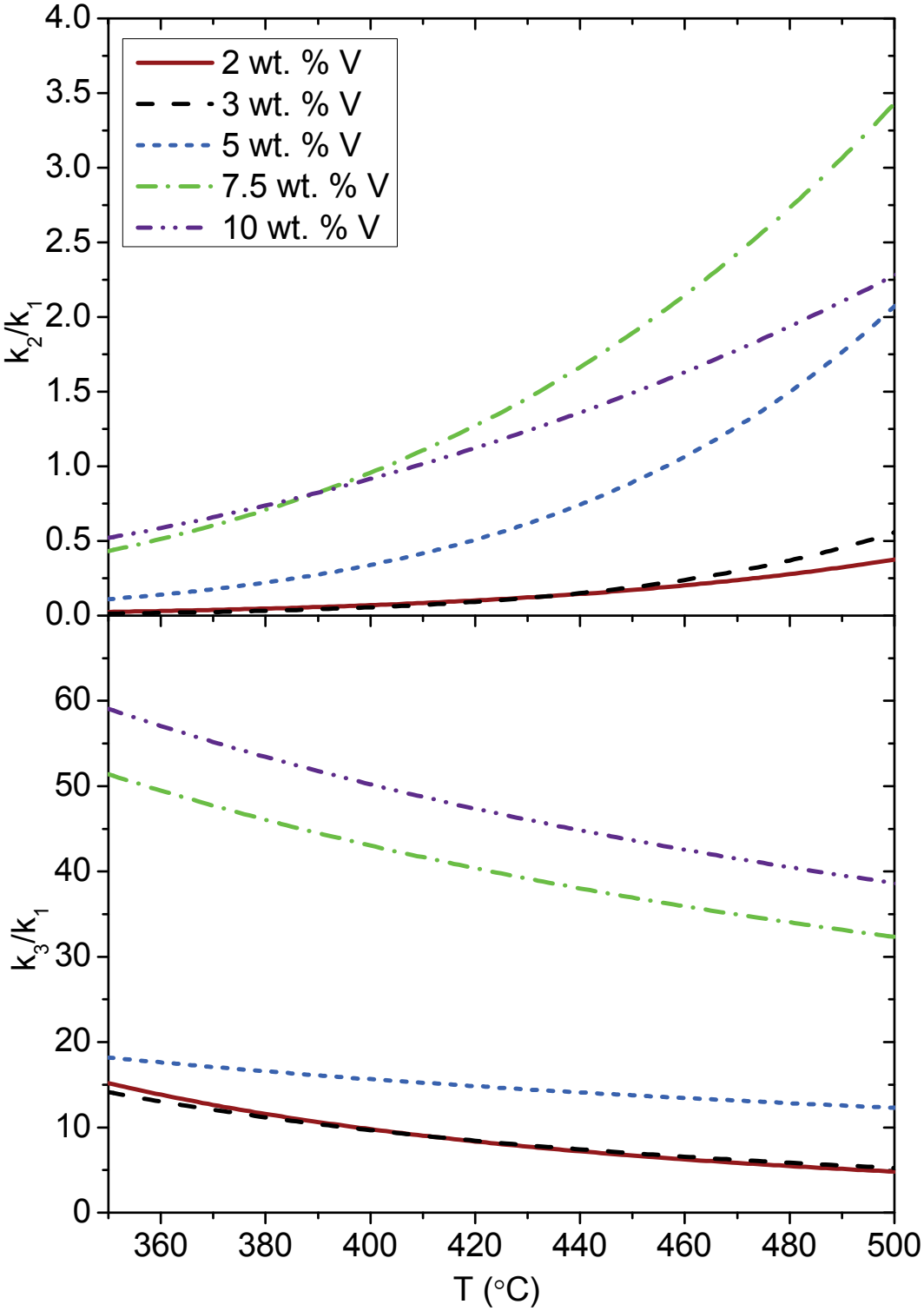

Figure 7.4: Calculated relative reaction rate constants for the propane combustion relative to ODP (top) and propene combustion relative to ODP (bottom) based on the kinetic parameters from Table 7.4.

The observations qualitatively agree with DFT calculations on the ODP mechanism that the activity was higher when neighboring vanadyl sites can participate in the reaction, as for the 7.5 and 10 wt.% V catalyst containing mainly vanadia oligomers [79]. Also the oligomeric vanadia sites favored formation of electrophilic oxygen species (like peroxovanadates), which were highly active in complete hydrocarbon oxidation, since the 7.5 and 10 wt.% V catalysts were much more active in both propane and propene combustion compared to the 2 and 3 wt.% V catalysts [83,88]. The ODP activation energy determined for the 2 wt.% catalyst (representing vanadia monomers) of 95 kJ/mol was somewhat lower than the DFT prediction of 123 kJ/mol, however, the calculations were performed for silica supported vanadia which is less active than alumina supported vanadia [77]. The ODP activation energy for alumina supported vanadia determined by Dinse et al. [77] was 113 kJ/mol for a 1.2 wt.% V catalyst and that determined by Argyle et al. [91] was around 110 to 120 kJ/mol over a range of loadings, which is somewhat higher than that determined in this study. The propane combustion activation energy for vanadia monomers (2 and 3 wt.% V) of 168 to 180 kJ/mol was significantly higher that reported by Argyle et al. of around 120 kJ/mol and for vanadia oligomers (7.5 and 10 wt.% V) it was 104 to 128 kJ/mol, similar to that reported by Argyle et al. [91].

The propene yield was calculated as function of the temperature and weight based contact time using the determined activation energies and pre-exponential factors (Equation (9)). For the 5 wt.% V catalyst the maximum propene yield was 5.3 % at a temperature of 455 °C and contact time of 0.030 g·s/cm^3 (see Figure 7.5). There was a rather large area on the contour plot stretching from short contact time at high temperature to long contact time at low temperature where the propene yield was close to the maximum val-

ue (see Figure 7.5). Moving away from this optimal region the propene yield decreased steeply with change in temperature or contact time, either due to propane and propene combustion at high temperature, propene combustion at low temperature and long contact time or too low ODP rate at low temperature and short contact time. Note that at temperatures above 500 °C homogeneous propane combustion becomes significant, which will decrease the yield, but temperatures up to 550 °C was included to better show the results of the model.

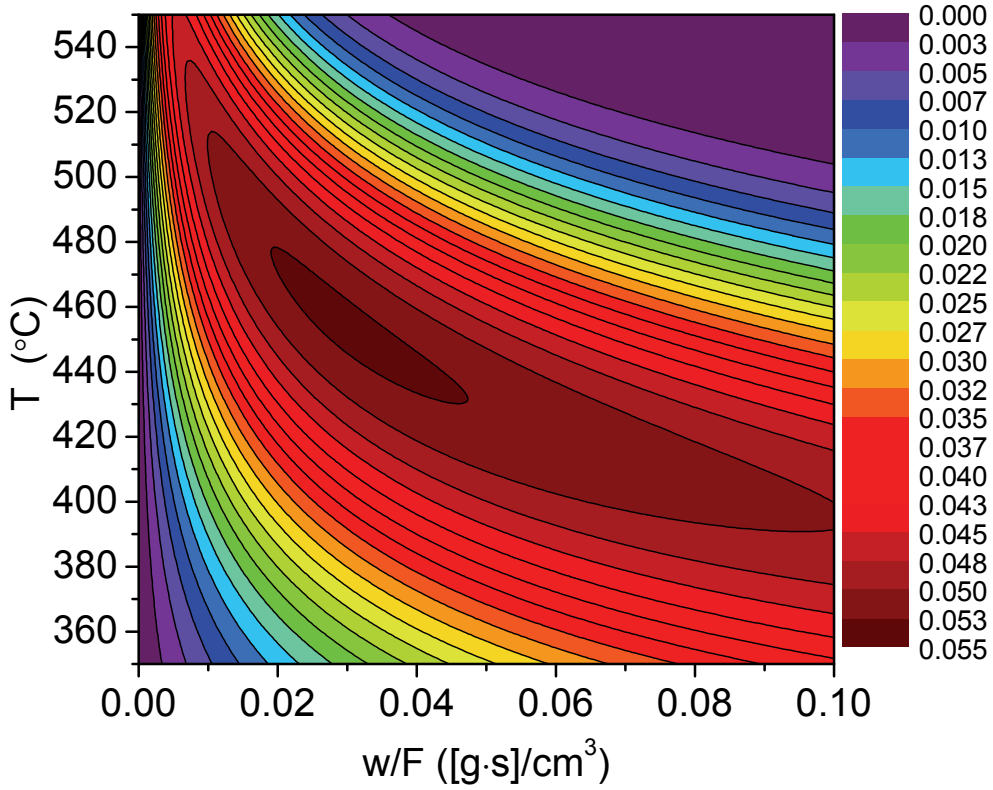

Figure 7.5: Predicted propene yield for the 5 wt.% V catalyst as function of the weight based contact time and the catalyst bed temperature based on activation energies and the pre-exponential factors from Figure 7.3. Temperatures above 500 °C were only included to clearly show the global maximum, since homogeneous propane combustion not included in the model would be significant, resulting in even lower propene yield.

7.4.3 Model validation by shifting temperature and contact time

To investigate the predictive capabilities of the model, catalytic activity over the 7.5 wt.% V catalyst was investigated using 15 mg of catalyst and temperatures from 446 to 508 °C, compared to 75 mg of catalyst and temperatures from 362 to 410 °C in the initial experiment. The measured propane conversion was compared with that predicted by the kinetic parameters extracted from the initial experiment showing reasonably good agreement (see Figure 7.6(a)), although the error increased with increasing temperature. Also in terms of propene yield and selectivity as function of conversion the experimental results showed good agreement with the model predictions (see Figure 7.6(b) and Figure 7.7). This showed that the model can be used to predict the propene yield when changing the temperature and contact time.

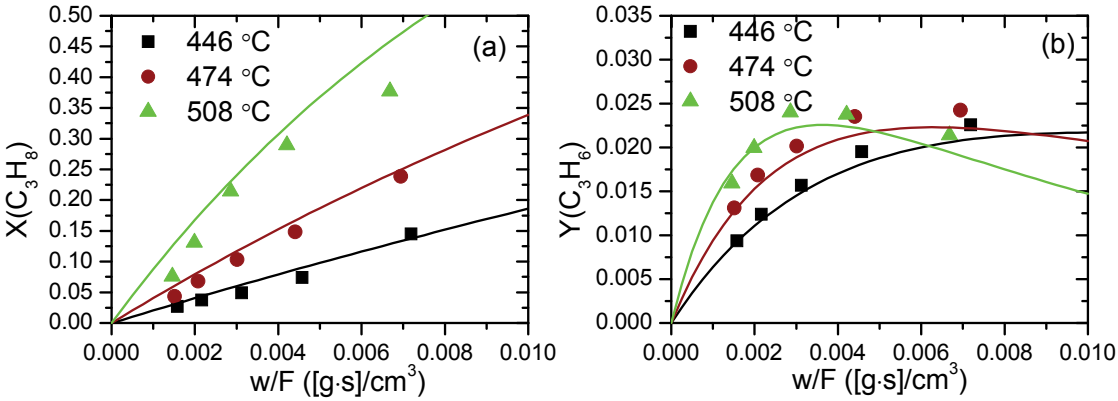

Figure 7.6: (a) Measured and predicted propane conversion and (b) measured and predicted propene yield of the 7.5 wt.% V catalyst. The measured values are from an experiment using 15 mg catalyst and the indicated catalyst bed temperatures and gas composition $C_3H_8/O_2/N_2$ = 5/25/70. The predicted values were calculated by equation (8) and (9) using the kinetic parameters from Table 7.4 for the 7.5 wt.% V catalyst (which are based on an experiment with 75 mg of catalyst and temperatures from 362 to 410 °C and gas composition $C_3H_8/O_2/N_2$ = 5/25/70) and the contact times and the bed temperatures in the 15 mg experiment.

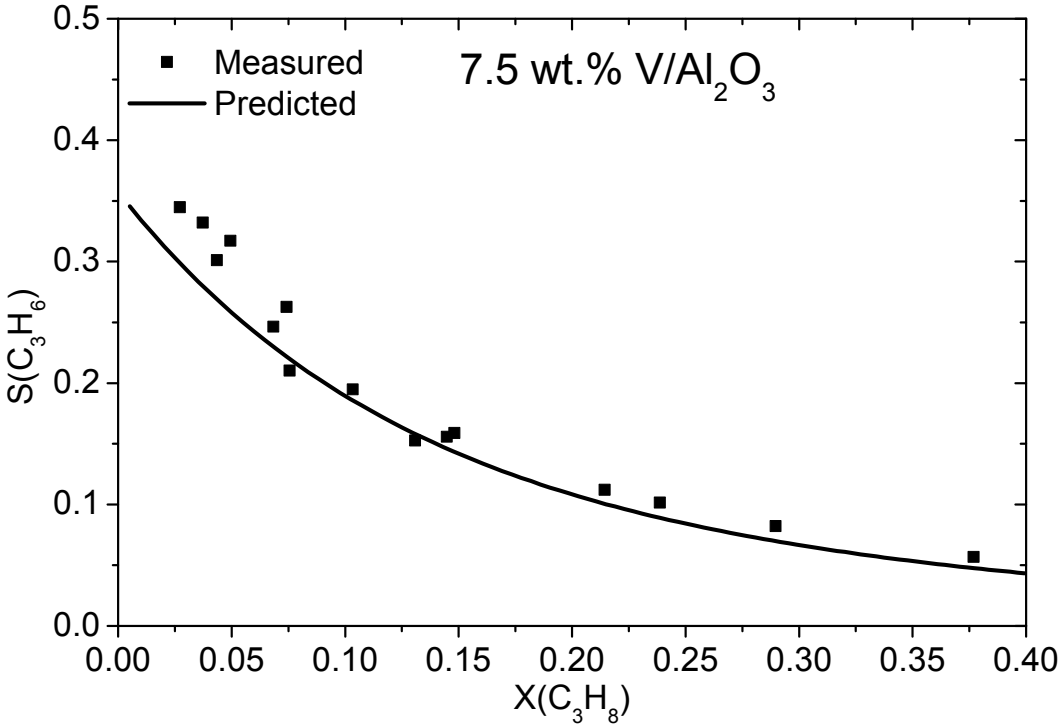

Figure 7.7: Predicted and measured propene selectivity as function of propane conversion for the 7.5 wt. % V catalyst. The measured values are from an experiment using 15 mg catalyst and the predicted values were calculated with the kinetic parameters from Table 7.4 for the 7.5 wt.% V catalyst like in Figure 7.6.

7.4.4 Model validation by direct propene combustion

In order to investigate whether the propene combustion kinetics included in the ODP model was valid, direct propene oxidation experiments were performed using the 5 wt.% V catalyst. In order to have similar conditions as in the ODP experiments the gas composition was $C_3H_6/O_2/N_2$ = 1/25/74 with total gas flow of 180 and 260 Nml/min. The temperature was 344 to 419 °C as measured in the catalyst bed. The propene conversion was between 5 and 35 % and the main products of the combustion were CO and CO_2. The selectivity to acrolein was between 5 and 10 %, decreasing with increasing propene conversion, and only traces of acetaldehyde and ethene were observed. The measured conversion was compared to that predicted by the kinetic model (see Figure

7.8). At 392 and 419 °C there is good agreement between the model and the experiment, while at 344 °C the measured conversion is 40 and 45 % lower than the predicted conversion at 180 and 260 Nml/min respectively. This temperature is also more than 50 °C lower than in the experiment the model was based on. This indicates that both the activation energy and the pre-exponential factor for direct propene combustion is somewhat underestimated by the ODP model, while still on the correct order of magnitude. The reason may be the higher propene concentration in the combustion experiment compared to the ODP experiment, which may result in occupation of active sites at low temperature leading to lower conversion or possibly slower re-oxidation of the catalyst by gas phase oxygen at low temperature.

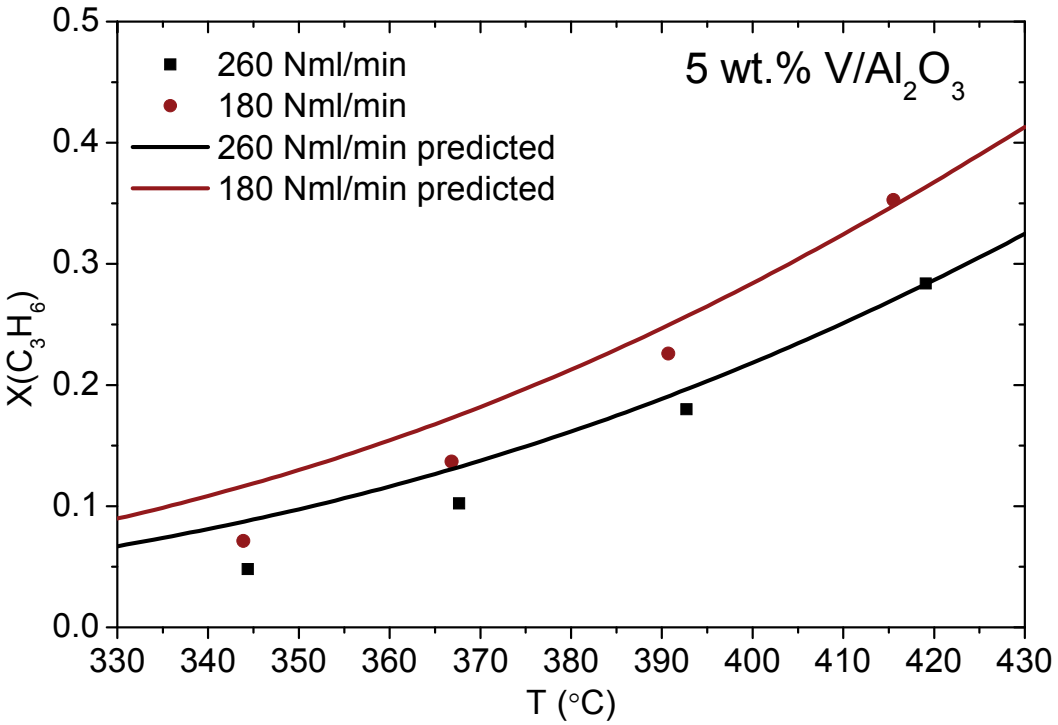

Figure 7.8: Measured and predicted propene conversion in direct propene oxidation as a function of the temperature measured in the catalyst bed using the gas composition $C_3H_6/O_2/N_2$ = 1/25/74.

7.4.5 Catalytic activity and selectivity at low oxygen concentration

Using in-situ X-ray absorption spectroscopy it was observed for the 7.5 wt.% V catalyst that vanadia was partly reduced at temperatures above 460 °C when the oxygen concentration was less than approximately 1 vol. % (see Section 6.3.5). To investigate the effect of this reduction on activity and selectivity, experiments were performed with gas composition of $C_3H_8/O_2/N_2$ = 5/10/85, 5/5/90, 5/3/92 and 5/2/93 at temperatures of 460 and 480 °C (furnace set points). During in-situ XANES experiments the 7.5 wt.% V catalyst was partly reduced to $V^{3+/4+}$ at these temperatures (see Section 6.3.5). The measured propane conversion was arround the value predicted by the kinetic model at 10 % O_2 in the inlet gas, but with decreasing oxygen concentration the difference between the measured and predicted propane conversion increased (see Figure 7.9). This was particular significant at 480 °C. The apparently decreased catalytic activity indicated that the vanadia is in reduced form, due to slow re-oxidation of the catalyst. When comparing the measured propene selectivity as function of conversion at low oxygen concentration there is a significant increase in selectivity compared to the model prediction (see Figure 7.10). The predicted selectivity as function of conversion is close to the measured values at 25 % O_2 in the gas, since these data are the basis of the model. The selectivity increase was most significant at 480 °C where the propene selectivity was around 36 % at 9 % propane conversion with 2 % O_2 in the inlet, compared to around 20 % propene selectivity at 9 % propane conversion with 25 % O_2 in the inlet. The decrease in the catalytic activity with reduction of vanadia could be the result of decreased surface concentration of nucleophilic oxygen ($O=V^{5+}$ vanadyl sites) responsible for C-H bond cleavage in ODP and the improved selectivity could be a result of decreased surface concentration of electrophilic oxygen species (like peroxovanadates), which would

otherwise lead to total combustion of adsorbed hydrocarbon intermediates [79,83,88]. After the low oxygen concentration experiments the same sample was re-oxidized in dry air. Thereby the original activity and selectivity was regained, showing that the reduction for the flame-derived catalysts is reversible.

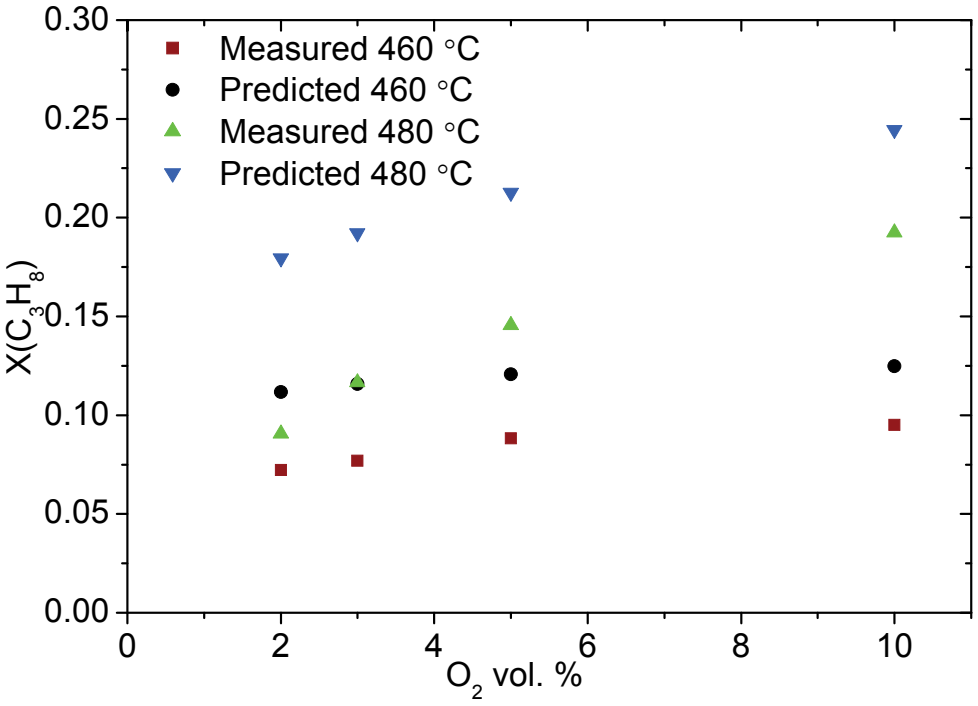

Figure 7.9: Measured propane conversion as function of oxygen vol. % in the inlet gas (gas composition $C_3H_8/O_2/N_2 = 5/x/95-x$) and the predicted propane conversions based on the kinetic parameters in Table 7.4 for the 7.5 wt.% V catalyst and temperatures measured in the catalyst bed. Legend temperatures were the furnace set points.

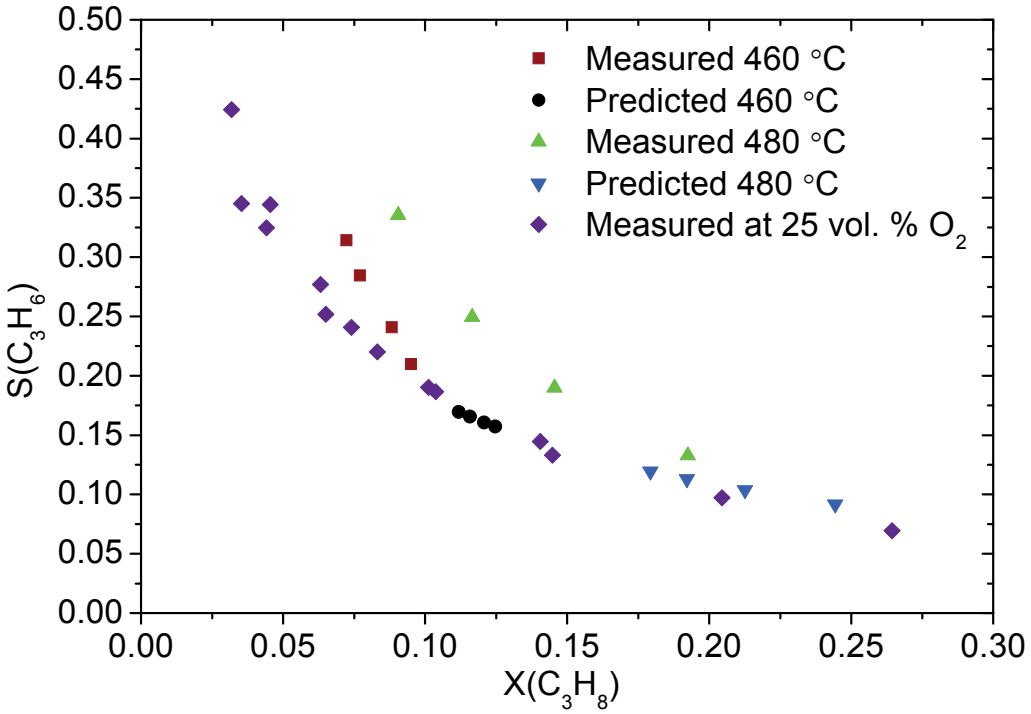

Figure 7.10: Measured and predicted propene selectivities as function of conversion. The predicted values were calculated from the kinetic parameters in Table 7.4 for the 7.5 wt.% V catalyst and temperatures measured in the catalyst bed. Better selectivity but significantly lower conversion was achieved when reducing the oxygen inlet concentration. Temperatures in the legend were the furnace set points and the gas composition was $C_3H_8/O_2/N_2 = 5/x/95-x$ (see Figure 7.9).

7.5 Conclusions

A kinetic model for oxidative dehydrogenation of propane (ODP) consisting of the dehydrogenation reaction, parallel combustion of propane and sequential combustion of propene was derived and applied to experimental data. The model fitted very well to the experimental results of yield and conversion obtained in lab-scale ODP experiments using alumina supported vanadia catalysts prepared by flame spray pyrolysis. The model was validated by comparing it to experimental ODP data at different temperatures and contact times as well as separate experiments of the direct combustion of propene. The activation energy for the parallel combustion of propane decreased significantly with

increased vanadia loading, resulting in significantly lower propene selectivity when using vanadia catalysts containing mainly vanadia oligomers. This was due to formation of electrophilic oxygen species, highly active in complete hydrocarbon oxidation, on the surface of vanadia oligomers. Calculations of the propene yield as function of both temperature and contact time showed that there is an optimum operating window, outside of which the propene and propane combustion rates are too high or the OPD rate too low.

Performing catalytic activity measurements at low oxygen concentration resulted in lower activity but higher propene selectivity compared to the predictions of the kinetic model and experimental data at high oxygen concentration. This may be the result of reduced surface concentration of both selective nucleophilic and unselective electrophilic oxygen species.

8. Oxidative dehydrogenation over supported molybdenum and molybdenum-vanadium oxide catalysts.

8.1 Introduction

Besides vanadia based catalysts, also molybdenum oxide is interesting for oxidative dehydrogenation of propane. To this purpose alumina supported molybdenum oxide and mixed molybdenum-vanadium oxide were prepared by FSP, structurally characterized and evaluated as catalysts for the ODP reaction in comparison to the vanadia based catalysts (see Sections 6 and 7).

8.2 Experimental

8.2.1 Catalyst preparation

Aluminium(III)acetylacetonate (Sigma Aldrich), molybdenum(VI)2-ethylhexanoate (Strem Chemicals) and vanadium(III)acetylacetonate (Sigma Aldrich) were dissolved in anhydrous toluene (Sigma Aldrich) to a total metal concentration of 0.4 M in ratios for preparation of 1,2, 5, 7, 10 and 15 wt.% Mo and 2 wt.% V with 4, 7, 10 and 15 wt.% Mo on alumina, assuming the products are MoO_3, V_2O_5 and Al_2O_3 (see Table 8.1). After stirring and gentle heating to around 50 °C clear, dark purple solutions were obtained. The precursor solutions were sprayed at 5 ml/min with 5 Nl/min O_2 as dispersion gas at 1.8 bar pressure drop. The supporting flame was maintained at 1 Nl/min CH_4 and 3 Nl/min O_2. Details of FSP experimental are found in Section 2.

8.2.2 Catalyst characterization

Details on specific surface area, XRD, Raman and UV-vis measurements are found in Section 6.2.2.

Table 8.1: Overview of the Mo/Al_2O_3 and MoV/Al_2O_3catalysts prepared by flame spray pyrolysis, specific surface area, BET equivalent particle diameter and apparent molybdenum and vanadium surface densities.

Sample	Mo wt.%	V wt.%	SSA (m^2/g)[a]	d_p (nm)[b]	MoO_x/nm^2, [c]	VO_x/nm^2, [c]
1Mo	1	-	160	9.4	0.4	-
2Mo	2	-	156	9.6	0.8	-
5Mo	5	-	166	9.0	1.9	-
7Mo	7	-	164	9.0	2.7	-
10Mo	10	-	152	9.7	4.2	-
15Mo	15	-	137	10.6	6.9	-
4Mo2V	4	2	157	9.6	1.6	1.5
7Mo2V	7	2	145	10.3	3.1	1.7
10Mo2V	10	2	123	11.9	5.1	1.9
15Mo2V	15	2	122	11.9	7.7	1.9

[a]6 point BET measurement, [b]calculated from the SSA assuming spherical particles, [c]calculated from the SSA and the molybdenum and vanadium loading.

8.2.3 Catalytic activity and selectivity

The FSP powder was pressed and crushed to 150 to 300 µm sized particles and diluted with SiC (also 150 to 300 µm). The amounts of catalyst and SiC depended on the transition metal loading (see Table 8.2). The catalysts were pre-oxidized in dry air at 550 °C before cooling down to the lowest reaction temperature and introducing the ODP reaction gas with a fixed composition of $C_3H_8/O_2/N_2$ = 5/25/70, flows of 50, 80, 100, 150 and 200 Nml/min and furnace temperatures of 460, 480 and 500 °C. The vanadia containing catalysts were generally much more active than only molybdenum oxide catalysts, so between 200 to 500 mg of catalyst was used for the Mo series and 75 mg of catalyst was used for the Mo+V series. Calculations of internal standard correction, conversion, yield and selectivity were done as for the vanadia catalysts (Section 6.2.3), details of the activity test setup are given in Section 2.2 and the kinetic model was applied as for the vanadia catalysts (Section 7).

Table 8.2: Conditions for the catalytic activity measurements. All experiments were performed with a gas mixture of 25 % O_2/5 % C_3H_8/N_2, flows from 50 to 200 Nml/min and temperatures 460, 480 and 500 °C as furnace set-point.

Sample	m_{cat} (mg)	m_{SiC} (mg)	w/F (g·s/cm^3)[a]
1Mo	500	300	0.072-0.241
2Mo	500	300	0.074-0.246
5Mo	400	300	0.057-0.196
7Mo	265	300	0.039-0.131
10Mo	300	300	0.040-0.144
15Mo	200	300	0.027-0.094
4Mo2V	75	450	0.0095-0.035
7Mo2V	75	450	0.0095-0.035
10Mo2V	75	450	0.0096-0.036
15Mo2V	75	450	0.0094-0.035

[a] weight over flow range at the measured reaction temperature and pressure.

8.3 Results and discussion

8.3.1 Catalyst preparation, surface area and metal surface density

The products of FSP synthesis were powders with very low density due to high interparticle porosity. Two series of catalyst were prepared, one series with only molybdenum oxide on alumina with loadings from 1 to 15 wt.% Mo and one series with mixed vanadium-molybdenum oxide on alumina with constant 2 wt.% V and 4 to 15 wt.% Mo (see Table 8.1). The fixed vanadium loading of 2 wt.% was chosen since when preparing only vanadia on alumina, 2 wt.% V resulted in supported vandia monomers with high selectivity for propene (see Section 6). The specific surface area generally decreased with increasing transition metal loading, where the Mo series ranged from 137 to 166 m^2/g, resulting in apparent molybdenum surface densities from 0.4 to 6.9 MoO_x/nm^2. This is from far below the theoretical monolayer density to above the monolayer density at approximately 5 MoO_x/nm^2 [139]. The Mo+V series ranged from 122 to 157 m^2/g resulting in apparent molybdenum surface densities from 1.6 to 7.7 MoO_x/nm^2 and vanadium

surface densities from 1.5 to 1.9 VO_x/nm^2, which is below the theoretical monolayer coverage of vanadia monomers of approximately 2.3 to 2.5 VO_x/nm^2 [34,67].

8.3.2 Powder X-ray diffraction

X-ray diffraction showed that the main crystalline phase of the FSP product was γ-Al_2O_3, with traces of crystalline MoO_3 observed as a very broad reflection around 2θ = 27° at 15 wt.% Mo and at 15 wt.% Mo+2 wt.%V where several reflections from MoO_3 were clearly observed (see Figure 8.1). This indicated that molybdenum and vanadium oxides were well dispersed on the surface of the of the alumina nanoparticles, when the molybdenum loading was below the theoretical monolayer around 5 MoO_x/nm^2. This is in agreement with studies of molybdenum oxide supported on silica-alumina mixtures prepared by FSP [113].

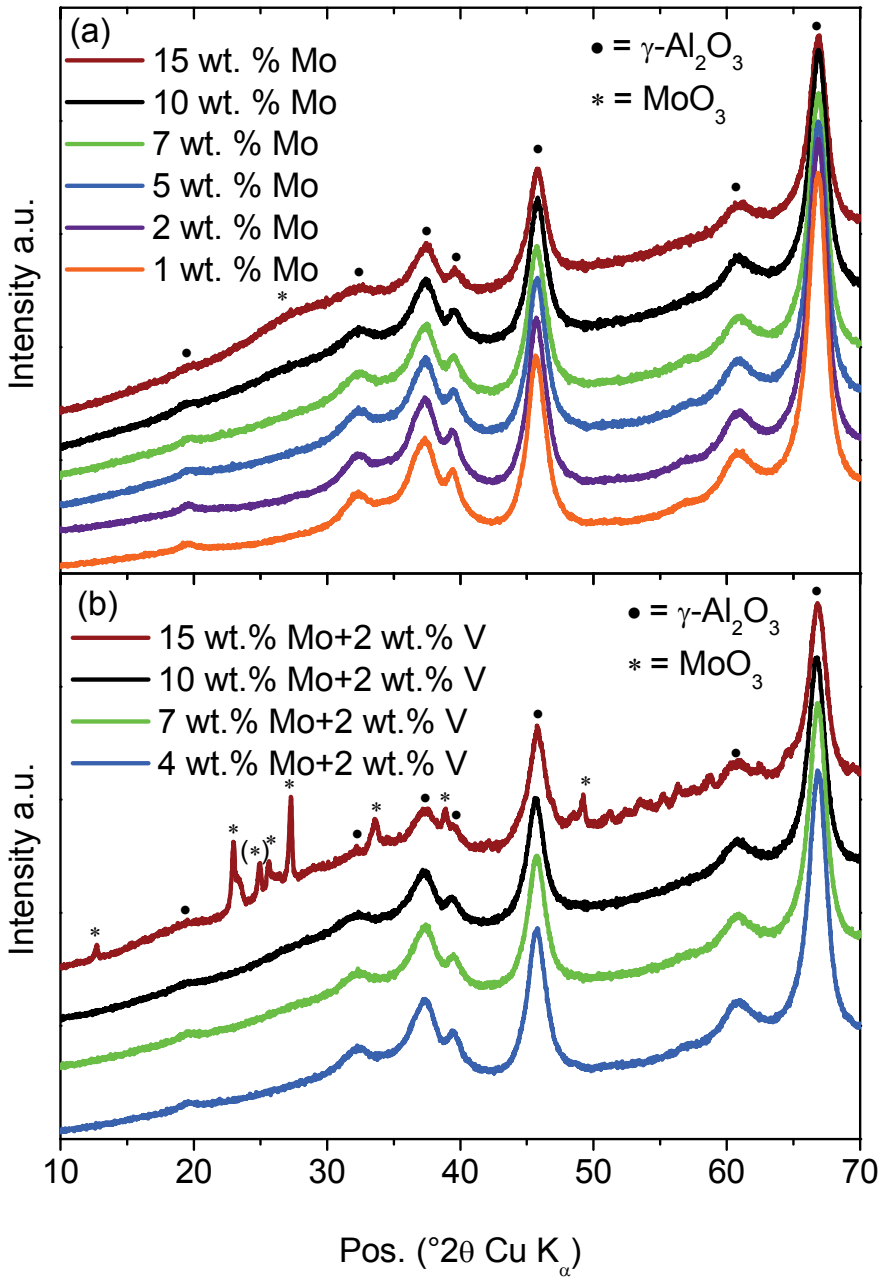

Figure 8.1: X-ray diffractograms of the molybdenum oxide series (a) and the mixed molybdenum-vanadium oxide series (b) showing mainly the reflection of γ-Al_2O_3. At 15 wt.% Mo weak indications of crystalline MoO_3 is marked with an * at 2θ = 27° and at 15 wt.% Mo + 2 wt.% V the reflections of α-MoO_3 are clearly observed along with a single reflection possibly from β-MoO_3 marked with (*).

8.3.3 Raman spectroscopy

Laser Raman spectra were recorded of the 10 and 15 wt.% Mo samples at room temperature, after dehydration at 550 °C in a flow of dry air (see Figure 8.2a). For the 10 wt.% Mo/alumina sample only supported molybdenum oxide species were observed by an intense peak at 1004 cm^{-1} assigned to molybdenyl stretching (Mo=O), consistent with other investigations of supported molybdenum oxide [69,113]. For the 15 wt.% sample a weak and broad peak was observed around 820 cm^{-1}, which could be assigned to crystalline MoO_3. This is in agreement with the XRD results that showed traces of MoO_3 for this sample (see Figure 8.1a) and that the apparent MoO_x surface density of 6.9 MoO_x/nm^2 is above monolayer coverage of approximately 5 MoO_x/nm^2. Compared to alumina supported molybdenum oxide prepared by incipient wetness impregnation the amount of crystalline MoO_3 formed after FSP synthesis was low, since at a surface density of 4.3 MoO_x/nm^2 (10 wt.% Mo) no crystalline MoO_3 was observed in this study, while significant amounts were observed by Chen et al. at 4.5 MoO_x/nm^2 [69]. For silica-alumina (30 wt.% SiO_2 and 70 wt.% Al_2O_3) supported molybdenum oxide prepared by FSP, traces of crystalline MoO_3 were observed at 1.5 MoO_x/nm^2 and above, which is likely to be an effect of the different support material [113]. This study also showed that Raman is not suited for distinguishing between monomeric and di- or oligomeric supported molybdenum oxide since the molybdenyl (Mo=O) stretching bands overlap and the Mo-O-Mo vibrations have too low Raman scattering cross section to be clearly observed. This was instead done by time of flight-secondary ion mass spectrometry (ToF-SIMS), where dimeric and trimeric molybdenum oxide clusters were clearly observed at 0.8 MoO_x/nm^2 and above.

The Raman spectra of the vanadium-molybdenum oxide catalysts recorded at similar conditions also showed the molybdenyl (Mo=O) stretching band at 1004 cm^{-1}, along with a vanadyl stretching band at 1030 cm^{-1} (see Figure 8.2b). This is consistent with other Raman investigations of alumina supported mixed vanadium-molybdenum oxide [71-73]. The vanadyl stretching band was clearly observed at 4 and 7 wt.% Mo + 2 wt.% V. Increasing the molybdenum loading to 10 and 15 wt.% resulted in the vanadyl band being reduced to a high energy shoulder to the molybdenyl band. At 15 wt.% Mo+2 wt.% V crystalline MoO_3 was clearly observed by the band around 820 cm^{-1}, while crystalline V_2O_5 was not observed, consistent with the XRD results (see Figure 8.1b).

Comparing the Raman spectrum of the 4 wt.% Mo+2wt.% V sample with the Raman spectra of the 10 wt.% Mo sample and a sample containing only 2 wt.% V, which contained mainly vanadia monomers (see Section 6.3.3), it is clear that the mixed oxide sample contained a mixture of supported MoO_x and VO_x monomers (see Figure 8.3a).

Crystalline MoO_3 was clearly observed by XRD for the 15 wt.% Mo+2wt.% V sample (see Figure 8.1b). This was also observed by Raman spectroscopy before dehydration. During the dehydration step this crystalline material spreads over the surface of the alumina, forming supported MoO_x, leaving only a minor fraction as crystalline MoO_3 (see Figure 8.3b). This thermal spreading phenomenon is well known and can be explained by the decreased surface free energy of an alumina supported MoO_x monolayer compared to separate nanoparticles of Al_2O_3 and MoO_3 [140-141].

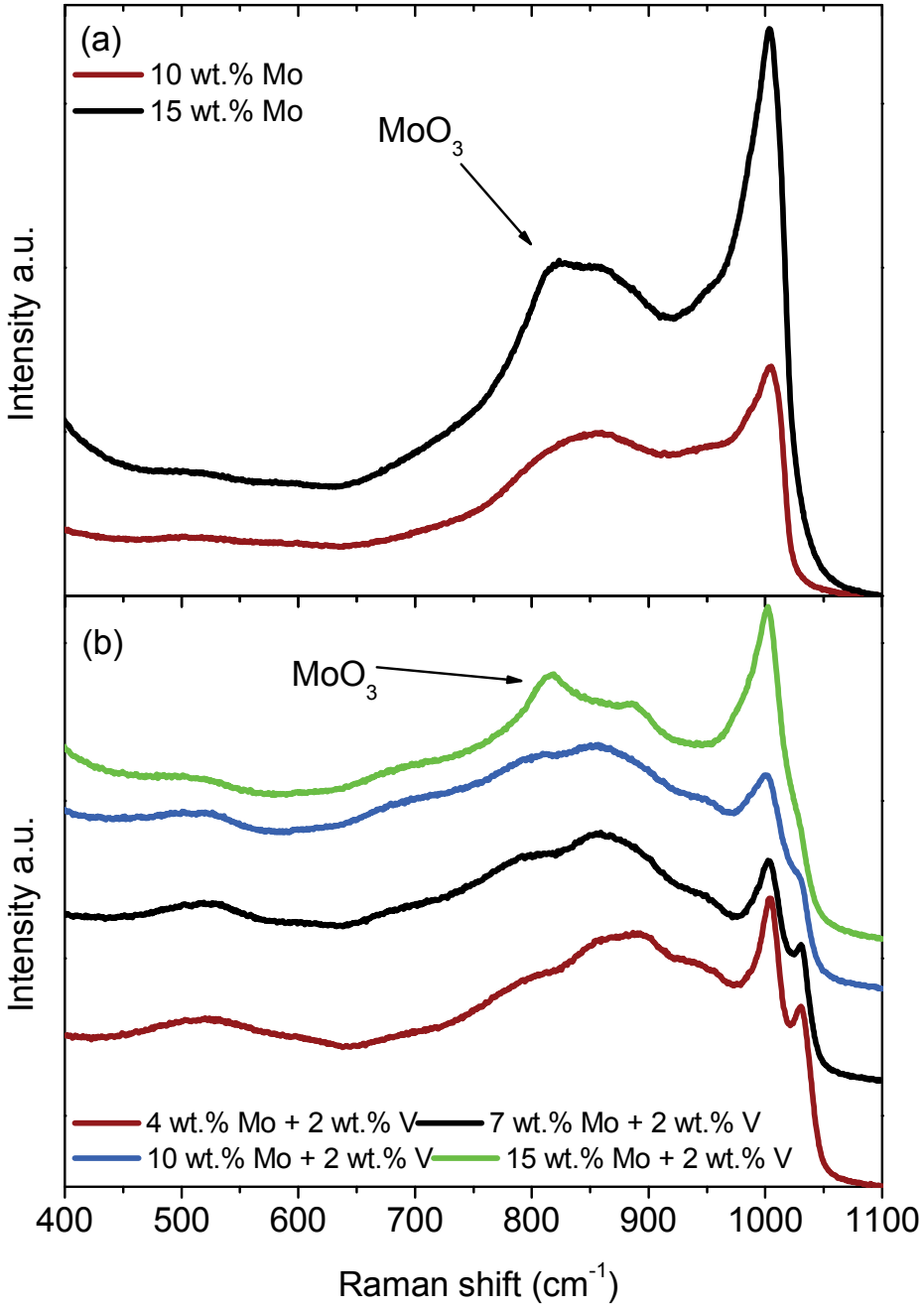

Figure 8.2: Laser Raman spectra recorded at room temperature after dehydration at 550 °C of the only molybdenum oxide series (a) and the mixed molybdenum-vanadium oxide series (b). Mainly supported MoO_x species is observed for the molybdenum oxide samples, with weak indication of crystalline MoO_3 at 820 cm^{-1}. The molybdenum-vanadium oxide samples showed a mixture of supported VO_x and MoO_x species at the lowest transition metal loadings, but with increasing Mo loading the VO_x signal diminished and crystalline MoO_3 was detected.

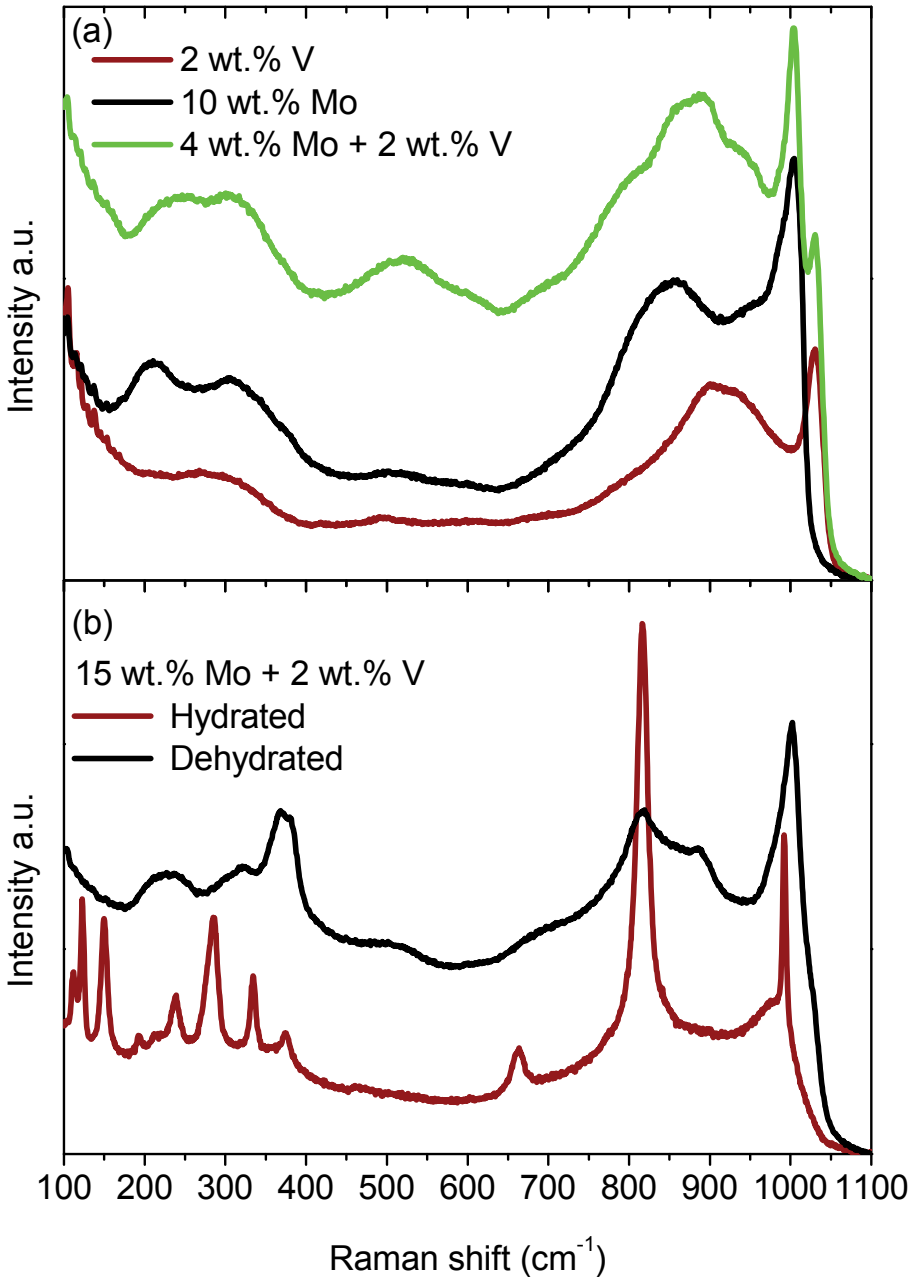

Figure 8.3: (a) Comparison of the Raman spectra of 4 wt.% Mo + 2 wt.% V, 10 wt.% Mo and 2 wt.% V clearly showing that supported VO_x and MoO_x species co-exists in the mixed molybdenum-vanadium oxide catalyst. Spectra recorded at room temperature after dehydration at 550 °C (b) Comparison of the Raman spectra of the 15 wt.% Mo+2 wt.% V catalyst before and after dehydration. Crystalline MoO_3 is clearly observed in the as-prepared hydrated state (in good agreement with XRD, see Figure 8.1), but minimizing the surface energy by thermal spreading during dehydration at 550 °C results in mostly supported MoO_x species.

8.3.4 UV-vis diffuse reflectance spectroscopy

The only molybdenum containing samples appeared white to light blue. The UV-vis spectra of the 10 and 15 wt.% Mo samples are shown in Figure 8.4a. The metal to ligand charge transfer (LMCT) band of $O^{2-} \rightarrow Mo^{6+}$ is observed at 242 and 248 nm respectively, in good agreement with supported molybdenum oxide species in tetrahedral coordination [142-143]. The charge transfer band for crystalline MoO_3, where molybdenum is in octahedral coordination, would be expected around 350 nm [142]. The absorption in the visible and near infrared region of the spectrum is due to *d–d* transitions of Mo^{5+} or Mo^{4+}, showing that Mo is partly reduced directly after synthesis.

The molybdenum-vanadium oxide catalyst appeared yellow after synthesis, but turned light green after ambient storage. The LMCT band was also observed around 250 nm, but it was broader and had a shoulder around 350 nm (see Figure 8.4b). This is likely due to supported vanadium oxide species, but could also be Mo^{6+} in octahedral coordination since crystalline MoO_3 was detected by XRD for the 15wt.% Mo+2wt.% V sample. Weak absorption in the visible region of the spectrum could be due to *d–d* transitions of either reduced vanadium and/or molybdenum.

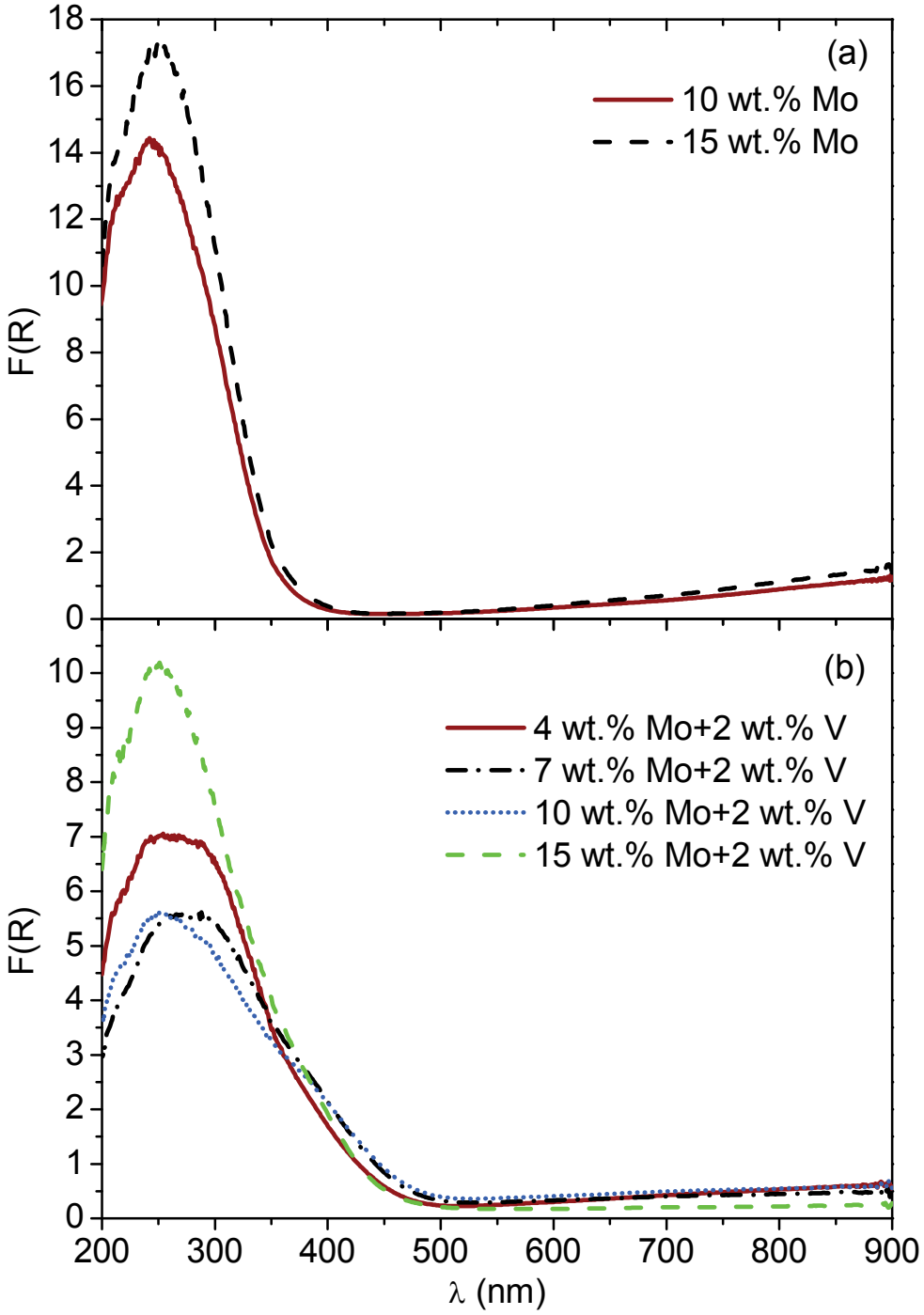

Figure 8.4: UV-vis spectra of the only molybdenum oxide series (a) and the mixed molybdenum-vanadium oxide series (b) recorded on the as-prepared oxide catalyst in the hydrated state. The strong ligand to metal charge transfer band in the UV-region (200 to 400 nm) is due to supported MoO_x and VO_x species, while weak absorption in the visible and NIR regions (400 to 700 and 700 to 900 nm respectively) is due to *d–d* transitions of partly reduced molybdenum and/or vanadium.

8.3.5 Catalytic activity and selectivity

The synthesized materials were evaluated as catalysts for the oxidative dehydrogenation of propane in fixed bed reactors. The gas composition was constantly $C_3H_8/O_2/N_2$ = 5/25/70, the flows were 50, 80, 100, 150 and 200 Nml/min and the temperatures were 460, 480 and 500 °C as the furnace set point (the actual reaction temperature was measured in the catalyst bed). The weight of catalyst was optimized for each sample to achieve lower than 40 % propane conversion at 500 °C and 50 Nml/min flow (see Table 8.2).

Comparing selectivity as function of conversion traces (measured at all 15 flow-temperature combinations) for the molybdenum oxide catalysts showed, that a significantly better selectivity was achieved for the high loaded molybdenum catalysts (5 to 15 wt.% Mo), compared to the low loaded catalysts (1 and 2 wt.% Mo), with the 10 wt.% Mo appearing to be the optimal (see Figure 8.5a). This was the opposite trend of the previously investigated vanadia on alumina catalysts, where propene selectivity decreased with increasing vanadia loading (see Section 6.3.6). A similar trend of increasing selectivity in increasing MoO_x surface loading was observed by other researchers [69,144]. The 10 wt.% Mo catalyst, the best of the molybdenum series, had slightly lower selectivity as function of conversion compared to the best vanadia based catalyst at 2 wt.% V (see Section 6.3.6).

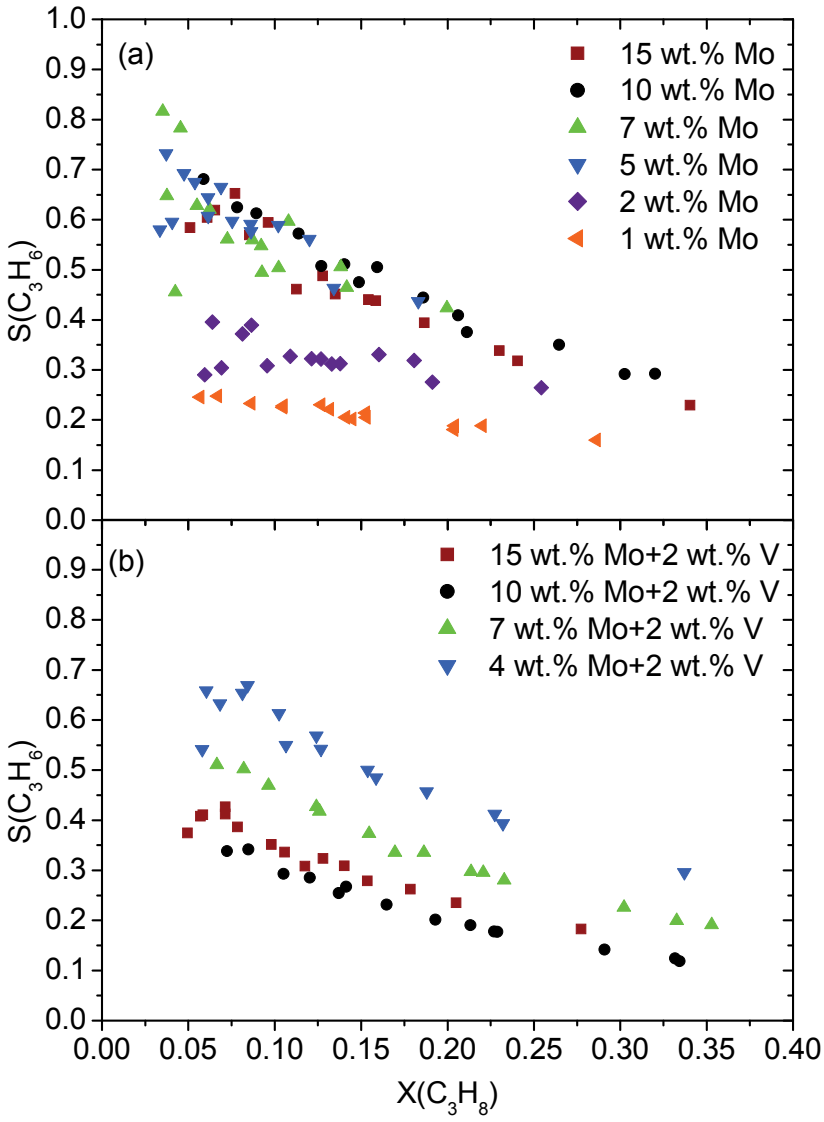

Figure 8.5: Propene selectivity as function of propane conversion of the only molybdenum oxide series (a) and the mixed molybdenum-vanadium oxide series (b). The gas composition was $C_3H_8/O_2/N_2$ = 5/25/70, the flow between 50 and 200 Nml/min and the temperature between 460 and 500 °C (furnace set-point). The amount of catalyst depended on the transition metal loading (see Table 8.2).

Table 8.3: Optimal propene yield obtained, the corresponding propane conversion and the maximum space time yield obtained at the highest temperature and flow rate.

Sample	Yield (%)[a]	Conv. (%)[b]	STY ($g_{propene}/[g_{cat}\cdot h]$)[c]
1Mo	4.6	29	0.066
2Mo	6.7	25	0.081
5Mo	8.0	18	0.107
7Mo	8.5	20	0.175
10Mo	9.4	32	0.271
15Mo	7.8	34	0.302
4Mo2V	10.0	34	0.879
7Mo2V	6.8	30	0.857
10Mo2V	4.1	33	0.570
15Mo2V	5.1	28	0.453

[a] Maximum propene yield obtained, [b] propane conversion at the maximum propene yield, [c] maximum weight time yield in grams of propene pr. gram of catalyst pr. hour (which was always obtained at 500 °C oven set-point and 200 Nml/min flow).

Similarly, when comparing the selectivity as function of conversion traces for the mixed molybdenum-vanadium oxide catalysts, the best selectivity was obtained at the lowest transition metal loading of 4 wt.% Mo+2 wt.% V (see Figure 8.5b), indicating that vanadia is dominating the catalytic properties. The selectivity decreased when increasing the molybdenum loading to 7 and 10 wt.% Mo, but improved again slightly when increasing it further to 15 wt.% Mo. The best selectivity obtained for this series of catalysts was better than the selectivity obtained when using only molybdenum oxide, but a little lower than for only vanadia (see Section 6.3.6). The best propene yield of the molybdenum oxide series was 9.4 % for the 10 wt.% Mo catalyst and for the molybdenum-vanadium oxide series it was 10.0 % for the 4 wt.% Mo+2wt.% V catalyst (see Table 8.3). This is compared to 12.6 % for 2 wt.% V catalyst (see Section 6.3.6).

The catalytic activity of the mixed molybdenum-vanadium oxide catalysts were however much higher than for the others, since around 33 % propane conversion was achieved at 500 °C and 50 Nml/min flow using only 75 mg of 4 wt.% Mo+2 wt.% V, compared to 300 mg of 10 wt.% Mo and 150 mg of 2 wt.% V. A similar trend of increased catalyt-

ic activity by adding molybdenum oxide to vanadia catalysts was observed by Nayak et al. [145]. Increasing the vanadia content, compared to adding molybdenum to vanadia catalysts, however, has a much stronger effect, since only approximately 26 mg of 5 wt.% V catalyst would be needed for 33 % propane conversion at 500 °C and 50 Nml/min flow (calculated using the kinetic parameters in Table 7.4).

The space time yield (STY) obtained also reflected this higher activity, but slightly lower selectivity since 0.879 $g_{propene}/(g_{cat} \cdot h)$ was obtained for 4 wt.%Mo+2 wt.% V catalyst, 0.302 $g_{propene}/(g_{cat} \cdot h)$ for the 15 wt.% Mo catalyst and 0.782 $g_{propene}/(g_{cat} \cdot h)$ for the 3 wt.% V catalyst, which were the best in the three series (see Table 8.3 and Table 6.4). The activity of the mixed molybdenum-vanadium oxide is also larger than the sum of the individual components, since using 75 mg of 2 wt.% V and 75 mg of 5 wt.% Mo catalysts would result in 20 % conversion for the vanadia catalyst and 4 % conversion for the molybdenum oxide catalyst at 500 °C and 50 Nml/min according to the model results, compared to the measured 33 % conversion for the 4 wt.%Mo+2 wt.% V catalyst. This indicates that there is favorable interaction between molybdenum and vanadium oxide, resulting in higher activity when present on the same alumina surface. One way to interpret this is that vanadia activates the molybdenum oxide since this is normally not very active.

Using a previously described kinetic model, it was possible to fit the measured propane conversions and the propene yields against this (see Section 7.3). The model consists of three reactions: oxidative dehydrogenation of propane (ODP, k_1), parallel combustion of propane (k_2) and sequential combustion of propene (k_3). All three reactions were assumed to be first order in hydrocarbon and zeroth order in oxygen [75,89]. The measured conversions of propane as function of the weight based contact time at different

temperatures for the 10 wt.% Mo catalyst could be fitted against the model using a one-parameter fit for the sum of the rate constants for the ODP and propane combustion reactions $k_1 + k_2$ (see Figure 8.6a). The measured yields of propene as function of the weight based contact time at different temperatures could also be fitted against the model using a three parameter fit for k_1, k_2, and k_3, with the sum of k_1+k_2 already determined as a constraint (see Figure 8.6b).

The measured reaction rate constants fitted Arrhenius type behavior, as determined by straight line fits to the logarithmic form of the Arrhenius equation (see Figure 8.7). The measured apparent activation energies and pre-exponential factors are summarized in Table 8.4. The activation energy of the ODP reaction was between 80 to 90 kJ/mol irrespective of the type of catalyst (with the exception of the 1 wt.% Mo and 15 wt.% Mo+2wt.%V catalysts); however, the pre-exponential factor was significantly higher for the mixed molybdenum-vanadium oxide catalysts, explaining the much higher activity of this series compared to the only molybdenum oxide series. The activation energies are similar to previous measurements on alumina supported molybdenum oxide [144].

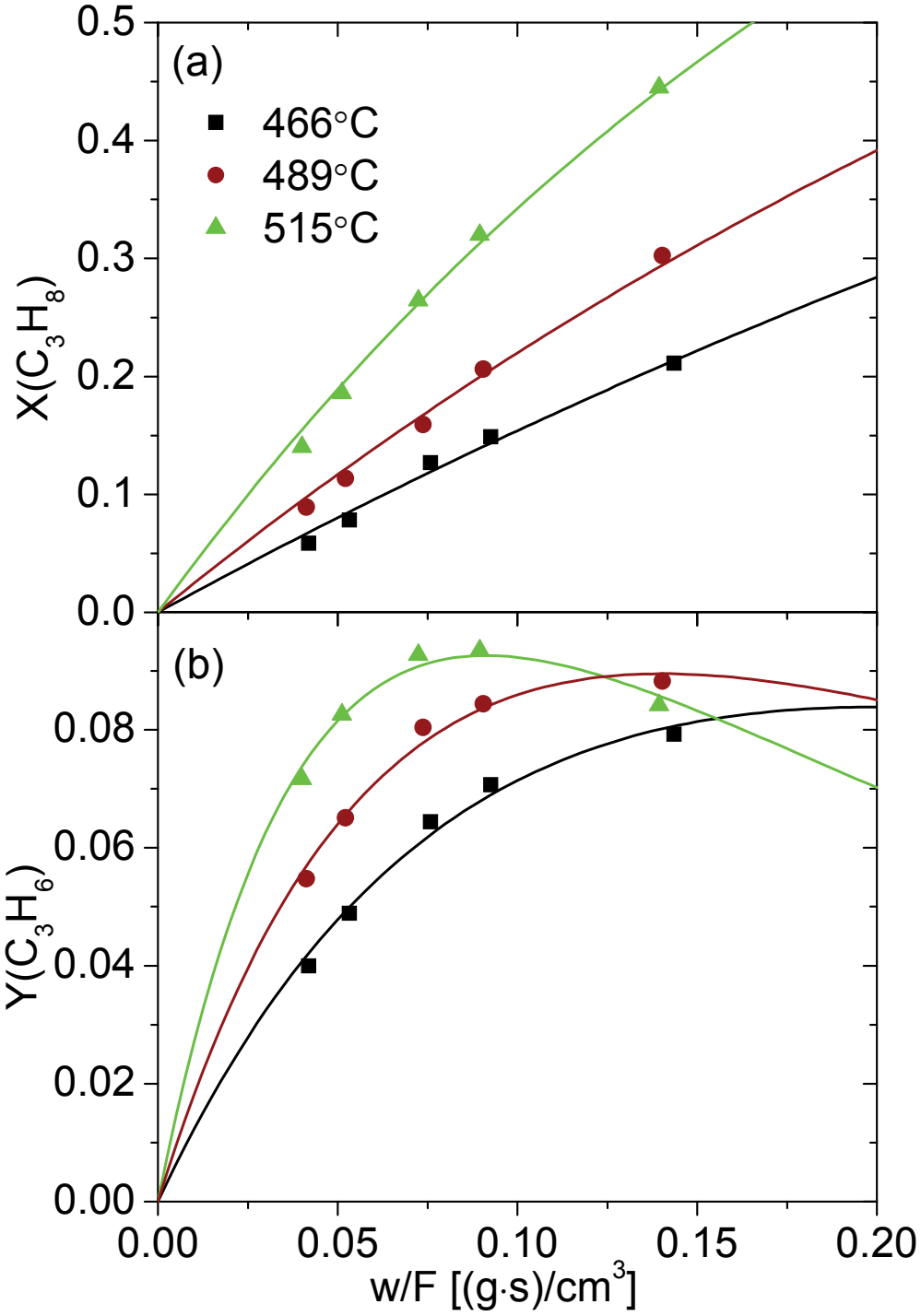

Figure 8.6: Conversion of propane (a) and yield of propene (b) as function of the weight based contact time for the 10 wt.% Mo catalyst. Points are the measured experimental data and solid lines are fits according to the kinetic model. The gas composition was $C_3H_8/O_2/N_2$ = 5/25/70, the flow between 50 and 200 Nml/min and the amount of catalyst was 300 mg.

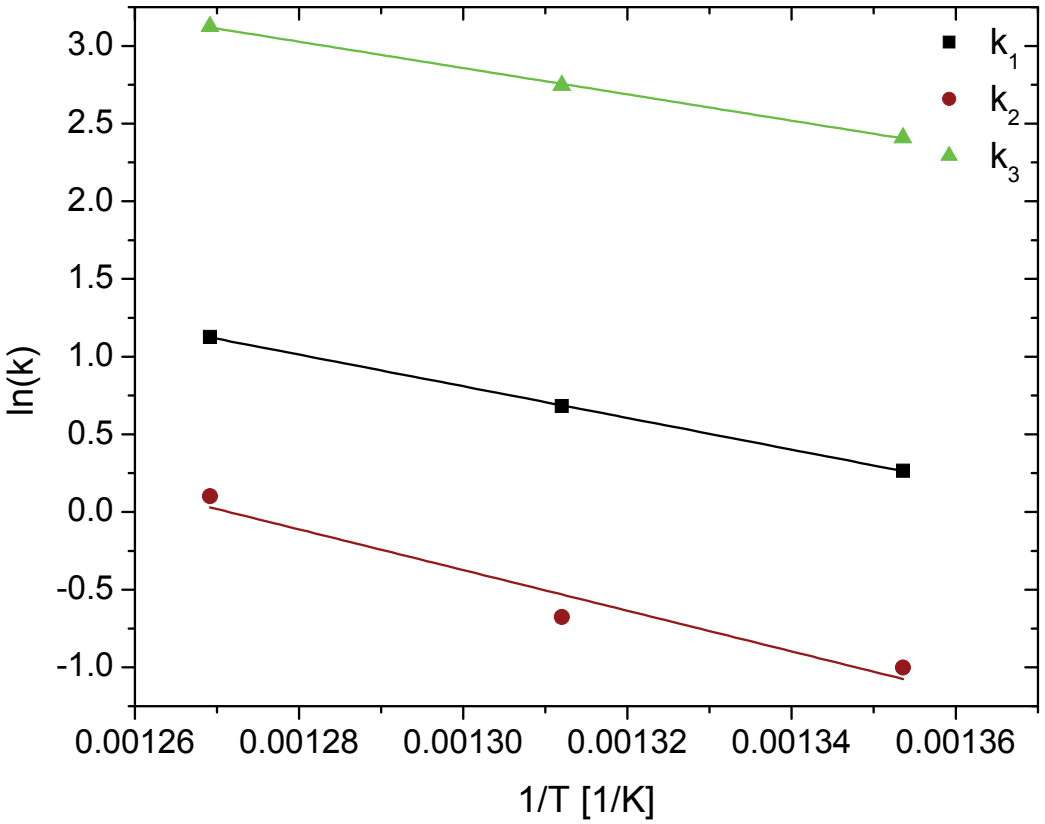

Figure 8.7: Arrhenius plots for the reaction rate constants for the oxidative dehydrogenation of propane (k_1), the parallel combustion of propane (k_2) and the sequential combustion of propene (k_3).

Table 8.4: Pre-exponential factors and apparent activation energies determined from straight line fits to Arrhenius plots of the first order rate constants.

Sample	**$k_{0,1}$ ($cm^3/(g \cdot s)$)**	**$E_{a,1}$ (kJ/mol)**	**$k_{0,2}$ ($cm^3/(g \cdot s)$)**	**$E_{a,2}$ (kJ/mol)**	**$k_{0,3}$ ($cm^3/(g \cdot s)$)**	**$E_{a,3}$ (kJ/mol)**
1Mo	$2.45 \cdot 10^6$	99.1	$5.57 \cdot 10^6$	100.2	$2.29 \cdot 10^4$	51.3
2Mo	$6.75 \cdot 10^5$	89.9	$1.29 \cdot 10^6$	93.1	$4.38 \cdot 10^3$	43.0
5Mo	$2.32 \cdot 10^5$	80.8	$2.43 \cdot 10^7$	119.1	$3.36 \cdot 10^3$	40.2
7Mo	$7.93 \cdot 10^5$	86.0	$2.09 \cdot 10^{10}$	157.7	$3.49 \cdot 10^3$	38.4
10Mo	$1.28 \cdot 10^6$	84.8	$1.69 \cdot 10^7$	108.8	$1.05 \cdot 10^6$	70.4
15Mo	$1.69 \cdot 10^6$	86.0	$8.43 \cdot 10^9$	145.5	$1.68 \cdot 10^7$	86.8
4Mo2V	$3.96 \cdot 10^6$	84.8	$1.19 \cdot 10^{10}$	142.8	$2.02 \cdot 10^6$	68.3
7Mo2V	$3.60 \cdot 10^6$	83.6	$9.30 \cdot 10^8$	121.4	$1.71 \cdot 10^7$	78.6
10Mo2V	$2.82 \cdot 10^6$	83.7	$9.44 \cdot 10^8$	119.2	$1.10 \cdot 10^7$	74.0
15Mo2V	$3.61 \cdot 10^5$	73.5	$1.24 \cdot 10^7$	95.6	$3.43 \cdot 10^6$	70.9

The activation energy for the propane combustion reaction varied from 93 to 158 kJ/mol, which was generally higher than for the ODP reaction. The pre-exponential factor for this reaction also varied significantly, but the ratio k_2/k_1 was between 0.02 and 0.5 for the 5 to 15 wt.% Mo catalyst and between 1.0 and 1.9 for the 1 and 2 wt.% Mo catalysts in the relevant temperature interval of 350 to 500 °C (see Figure 8.8), in good agreement with other measurements [69]. For the mixed molybdenum and vanadium oxide catalysts the k_2/k_1 ratio varied between 0.04 and 1.3, lowest for the 4 wt.% Mo+2 wt.% V catalyst and highest for the 10 wt.% Mo+2 wt.% V catalyst. The k_2/k_1 ratio increased with increasing temperature due to the higher activation energy of the propane combustion reaction. In order to maximize the propene selectivity, the k_2/k_1 ratio should be as low as possible.

The activation energy for the propene combustion reaction varied from 38 to 87 kJ/mol, which was generally lower than for the ODP reaction. Likewise there was significant variation in the pre-exponential factor. However; k_3 was always significantly larger than k_1, resulting k_3/k_1 ratios between 9 and 95 for the molybdenum oxide catalysts and between 7 and 26 for the mixed molybdenum-vanadium oxide catalysts (see Figure 8.9), in good agreement with other measurements [69]. The k_3/k_1 ratio decreased with increasing temperature and should be as low as possible in order to maximize the propene selectivity.

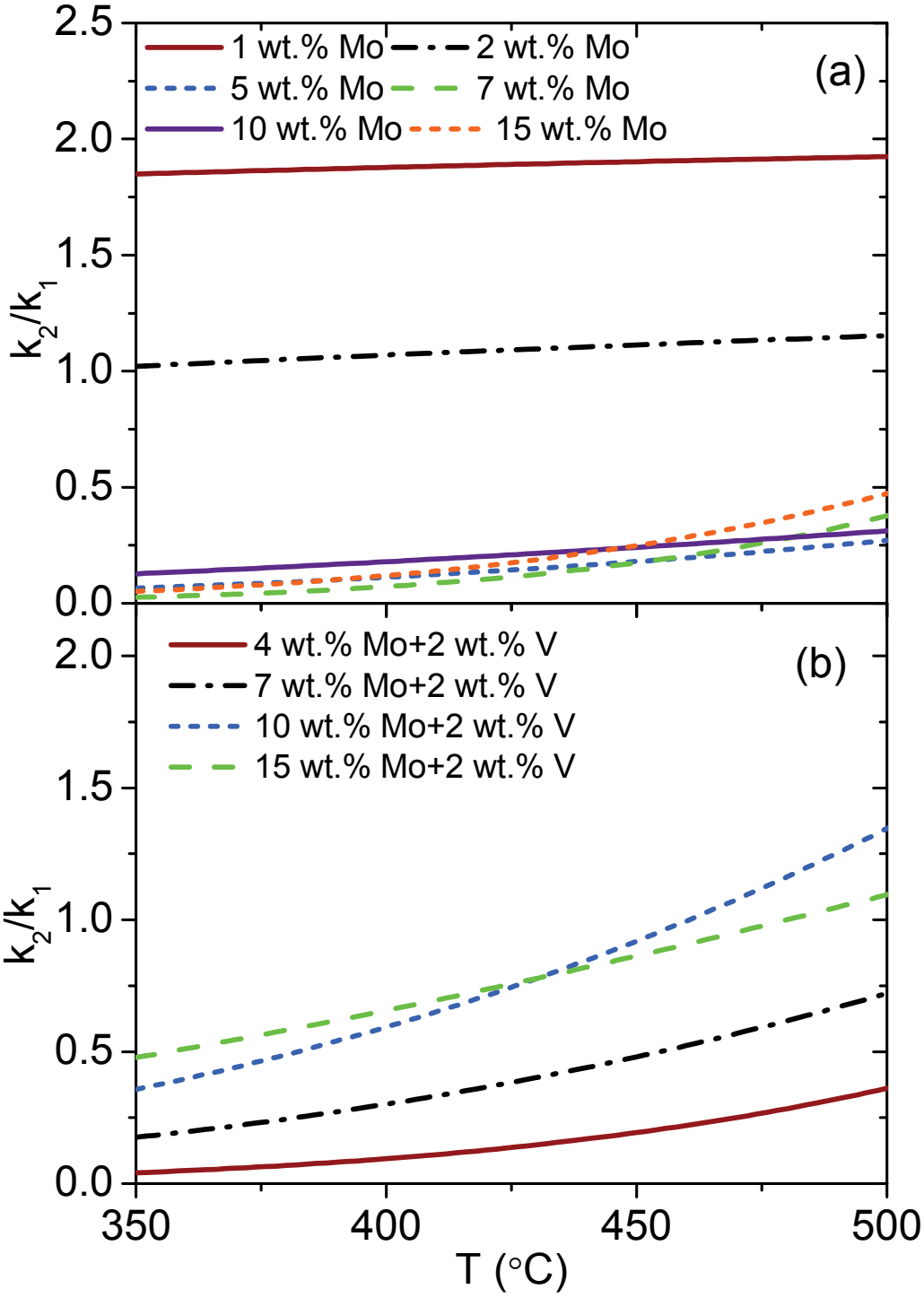

Figure 8.8: Calculated relative reaction rate constants for the combustion of propane (k_2) and the oxidative dehydrogenation of propane (k_1) based on the kinetic parameters in Table 8.4 for the only molybdenum oxide series (a) and the mixed molybdenum-vanadium oxide series (b).

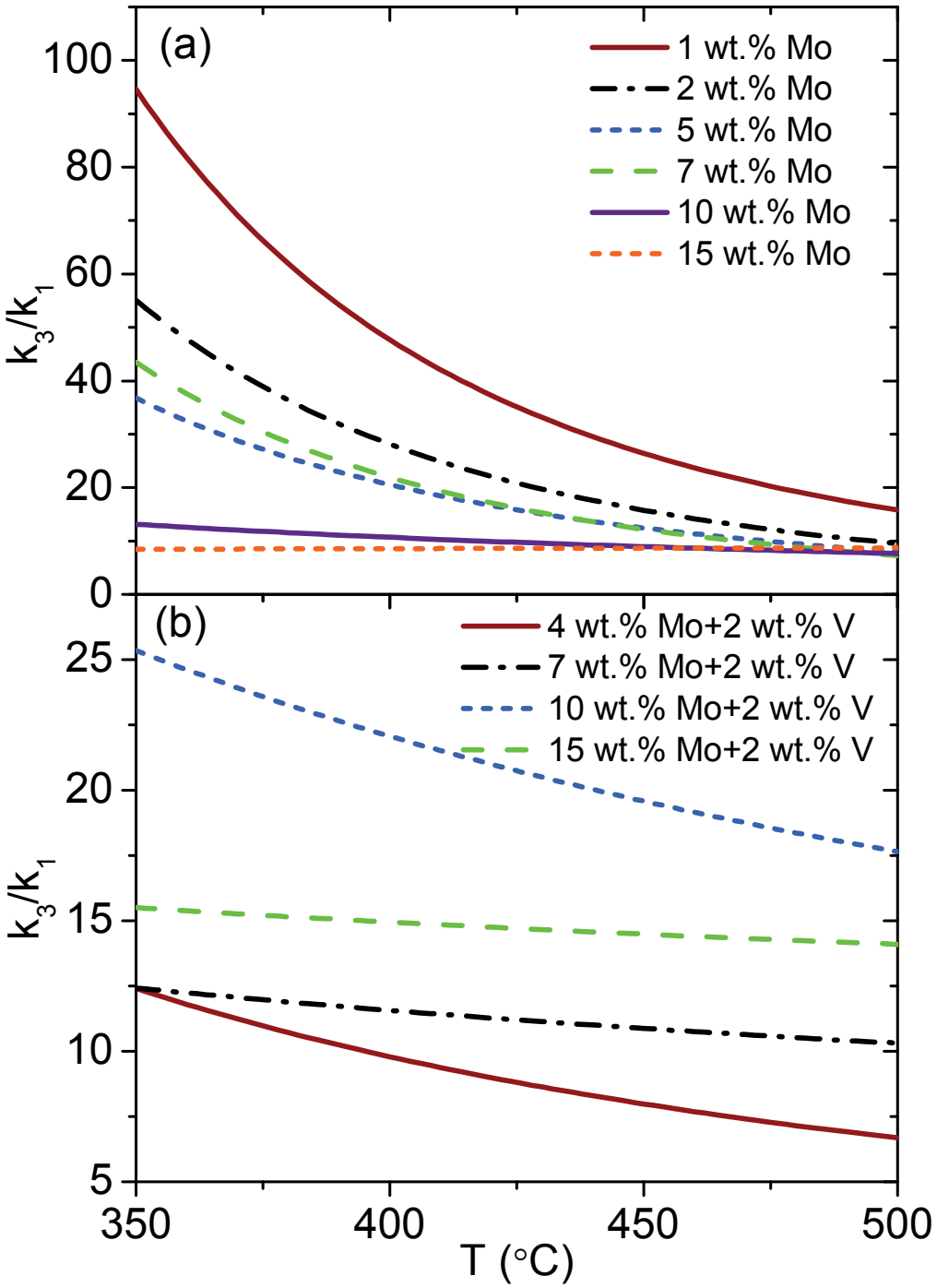

Figure 8.9: Calculated relative reaction rate constants for the combustion of propene (k_3) and the oxidative dehydrogenation of propane (k_1) based on the kinetic parameters in Table 8.4 for the only molybdenum oxide series (a) and the mixed molybdenum-vanadium oxide series (b).

By calculating the reaction rate constants as function of temperature, the yield of propene could be calculated as function of both temperature and weight based contact time. This showed that the best propene yield was achieved at short contact time and relatively high temperature (up to 500 °C, above which homogeneous combustion reactions become important), see contour plot in Figure 8.10 for the 10 wt.% Mo catalyst. On the contour plot there is a relatively large area with high yield, stretching from short contact time and high temperature towards intermediate temperature and long contact time. Moving away from this region towards lower temperature, the rate of the ODP reaction becomes too low and towards higher temperature the rate of the combustion reaction becomes too high. Increasing the contact time will result in high conversion, but the sequential combustion of propene will limit the yield, since the reaction rate constant of this is always significantly higher than the reaction rate constant of the ODP reaction. Decreasing the contact time will result in too low conversion to achieve a high yield. On an absolute scale a yield of up to 10 % is not particularly high. The problem of obtaining a better yield is the opposite trend in the temperature dependence of the k_2/k_1 and k_3/k_1 ratios, which shows that improved catalysts should be developed.

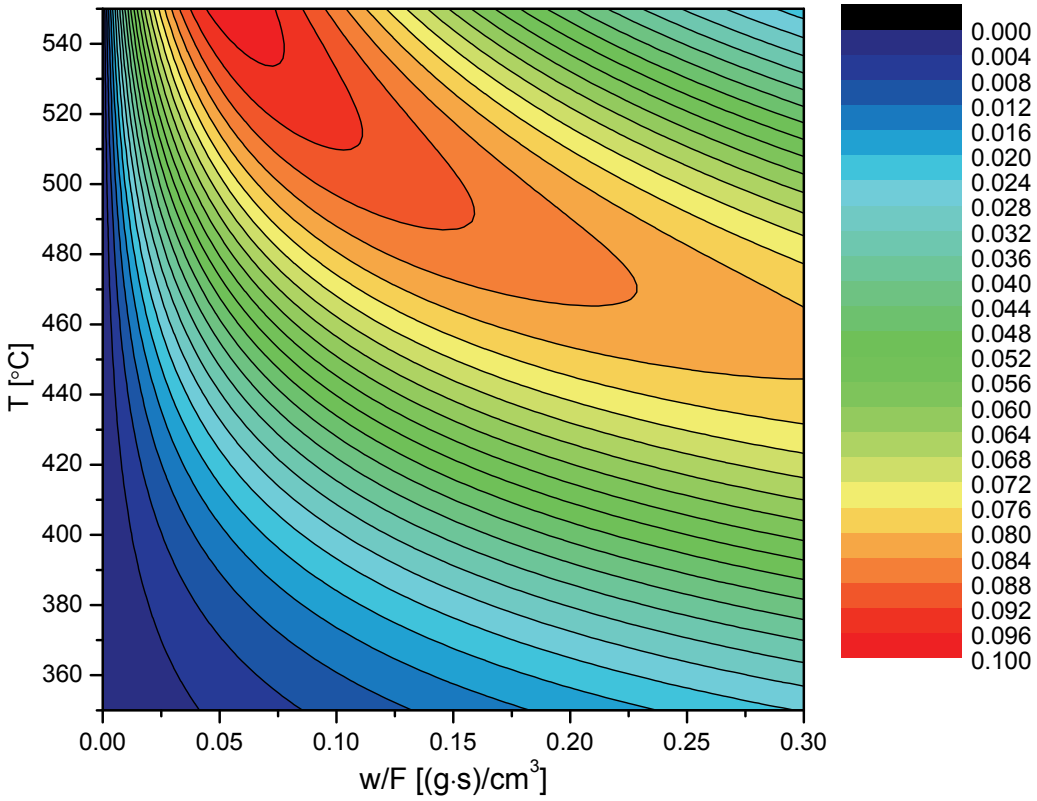

Figure 8.10: Calculated yield of propene as function of the weight based contact time and the temperature for the 10 wt.% Mo catalyst. Based on the kinetic parameters in Table 8.4.

8.4 Conclusions

Series of alumina supported molybdenum oxide and mixed molybdenum-vanadium oxide catalysts were successfully prepared by flame spray pyrolysis. Raman spectroscopy and XRD showed that the product of the flame synthesis was MoO_x and VO_x species supported on γ-alumina, with only small amounts of crystalline MoO_3 observed at high transition metal loadings. The most selective catalysts of the only molybdenum oxide series were those with high loadings (5 to 15 wt.% Mo), with a maximum propene yield of 9.4 % for the 10 wt.% Mo catalyst. The most selective catalyst of the mixed molyb-

denum- vanadium oxide series was at low transition metal loadings of 4 wt.% Mo and 2 wt.% V, with a maximum propene yield of 10.0 %. The catalytic activity of the vanadia containing catalysts was much higher than for the only molybdenum oxide catalysts, with a maximum space time yield of 0.879 $g_{propene}/(g_{cat} \cdot h)$ for the 4 wt.% Mo and 2 wt.% V catalyst, compared to 0.302 $g_{propene}/(g_{cat} \cdot h)$ for the 15 wt.% Mo catalyst. Catalytic activity increased with increasing transition metal loading.

The measured conversion of propane and yield of propene could be described by a kinetic model consisting of oxidative dehydrogenation of propane (ODP), parallel combustion of propane and sequential combustion of propene. This showed that the reaction rate constant for the combustion of propane relative to the ODP reaction was higher than 1 for the least selective catalysts and less than 0.2 for the most selective catalysts between 350 and 500 °C. This ratio increased with increasing temperature. The reaction rate constant of the consecutive combustion of propene relative to the ODP reaction was less than 15 for the most selective catalysts and up to 95 for the least selective catalysts between 350 and 500 °C. This ratio decreased with increasing temperature. The opposite temperature dependence of the relative reaction rate constants strongly limits the yield of propene.

9. Conclusions and outlooks

9.1 Hydrotreating

Flame spray pyrolysis as one-step catalyst synthesis method was successfully used to synthesize highly active CoMo hydrotreating catalysts. Using two-nozzle FSP and silica addition in one-nozzle FSP the unwanted $CoAl_2O_4$ phase, formed in one-nozzle FSP of $CoMo/Al_2O_3$, was successfully avoided. This is an example of how FSP can be used to prepare more active catalysts. These flame-made catalysts could potentially be used as industrial catalysts for hydrotreating, since the activities obtained are close to the activities of the commercial reference, which have been optimized during many years of research.

The two-flame process can be further optimized by adding silica and by optimizing the surface area, which was rather low for the catalysts prepared in this study. Also, the possibility of adding other promoter atoms like B, P or Mg has not been investigated. Furthermore, the concentrations of Mo and Co can be optimized. Nickel promoted molybdenum sulfide catalysts have not been investigated so far, but for this type of catalyst $NiAl_2O_4$ is a possible FSP product, which should be avoided like $CoAl_2O_4$. Since nickel containing catalysts are toxic and have potential allergy induction, the present work has exclusively concentrated on the cobalt-based catalysts. However, with appropriate safety precautions in corresponding fume cupboards the same strategy can be applied.

Besides finding a highly active hydrotreating catalyst formulation by lab-scale FSP, the up-scaling of this is a significant engineering problem which is currently being addressed [25-27]. Powder handling will be a big challenge, since the very fluffy FSP product must be compacted and formulated into shapes that could be loaded in an indus-

trial reactor. This could be done either by pressing pellets or by making pastes of the FSP product that could be shaped as extrudates in the conventional way.

Another way that FSP could be utilized is for the synthesis of the high surface area support material itself. This could then be impregnated with molybdenum and cobalt in the conventional way, in order to evaluate the support material properties of the FSP products. The first work in this direction, which was started but not finished during this Ph.D. work, was to impregnate alumina and silica-alumina mixtures (with the same Si/Al ratios as in Section 5) prepared by FSP with Mo+Co solutions and evaluate the hydrotreating catalytic activity after calcination and sulfidation. Initial results showed reasonable activity, indicating this may be a viable method.

There is no doubt, that hydrotreating will continue to be an important process in the refining industry, in particular, because of more stringent regulations and oils that contain more sulfur. Another potential application is the removal of not only nitrogen and sulfur, but also oxygen from bio oil [146].

9.2 Oxidative dehydrogenation

Oxidative dehydrogenation of propane is a very challenging reaction due to the lower C–H bond energy of the methyl group of propene than those of propane [89]. Thus finding catalysts that are more reactive for propane oxidation than propene oxidation is very demanding. The FSP synthesized vanadium and molybdenum oxide catalysts are equally selective as catalysts prepared by conventional methods, but the improvement was not significant. The similar chemical structure of the FSP made catalysts and conventionally made catalysts, as determined with spectroscopy, makes this a reasonable outcome. Also, the determined activation energies and reaction rate constants for the ODP

and combustion reactions are similar to what has been measured on conventional catalysts.

Commercial exploitation of the ODP process seems very unlikely, unless a breakthrough catalyst design or new reactor designs are discovered. This was also the conclusion of a poster symposium at the International Congress on Catalysis 2012 [147]. For ethane oxidative dehydrogenation the situation is different, since ethene is a more stable molecule than ethane. This is being investigated at pilot scale using MoVTeNb mixed oxides as catalyst [148]. When these catalysts are used for propane oxidative dehydrogenation, acrylic acid is the main product (with 20 % water in the inlet gas), formed by subsequent reactions of propene, but this is a very important intermediate product, too [149]. Future experiments with the most selective FSP made vanadia and molybdenum oxide catalysts could be to investigate their performance in ethane oxidative dehydrogenation.

Another possibility for improving the selectivity is to use N_2O or CO_2 as oxidants [150-151]. The former is however less available on large scale and the latter is a rather stable molecule. As a consequence the reaction between CO_2 and propane is endothermic, which is one of the problems of non-oxidative dehydrogenation, which is desired to overcome by an oxidative process. Finally, partial oxidative and partial non-oxidative dehydrogenation is possible, but will result in some coking of the catalyst [152]. However, less than for purely non-oxidative dehydrogenation, but on large scale and long terms regeneration of the catalyst will most likely be necessary.

9.3 Extension of FSP-synthesis to further catalysts

Synthesizing catalysts with FSP is a very attractive topic, thus further choices have been made with regards to which reactions and catalyst systems were to be studied. Besides

the hydrotreating and oxidative dehydrogenation catalysts described in this thesis, other catalysts and materials were briefly investigated or considered.

Vanadia catalysts supported on titania and magnesia were also synthesized and evaluated for ODP. Magnesia supported catalysts were significantly less active and titania supported catalysts significantly less selective than alumina based catalysts.

Amorphous silica-titania catalysts for selective epoxidation of olefins in liquid phase, an alternative to TS-1 zeolites [153], were synthesized successfully without anatase titania being detected by XRD, showing that titanium atoms were well dispersed in the amorphous silica matrix. This catalyst was used to test the FSP setup was working properly, but the performance was not as good as other flame-made materials (by vapor flame synthesis) described in the literature [35,154].

Amorphous tin dioxide-silica mixtures were synthesized and briefly investigated for conversion of sugar to methyl lactate, as alternative to Sn containing Beta zeolite [155]. Initial results showed high conversion and reasonable selectivity to methyl lactate. Also tetragonal zirconia was synthesized as potential anti-shrinking additives for dental fillings [156]. Both these collaborations with research groups in those fields have not been deepened, so the topics should be investigated in detail in the future.

Alumina supported copper-cobalt oxide was attempted by FSP, to be used as catalysts for higher alcohol synthesis after reduction to copper-cobalt metal alloy [157]. However, the product of FSP synthesis appeared to be mostly $CoAl_2O_4$ and $CuAl_2O_4$, which are much more stable than copper- and cobalt oxides, so they did not reduce to the metals upon activation and are expected to be inactive as catalysts. For future investigations silica supported or unsupported catalysts could be interesting, with the same strategy as for the cobalt-based hydrotreating catalysts.

Besides hydrotreating, also hydrocracking catalysts were considered. Mixed oxides with cation charge mismatch like Si^{4+}/Al^{3+}, Ti^{4+}/Al^{3+}, Zr^{4+}/Al^{3+}, Nb^{5+}/Ti^{4+}, Nb^{5+}/Al^{3+} and Nb^{5+}/Zr^{4+} oxides (unlike Sn^{4+}/Si^{4+} and Ti^{4+}/Si^{4+} oxides as described above were the cation 4+ charges match), could potentially form acidic sites with hydrocracking activity and possibly different selectivities compared to other acidic catalysts [158-159]. Indeed, silica-alumina mixtures prepared by FSP have been shown to contain high concentration of acidic sites [119]. Also, noble metals could easily be added to the FSP-made oxide catalysts to add hydrogenation activity. However, lack of experimental facilities for evaluating the catalysts limited this project, but might be interesting in the future.

9.4 Outlook

FSP has been demonstrated as synthesis method for a wide variety of catalysts and the development of two-nozzle FSP adds the possibility of controlling the multi-metal products, in particular, since not only two components can be prepared independently but also the distance and angle between the two flames can be varied. Even more flexibility could be obtained by using a three-nozzle apparatus.

Up-scaling FSP with similar catalytic properties of the products seems to be the major challenge to be addressed, since high production rates may result in lower specific surface area [27].

Other catalyst systems where FSP could be of interest are steam reforming, which has recently been demonstrated with ethanol as substrate [160], methanol synthesis (vapor flame materials have been prepared for methanol synthesis [161]), the water gas shift reaction (both high and low temperature catalysts, the latter has been demonstrated [162-163]) and sulfuric acid synthesis [164]. These are very important, large scale pro-

cesses for bulk chemicals and their catalysts are complicated multi-metal materials which have been developed for many years. Therefore it must be expected, that initial results are not immediately competitive, but evaluating their potential by comparison to industrial type catalysts is important.

In addition, FSP appears to be very favorable for preparation of supported noble metal catalysts [7], with application in fine chemical synthesis and environmental catalysis, where only a small amount of catalyst is needed for full scale application. This may be the first practical application of FSP made catalysts [25].

10. References

[1] R. Strobel, S.E. Pratsinis, J. Mater. Chem. 17 (2007) 4743-4756.
[2] L. Mädler, KONA. 22 (2004) 107-120.
[3] L. Mädler, H.K. Kammler, R. Mueller, S.E. Pratsinis, J. Aerosol Sci. 33 (2002) 369-389.
[4] H.K. Kammler, L. Mädler, S.E. Pratsinis, Chem. Eng. Technol. 24 (2001) 583-596.
[5] W.Y. Teoh, R. Amal, L. Mädler, Nanoscale. 2 (2010) 1324-1347.
[6] R. Strobel, A. Baiker, S.E. Pratsinis, Adv. Powder Technol. 17 (2006) 457-480.
[7] R. Strobel, S.E. Pratsinis, Platinum Met. Rev. 53 (2009) 11-20.
[8] S. Hannemann, J.-D. Grunwaldt, P. Lienemann, D. Günther, F. Krumeich, S.E. Pratsinis, A. Baiker, Appl. Catal., A. 316 (2007) 226-239.
[9] W.J. Stark, M. Maciejewski, L. Mädler, S.E. Pratsinis, A. Baiker, J. Catal. 220 (2003) 35-43.
[10] W.J. Stark, J.-D. Grunwaldt, M. Maciejewski, S.E. Pratsinis, A. Baiker, Chem. Mater. 17 (2005) 3352-3358.
[11] J. Azurdia, J. Marchal, R.M. Laine, J. Am. Ceram. Soc. 89 (2006) 2749-2756.
[12] W.Y. Teoh, R. Setiawan, L. Mädler, J.-D. Grunwaldt, R. Amal, S.E. Pratsinis, Chem. Mater. 20 (2008) 4069-4079.
[13] T. Hinklin, B. Toury, C. Gervais, F. Babonneau, J.J. Gislason, R.W. Morton, R.M. Laine, Chem. Mater. 16 (2004) 21-30.
[14] R.M. Laine, J.C. Marchal, H.P. Sun, X.Q. Pan, Nature Mat. 5 (2006) 710-712.
[15] R. Strobel, J.-D. Grunwaldt, A. Camenzind, S. Pratsinis, A. Baiker, Catal. Lett. 104 (2005) 9-16.
[16] R. Strobel, F. Krumeich, W. Stark, S. Pratsinis, A. Baiker, J. Catal. 222 (2004) 307-314.
[17] R. Strobel, W. Stark, L. Mädler, S. Pratsinis, A. Baiker, J. Catal. 213 (2003) 296-304.
[18] R.S. Zhou, R.L. Snyder, Acta Crystallogr., Sect. B: Struct. Sci. 47 (1991) 617-630.
[19] A. Camenzind, R. Strobel, F. Krumeich, S.E. Pratsinis, Adv. Powder Technol. 18 (2007) 5-22.
[20] J.A. Kemmler, S. Pokhrel, J. Birkenstock, M. Schowalter, A. Rosenauer, N. Bârsan, U. Weimar, L. Mädler, Sens. Actuators, B. 161 (2012) 740-747.
[21] F.O. Ernst, H.K. Kammler, A. Roessler, S.E. Pratsinis, W.J. Stark, J. Ufheil, P. Novák, Mater. Chem. Phys. 101 (2007) 372-378.
[22] D.J. Babu, A.J. Darbandi, J. Suffner, S.S. Bhattacharya, H. Hahn, Trans. Indian Inst. Met. 64 (2011) 181-184.
[23] S.B. Bubenhofer, C.M. Schumacher, F.M. Koehler, N.A. Luechinger, R.N. Grass, W.J. Stark, J. Phys. Chem. C (2012).
[24] M. Vollenweider, T.J. Brunner, S. Knecht, R.N. Grass, M. Zehnder, T. Imfeld, W.J. Stark, Acta Biomater. 3 (2007) 936-943.

[25] B. Thiébaut, Platinum Met. Rev. 55 (2011) 149-151.
[26] K. Wegner, B. Schimmoeller, B. Thiebaut, C. Fernandez, T.N. Rao, KONA. 29 (2011) 251-265.
[27] R. Mueller, R. Jossen, S.E. Pratsinis, M. Watson, M.K. Akhtar, J. Am. Ceram. Soc. 87 (2004) 197-202.
[28] R. Mueller, L. Mädler, S.E. Pratsinis, Chem. Eng. Sci. 58 (2003) 1969-1976.
[29] A.J. Gröhn, S.E. Pratsinis, K. Wegner, Chem. Eng. J. 191 (2012) 491-502.
[30] G. Beaucage, H.K. Kammler, R. Mueller, R. Strobel, N. Agashe, S.E. Pratsinis, T. Narayanan, Nature Mat. 3 (2004) 370-374.
[31] R. Strobel, L. Mädler, M. Piacentini, M. Maciejewski, A. Baiker, S.E. Pratsinis, Chem. Mater. 18 (2006) 2532-2537.
[32] M. Swihart, Curr. Opin. Colloid Interface Sci. 8 (2003) 127-133.
[33] P. Roth, Proc. Combust. Inst. 31 (2007) 1773-1788.
[34] B. Schimmoeller, S.E. Pratsinis, A. Baiker, ChemCatChem. 3 (2011) 1234-1256.
[35] W.J. Stark, S.E. Pratsinis, A. Baiker, J. Catal. 203 (2001) 516-524.
[36] W.J. Stark, K. Wegner, S.E. Pratsinis, A. Baiker, J. Catal. 197 (2001) 182-191.
[37] J.P. Hansen, J.R. Jensen, H. Livbjerg, T. Johannessen, AIChE J. 47 (2001) 2413-2418.
[38] T. Johannessen. Synthesis of Nano-Particles in Flames. Ph.D., Technical University of Denmark, Kgs. Lyngby, 1999.
[39] T. Rudin, K. Wegner, S.E. Pratsinis, J. Nanopart. Res. 13 (2011) 2715-2725.
[40] H. Topsøe, B.S. Clausen, F.E. Massoth, in: J.R. Anderson, M. Boudart (Eds.), Catalysis: Science and Technology, vol. 11, Springer-Verlag, Berlin, 1996.
[41] R. Prins, in: G. Ertl, H. Knözinger, F. Schüth, J. Weitkamp (Eds.), Handbook of Heterogeneous Catalysis, Wiley-VCH Verlag, Weinheim, 2008, pp. 2695-2718.
[42] K.G. Knudsen, B.H. Cooper, H. Topsøe, Appl. Catal., A. 189 (1999) 205-215.
[43] R.G. Leliveld, A.J. van Dillen, J.W. Geus, D.C. Koningsberger, J. Catal. 165 (1997) 184-196.
[44] B.S. Clausen, H. Topsøe, R. Candia, J. Villadsen, B. Lengeler, J. Als-Nielsen, F. Christensen, J. Phys. Chem. 85 (1981) 3868-3872.
[45] J. Vakros, C. Papadopoulou, G.A. Voyiatzis, A. Lycourghiotis, C. Kordulis, Catal. Today. 127 (2007) 85-91.
[46] W. Huang, A. Duan, Z. Zhao, G. Wan, G. Jiang, T. Dou, K.H. Chung, J. Liu, Catal. Today. 131 (2008) 314-321.
[47] L. Wu, D. Jiao, J.-A. Wang, L. Chen, F. Cao, Catal. Commun. 11 (2009) 302-305.
[48] C. Wivel, B.S. Clausen, R. Candia, S. Mørup, H. Topsøe, J. Catal. 87 (1984) 497-513.
[49] H. Topsøe, B.S. Clausen, R. Candia, C. Wivel, S. Mørup, J. Catal. 68 (1981) 433-452.
[50] C. Wivel, R. Candia, B.S. Clausen, S. Mørup, H. Topsøe, J. Catal. 68 (1981) 453-463.

[51] T. Shido, R. Prins, J. Phys. Chem. B. 102 (1998) 8426-8435.
[52] C. Calais, N. Matsubayashi, C. Geantet, Y. Yoshimura, H. Shimada, A. Nishijima, M. Lacroix, M. Breysse, J. Catal. 174 (1998) 130-141.
[53] F. Besenbacher, M. Brorson, B.S. Clausen, S. Helveg, B. Hinnemann, J. Kibsgaard, J.V. Lauritsen, P.G. Moses, J.K. Nørskov, H. Topsøe, Catal. Today. 130 (2008) 86-96.
[54] J.V. Lauritsen, J. Kibsgaard, G.H. Olesen, P.G. Moses, B. Hinnemann, S. Helveg, J.K. Nørskov, B.S. Clausen, H. Topsøe, E. Lægsgaard, F. Besenbacher, J. Catal. 249 (2007) 220-233.
[55] A. Tuxen, J. Kibsgaard, H. Gøbel, E. Lægsgaard, H. Topsøe, J.V. Lauritsen, F. Besenbacher, ACS Nano. 4 (2010) 4677-4682.
[56] J. Kibsgaard, A. Tuxen, K.G. Knudsen, M. Brorson, H. Topsøe, E. Lægsgaard, J.V. Lauritsen, F. Besenbacher, J. Catal. 272 (2010) 195-203.
[57] M. Brorson, A. Carlsson, H. Topsøe, Catal. Today. 123 (2007) 31-36.
[58] A. Carlsson, M. Brorson, H. Topsøe, J. Microsc.-Oxf. 223 (2006) 179-181.
[59] L.P. Hansen, Q.M. Ramasse, C. Kisielowski, M. Brorson, E. Johnson, H. Topsøe, S. Helveg, Angew. Chem. 123 (2011) 10335-10338.
[60] C. Kisielowski, Q.M. Ramasse, L.P. Hansen, M. Brorson, A. Carlsson, A.M. Molenbroek, H. Topsøe, S. Helveg, Angew. Chem.-Int. Edit. 49 (2010) 2708-2710.
[61] F. Cavani, N. Ballarini, A. Cericola, Catal. Today. 127 (2007) 113-131.
[62] J.G. Speight, Handbook of industrial hydrocarbon processes, Gulf Professional, Oxford Burlington, MA, 2011.
[63] P. Eisele, R. Killpack, Ullmann's Encyclopedia of Industrial Chemistry, Wiley-VCH Verlag GmbH & Co. KGaA, 2000.
[64] N. Calamur, M. Carrera, Updated by Staff, Kirk-Othmer Encyclopedia of Chemical Technology, Wiley-VCH Verlag GmbH & Co. KGaA, 2005.
[65] S.F. Håkonsen, A. Holmen, in: G. Ertl, H. Knözinger, F. Schüth, J. Weitkamp (Eds.), Handbook of Heterogeneous Catalysis, Wiley-VCH Verlag, Weinheim, 2008, pp. 3384-3400.
[66] M. Huff, P.M. Torniainen, L.D. Schmidt, Catal. Today. 21 (1994) 113-128.
[67] A. Khodakov, J. Yang, S. Su, E. Iglesia, A.T. Bell, J. Catal. 177 (1998) 343-351.
[68] F.C. Meunier, A. Yasmeen, J.R.H. Ross, Catal. Today. 37 (1997) 33-42.
[69] K. Chen, S. Xie, A.T. Bell, E. Iglesia, J. Catal. 198 (2001) 232-242.
[70] K. Chen, S. Xie, E. Iglesia, A.T. Bell, J. Catal. 189 (2000) 421-430.
[71] S. Yang, E. Iglesia, A.T. Bell, J. Phys. Chem. B. 109 (2005) 8987-9000.
[72] M.A. Bañares, S.J. Khatib, Catal. Today. 96 (2004) 251-257.
[73] B. Solsona, A. Dejoz, T. Garcia, P. Concepción, J.M.L. Nieto, M.I. Vázquez, M.T. Navarro, Catal. Today. 117 (2006) 228-233.
[74] K. Chen, E. Iglesia, A.T. Bell, J. Phys. Chem. B. 105 (2000) 646-653.
[75] K. Chen, A.T. Bell, E. Iglesia, J. Phys. Chem. B. 104 (2000) 1292-1299.
[76] I.E. Wachs, Catal. Today. 100 (2005) 79-94.
[77] A. Dinse, B. Frank, C. Hess, D. Habel, R. Schomäcker, J. Mol. Catal. A: Chem. 289 (2008) 28-37.

[78] A.A. Lemonidou, L. Nalbandian, I.A. Vasalos, Catal. Today. 61 (2000) 333-341.
[79] X. Rozanska, R. Fortrie, J. Sauer, J. Phys. Chem. C. 111 (2007) 6041-6050.
[80] X. Rozanska, J. Sauer, Int. J. Quantum Chem. 108 (2008) 2223-2229.
[81] X. Rozanska, J. Sauer, J. Phys. Chem. A. 113 (2009) 11586-11594.
[82] P.C. Redfern, P. Zapol, M. Sternberg, S.P. Adiga, S.A. Zygmunt, L.A. Curtiss, J. Phys. Chem. B. 110 (2006) 8363-8371.
[83] X. Rozanska, E.V. Kondratenko, J. Sauer, J. Catal. 256 (2008) 84-94.
[84] O.L.J. Gijzeman, J.N.J. van Lingen, J.H. van Lenthe, S.J. Tinnemans, D.E. Keller, B.M. Weckhuysen, Chem. Phys. Lett. 397 (2004) 277-281.
[85] J.N.J. van Lingen, O.L.J. Gijzeman, B.M. Weckhuysen, J.H. van Lenthe, J. Catal. 239 (2006) 34-41.
[86] J.E. Molinari, I.E. Wachs, J. Am. Chem. Soc. 132 (2010) 12559-12561.
[87] N. Magg, B. Immaraporn, J.B. Giorgi, T. Schroeder, M. Bäumer, J. Dőbler, Z. Wu, E. Kondratenko, M. Cherian, M. Baerns, P.C. Stair, J. Sauer, H.-J. Freund, J. Catal. 226 (2004) 88-100.
[88] J. Haber, in: G. Ertl, H. Knözinger, F. Schüth, J. Weitkamp (Eds.), Handbook of Heterogeneous Catalysis, Wiley-VCH Verlag, Weinheim, 2008, pp. 3359-3384.
[89] A. Dinse, S. Khennache, B. Frank, C. Hess, R. Herbert, S. Wrabetz, R. Schlögl, R. Schomäcker, J. Mol. Catal. A: Chem. 307 (2009) 43-50.
[90] K. Routray, K.R.S.K. Reddy, G. Deo, Appl. Catal., A. 265 (2004) 103-113.
[91] M.D. Argyle, K. Chen, A.T. Bell, E. Iglesia, J. Catal. 208 (2002) 139-149.
[92] A. Khodakov, B. Olthof, A.T. Bell, E. Iglesia, J. Catal. 181 (1999) 205-216.
[93] K. Chen, A. Khodakov, J. Yang, A.T. Bell, E. Iglesia, J. Catal. 186 (1999) 325-333.
[94] M.M. Barsan, F.C. Thyrion, Catal. Today. 81 (2003) 159-170.
[95] R. Grabowski, Catal. Rev. Sci. Eng. 48 (2006) 199-268.
[96] R. Grabowski, S. Pietrzyk, J. Słoczyński, F. Genser, K. Wcisło, B. Grzybowska-Świerkosz, Appl. Catal., A. 232 (2002) 277-288.
[97] R. Grabowski, J. Słoczyñski, N.M. Grzesik, Appl. Catal., A. 242 (2003) 297-309.
[98] I. Rossetti, L. Fabbrini, N. Ballarini, C. Oliva, F. Cavani, A. Cericola, B. Bonelli, M. Piumetti, E. Garrone, H. Dyrbeck, E.A. Blekkan, L. Forni, Catal. Today. 141 (2009) 271-281.
[99] I. Rossetti, L. Fabbrini, N. Ballarini, C. Oliva, F. Cavani, A. Cericola, B. Bonelli, M. Piumetti, E. Garrone, H. Dyrbeck, E.A. Blekkan, L. Forni, J. Catal. 256 (2008) 45-61.
[100] L. Mädler, S.E. Pratsinis, J. Am. Ceram. Soc. 85 (2002) 1713-1718.
[101] L. Mädler, W.J. Stark, S.E. Pratsinis, J. Mater. Res. 17 (2002) 1356-1362.
[102] T. Tani, L. Mädler, S.E. Pratsinis, J. Nanopart. Res. 4 (2002) 337-343.
[103] C. Papadopoulou, J. Vakros, H.K. Matralis, C. Kordulis, A. Lycourghiotis, J. Colloid Interface Sci. 261 (2003) 146-153.
[104] J. Vakros, K. Bourikas, C. Kordulis, A. Lycourghiotis, J. Phys. Chem. B. 107 (2003) 1804-1813.

[105] J. Vakros, A. Lycourghiotis, G.A. Voyiatzis, A. Siokou, C. Kordulis, Appl. Catal., B. 96 (2010) 496-507.
[106] K. Herbst, M. Brorson, A. Carlsson, J. Mol. Catal. A: Chem. 325 (2010) 1-7.
[107] J.A. Rodriguez, S. Chaturvedi, J.C. Hanson, A. Albornoz, J.L. Brito, J. Phys. Chem. B. 102 (1998) 1347-1355.
[108] J.A. Rodriguez, J.Y. Kim, J.C. Hanson, J.L. Brito, Catal. Lett. 82 (2002) 103-109.
[109] S.S. Saleem, Infrared Phys. Technol. 27 (1987) 309-315.
[110] T. Ono, N. Ogata, Y. Miyaryo, J. Catal. 161 (1996) 78-86.
[111] M. Digne, K. Marchand, P. Bourges, Oil & Gas Science and Technology - Rev. IFP. 62 (2007) 91-99.
[112] M. De Boer, A.J. Vandillen, D.C. Koningsberger, J.W. Geus, M.A. Vuurman, I.E. Wachs, Catal. Lett. 11 (1991) 227-239.
[113] D.P. Debecker, B. Schimmoeller, M. Stoyanova, C. Poleunis, P. Bertrand, U. Rodemerck, E.M. Gaigneaux, J. Catal. 277 (2011) 154-163.
[114] D.J. Perez-Martinez, P. Eloy, E.M. Gaigneaux, S.A. Giraldo, A. Centeno, Appl. Catal., A. 390 (2010) 59-70.
[115] R. Cid, J. Villaseor, F. Orellana, J.L.G. Fierro, A. López Agudo, Appl. Catal. 18 (1985) 357-372.
[116] P. Gajardo, A. Mathieux, P. Grange, B. Delmon, Appl. Catal. 3 (1982) 347-376.
[117] D.J. Pérez-Martínez, E.M. Gaigneaux, S.A. Giraldo, A. Centeno, J. Mol. Catal. A: Chem. 335 (2011) 112-120.
[118] N. Kunisada, K.-H. Choi, Y. Korai, I. Mochida, K. Nakano, Appl. Catal., A. 273 (2004) 287-294.
[119] J. Huang, N. Van Vegten, Y. Jiang, A. Baiker, M. Hunger, Angew. Chem.-Int. Edit. 49 (2010) 7776-7781.
[120] J. Huang, Y. Jiang, N. van Vegten, M. Hunger, A. Baiker, J. Catal. 281 (2011) 352-360.
[121] J.-D. Grunwaldt, M. Caravati, S. Hannemann, A. Baiker, Phys. Chem. Chem. Phys. 6 (2004) 3037-3047.
[122] B. Xiang, C. Yu, H. Xu, W. Li, Catal. Lett. 125 (2008) 90-96.
[123] B. Schimmoeller, R. Delaigle, D.P. Debecker, E.M. Gaigneaux, Catal. Today. 157 (2010) 198-203.
[124] B. Schimmoeller, H. Schulz, A. Ritter, A. Reitzmann, B. Kraushaar-Czarnetzki, A. Baiker, S.E. Pratsinis, J. Catal. 256 (2008) 74-83.
[125] N. Magg, J.B. Giorgi, T. Schroeder, M. Bäumer, H.-J. Freund, J. Phys. Chem. B. 106 (2002) 8756-8761.
[126] D.E. Keller, F.M.F. de Groot, D.C. Koningsberger, B.M. Weckhuysen, J. Phys. Chem. B. 109 (2005) 10223-10233.
[127] D.E. Keller, D.C. Koningsberger, B.M. Weckhuysen, Phys. Chem. Chem. Phys. 8 (2006) 4814-4824.
[128] D.E. Keller, T. Visser, F. Soulimani, D.C. Koningsberger, B.M. Weckhuysen, Vib. Spectrosc. 43 (2007) 140-151.
[129] G.T. Went, S.T. Oyama, A.T. Bell, J. Phys. Chem. 94 (1990) 4240-4246.
[130] X. Gao, J.-M. Jehng, I.E. Wachs, J. Catal. 209 (2002) 43-50.
[131] B. Kilos, A.T. Bell, E. Iglesia, J. Phys. Chem. C. 113 (2009) 2830-2836.

[132] E.V. Kondratenko, M. Baerns, Appl. Catal., A. 222 (2001) 133-143.
[133] T. Blasco, A. Galli, J.M. López Nieto, F. Trifiró, J. Catal. 169 (1997) 203-211.
[134] P. Concepción, M.T. Navarro, T. Blasco, J.M. López Nieto, B. Panzacchi, F. Rey, Catal. Today. 96 (2004) 179-186.
[135] R. Bulánek, P. Čičmanec, H. Sheng-Yang, P. Knotek, L. Čapek, M. Setnička, Appl. Catal., A. 415–416 (2012) 29-39.
[136] D.E. Keller, S.M.K. Airaksinen, A.O. Krause, B.M. Weckhuysen, D.C. Koningsberger, J. Am. Chem. Soc. 129 (2007) 3189-3197.
[137] B. Frank, A. Dinse, O. Ovsitser, E.V. Kondratenko, R. Schomäcker, Appl. Catal., A. 323 (2007) 66-76.
[138] K. Chen, A.T. Bell, E. Iglesia, J. Catal. 209 (2002) 35-42.
[139] T.F. Hayden, J.A. Dumesic, J. Catal. 103 (1987) 366-384.
[140] J. Leyrer, D. Mey, H. Knözinger, J. Catal. 124 (1990) 349-356.
[141] J. Leyrer, R. Margraf, E. Taglauer, H. Knözinger, Surf. Sci. 201 (1988) 603-623.
[142] H. Aritani, T. Tanaka, T. Funabiki, S. Yoshida, K. Eda, N. Sotani, M. Kudo, S. Hasegawa, J. Phys. Chem. 100 (1996) 19495-19501.
[143] M. Henker, K.-P. Wendlandt, J. Valyon, P. Bornmann, Appl. Catal. 69 (1991) 205-220.
[144] E. Heracleous, M. Machli, A.A. Lemonidou, I.A. Vasalos, J. Mol. Catal. A: Chem. 232 (2005) 29-39.
[145] S.C. Nayak, D. Shee, G. Deo, Catal. Lett. 136 (2010).
[146] P.M. Mortensen, J.D. Grunwaldt, P.A. Jensen, K.G. Knudsen, A.D. Jensen, Appl. Catal., A. 407 (2011) 1-19.
[147] J.A. Lercher, 15th International Congress on Catalysis. Programme. Poster Symposium PS.02., Munich, 2012.
[148] A. Meiswinkel, C. Thaller, M. Bock, L. Alvarado, D. Hartmann, A.C. van Veen, J.A. Lercher, 15th International Congress on Catalysis, Munich, 2012.
[149] F.N. Naraschewski, C. Praveen Kumar, A. Jentys, J.A. Lercher, Appl. Catal., A. 391 (2011) 63-69.
[150] O. Ovsitser, E.V. Kondratenko, Catal. Today. 142 (2009) 138-142.
[151] V.C. Corberán, Catal. Today. 99 (2005) 33-41.
[152] O. Ovsitser, C. Carrero, R. Schomäcker, A. Trunschke, 15th International Congress on Catalysis, Munich, 2012.
[153] I. Schmidt, A. Krogh, K. Wienberg, A. Carlsson, M. Brorson, C.J.H. Jacobsen, Chem. Commun. (2000) 2157-2158.
[154] J.-D. Grunwaldt, C. Beck, W. Stark, A. Hagen, A. Baiker, Phys. Chem. Chem. Phys. 4 (2002) 3514-3521.
[155] M.S. Holm, S. Saravanamurugan, E. Taarning, Science. 328 (2010) 602-605.
[156] M. Skovgaard, K. Almdal, B.F. Sørensen, S. Linderoth, A. Van Lelieveld, J. Compos. Mater. 45 (2011) 2817-2822.
[157] V. Subramani, S.K. Gangwal, Energy Fuels. 22 (2008) 814-839.
[158] J. Weitkamp, ChemCatChem. 4 (2012) 292-306.
[159] J.W. Ward, Fuel Process. Technol. 35 (1993) 55-85.

[160] I. Rossetti, C. Biffi, C.L. Bianchi, V. Nichele, M. Signoretto, F. Menegazzo, E. Finocchio, G. Ramis, A. Di Michele, Appl. Catal., B. 117 (2012) 384-396.
[161] J.R. Jensen, T. Johannessen, S. Wedel, H. Livbjerg, J. Catal. 218 (2003) 67-77.
[162] F. Huber, H. Meland, M. Rønning, H. Venvik, A. Holmen, Top. Catal. 45 (2007) 101-104.
[163] H. Meland, T. Johannessen, B. Arstad, H.J. Venvik, M. Ronning, A. Holmen, Stud. Surf. Sci. Catal. 162 (2006) 985-992.
[164] V.I. Pârvulescu, C. Paun, V. Pârvulescu, M. Alifanti, I. Giakoumelou, S. Boghosian, S.B. Rasmussen, K.M. Eriksen, R. Fehrmann, J. Catal. 225 (2004) 24-36.